

Last Call for Life: Habitability of Terrestrial Planets Orbiting Red Giants and White Dwarfs

A dissertation presented

by

Thea Kozakis

to

The Department of Astronomy and Space Sciences

in partial fulfillment of the requirements

for the degree of

Doctor of Philosophy

in the subject of

Astronomy & Astrophysics

Cornell University

Ithaca, New York

August 2020

© 2020 — Thea Kozakis

All rights reserved.

Last Call for Life: Habitability of Terrestrial Planets Orbiting Red Giants and White Dwarfs

Abstract

As a star evolves, the orbital distance where liquid water is possible on the surface of an Earth-like planet, the habitable zone, evolves as well. While stellar properties are relatively stable on the main sequence, post-main sequence evolution of a star involves significant changes in stellar temperature and radius, which is reflected in the changing irradiation at a specific orbital distance when the star becomes a red giant, and then later a white dwarf. To search planets in these systems for signs of life it is essential that we understand how stellar evolution influences atmospheric photochemistry along with detectable biosignatures. We use EXO-Prime, which consists of a 1D coupled climate/photochemistry and a line-by-line radiative transfer code, to model the atmospheres and spectra of habitable zone planets around red giants and white dwarfs, and assess the time dependency of detectable biosignatures.

Biosketch

Thea Kozakis was born in Suffern, New York and spent the majority of her childhood in Lebanon, New Jersey with her parents John and Jacqueline, her sisters Cassandra and Sydney, and several wonderful dogs. From a young age she played the piano competitively, along with reading an excessive amount of books. As a teenager she worked as a cashier at a local grocery store, and paid significantly more attention in her English classes than in her math classes. She attended the College of Charleston in South Carolina, where she worked as a campus tour guide and the physics lab manager's assistant. She wrote her undergraduate thesis with Dr. Joseph Carson on directly imaging exoplanets around high-mass stars. During this work Thea was able to be a part of the discovery of κ Andromedae b, a “super-Jupiter” which she refers to fondly as Derek. In 2013 she graduated summa cum laude with bachelor's degrees in physics and astrophysics, and a minor in mathematics.

In the fall of 2013 she began a doctorate program in astronomy at Cornell University in New York. Along with being a research assistant Thea was also a teaching assistant, a mental health counselor, a dancer, and frequently engaged in climate change and human rights activism. As a part of the Carl Sagan Institute, Thea worked on her doctorate with her advisor, Dr. Lisa Kaltenegger, switching from exoplanet observations to more theoretical astrobiology. She wrote and defended her doctoral thesis in the spring of 2020. After leaving Cornell she is set to begin a postdoctoral fellowship at the Denmark Technical University, where she will continue to study life in the universe.

This thesis is dedicated to everyone committed to the fight against climate change. Looking for habitable planets is a fruitless effort if we cannot keep our own planet habitable. In the words of Carl Sagan:

“In our obscurity, in all this vastness, there is no hint that help will come from elsewhere to save us from ourselves. The Earth is the only world known so far to harbor life. There is nowhere else, at least in the near future, to which our species could migrate. Visit, yes. Settle, not yet. Like it or not, for the moment the Earth is where we make our stand.”

Acknowledgments

They say it takes a village to raise a child, and I feel like it took even more than that to help me get my PhD! I have so many people who have supported me throughout this process, but for the purposes of keeping my acknowledgements shorter than the main body of my thesis, this list is woefully incomplete.

First off to my advisor, Lisa Kaltenegger, who made this all possible. Thank you for being willing to take on an enthusiastic student with zero knowledge of astrobiology. This thesis completely changed my research trajectory in a way I couldn't be happier with. I'd also like to thank the Simons Foundation and the New York Space Grant Program, both of which gave me the financial support I needed to complete this work.

Of course my graduate studies at Cornell could not have happened without my undergraduate career at the College of Charleston. I'd like to thank my undergraduate advisor, Joe Carson, who was the most patient, thoughtful advisor I could have asked for when entering a strange new field. Without such an incredibly positive first research experience, I'm not sure if I would have pursued graduate school. I'm looking forward to us being Cornell alumni together!

I'm extremely grateful to so many of my first physics teachers: Jim Neff who first introduced me to stellar evolution and gave me my first view of what graduate studies are like, Laura Penny who gave me invaluable advice about being a woman in science, and Jeff Wragg who refused to tolerate my lack of self-confidence. I'm happy to say I don't have that problem any more.

And especially to Kat Low. Working as your assistant was so much more than a job

CHAPTER 0. ACKNOWLEDGMENTS

to both of us, and I continue to be grateful for your support. Thanks for always being there for me.

I had so many wonderful, supportive friends in and out of the physics department, and I'm especially thankful to Laura Stevens, Ally Olejar, Drew Moore, and Ryan Wilke, who I still joke around with on a regular basis.

At Cornell I've been so thankful for the community I've found within the astronomy department. In particular the members of ABC (Astronomy Breakfast Club), Dylan Cromer and Christopher Rooney, although we were definitely not good at consistently assembling on time. Dylan, thank you so much for being my partner in helping to improve the climate in academia! Christopher, thanks for always being willing to goof around with me! And thank you both for always listening to whatever was on my mind. I'm glad we're already figuring out how to play board games virtually so we can keep at it even after I leave.

I'd like to thank the "exo-post docs" that have helped me an extreme amount this last year in my job search. I don't know what I would have done without all of you! Andrew Ridden-Harper, thank you your constant thoughtfulness, whether it's helping me to write a job talk or to find an Icelandic glacier that had apparently already melted. Ryan MacDonald, your scientific insight has been so valuable to me, along with our fun conversations about life in the universe, science fiction, and other random topics. I'm also excited that you now love white dwarf planets as much as me! Jake Turner, you've been a huge source of support both in the office and fighting to improve the world. You and your partner Veronica fight for equality harder than anyone else I know.

A special shout out to my academic brother and long-term officemate, Jack Madden.

CHAPTER 0. ACKNOWLEDGMENTS

I can't describe how much your friendship has meant to me over the years. Thank you so much for your academic and emotional support, our fun philosophical conversations, and our time spent singing our signature karaoke song, "Let It Go". I'm so happy I got to share so many experiences with you! (P.S. Let's get a better signature karaoke song)

In addition to my scientific work, I also had the privilege of working as an EARS counselor (Empathy, Assistance, and Referral Services), where I grew more as a person than I had ever thought possible, and connected with more people than I could possibly name. To name a few, there's Janet Shortall, who is the most empathetic person I know. When I'm frustrated with someone, I frequently ask myself WWJD?: What Would Janet Do? Thank you for helping me through the bad times and celebrating with me during the good ones. Kate Shanks, who is one of the most thoughtful and helpful people I know. I always looked forward to our Friday lunches, with our conversations ranging from issues we were facing, the science we were doing, and the finer points of Harry Potter. Not to mention the fact that you're the only person I know with a longer Duolingo streak than me! Thank you so much for being there for me. Sari Vihervaara, whose calm demeanor and quiet wisdom and humor balanced my energy perfectly as we trained the next generation of counselors together. Thank you for your constant support and our wonderful conversations. I hope I see you and your family over in Scandinavia! And Alana Sullivan, who I have always found so easy to talk to about anything and everything. You're my EARS sister, and I'm so thankful to have you in my life.

I have been so thankful to be a part of the Ithaca community, where so many people care deeply about the state of the world, particularly the members of the Sunrise Movement and Extinction Rebellion. It has been an honor to fight for our planet with you! And especially to June Seaney, who I am so thankful to have as a dance teacher and

CHAPTER 0. ACKNOWLEDGMENTS

a friend. You have such a beautiful world view, and I love that I can talk to you about anything. One of the main reasons I'll have to visit Ithaca is to come dance with you!

And last, but certainly not least, my family, who has supported me during a scientific journey unprecedented in our family's history. My father, John, who apparently thought he was dragging me out to look through his telescope as a child, when he was really instilling within me a love of the universe. Thank you so much for that. My mother, Jacqueline, who has always listened to me and encouraged me over the years, even with things she couldn't personally relate with. Thank you for always being able to add compassion or fun to any situation.

My sisters, Cassandra and Sydney, who lead such wonderful lives that it has always been easy to brag about them. Cassandra, you're the perfect combination of humor and taking care of business ATFT, and are growing such a beautiful family of your own. I'm glad I always had a companion in early childhood to make up ridiculous games and crazy dollhouse scenarios with. Sydney, despite our 8 year age gap we have always been able to have fun together, whether it's playing Animal Crossing, or shopping on our annual post-Christmas mall trip. Your dedication to work and school make me look like a slacker, and I know your incredible talents are just starting to emerge.

My brother-in-law, Matt, who along with being the only family member to consistently help me with my summer vacation jigsaw puzzles, is a wonderful match for my sister and a formidable beekeeper. My baby nephew Clay, who I believe just discovered that his hands belong to him. I can't wait to share the universe with you!

And of course to our dog, Charlie. You don't understand English, but hopefully mom and dad can give you a bone as my thanks. No one can run through the woods like

CHAPTER 0. ACKNOWLEDGMENTS

a total maniac as well as you do.

I'd also like to thank everyone who has been supporting me during these final weeks in graduate school. This thesis has been put together and defended entirely in quarantine during the COVID-19 pandemic. Although it may seem that I've been alone these past weeks, in reality I've been surrounded by constant love and support. And for this, I consider myself truly lucky.

I look forward to seeing you all in person on the other side of this, in what I hope we can make into a better world.

Contents

| | |
|--|--------------|
| Abstract | iii |
| Biosketch | iv |
| Dedication | v |
| Acknowledgments | vi |
| List of Figures | xv |
| List of Tables | xviii |
| | |
| I Introduction | 1 |
| | |
| 1 The search for life in the universe | 2 |
| 1.1 Where to look for life? | 2 |
| 1.1.1 Exoplanets entering the scene | 6 |
| 1.1.2 Exoplanet atmospheric characterization | 8 |
| 1.2 How could we identify life? | 10 |
| 1.2.1 The habitable zone: a starting point | 11 |
| 1.2.2 Which biosignatures are ‘enough’? | 13 |
| 1.3 What role does stellar evolution play? | 20 |

CONTENTS

| | | |
|--|--|-----------|
| 1.3.1 | Red giant evolution | 22 |
| 1.3.2 | High mass stars after AGB | 25 |
| 1.3.3 | White dwarf evolution | 26 |
| 1.3.4 | What does this thesis contribute to our understanding? | 27 |
| II Dying to live: habitability around red giants | | 28 |
| 2 Atmospheres and UV Environments of Earth-like Planets throughout Post-main-sequence Evolution | | 29 |
| 2.1 | Introduction | 29 |
| 2.2 | Methods | 32 |
| 2.2.1 | Post-MS HZ boundaries | 33 |
| 2.2.2 | Planetary semimajor axis evolution | 36 |
| 2.2.3 | Planetary atmospheric erosion | 37 |
| 2.2.4 | Post-MS stellar model spectra | 37 |
| 2.2.5 | Modeling planetary atmospheres and UV surface environments | 39 |
| 2.3 | Results | 42 |
| 2.3.1 | Orbital distance of the post-MS HZ | 42 |
| 2.3.2 | Post-MS habitable zone lifetime | 43 |
| 2.3.3 | Planets at Earth equivalent orbital distances | 47 |
| 2.3.4 | Planetary Atmospheres: post-MS evolution | 52 |
| 2.4 | Discussion | 55 |
| 2.4.1 | How could life form/become detectable on objects habitable during the post-MS? | 55 |
| 2.4.2 | Could we directly image planets in the post-MS HZ of red giants? | 56 |
| 2.4.3 | Continuous time in the habitable zone | 58 |
| 2.4.4 | Comparisons to previous studies | 58 |
| 2.5 | Conclusions | 59 |

CONTENTS

3 High resolution Spectra of Earth-Like Planets Orbiting Red Giant Host Stars 61

3.1 Introduction 61

3.2 Methods 66

3.2.1 Stellar Hosts and Planet Atmospheric Spectra Models 66

3.2.2 Coronagraph simulation of detectability of spectral features 69

3.3 Results: spectra of Earth-like planets orbiting red giant hosts 70

3.3.1 Spectra of Earth-like planets in the RG HZ receiving modern Earth irradiation 70

3.3.2 Spectra of Earth-like planets in the HZ through the red giant’s evolution 77

3.3.3 Estimated observation times for red giant HZ planets 80

3.4 Discussion and Conclusions 82

III Life after (stellar) death: habitability around white dwarfs 85

4 UV Surface Environments and Atmospheres of Earth-like Planets Orbiting White Dwarfs 86

4.1 Introduction 86

4.2 Methods 89

4.2.1 Planet model: *EXO-Prime* 89

4.2.2 White Dwarf Model Spectra 91

4.2.3 Photochemistry of some biologically interesting species 92

4.3 Results 94

4.3.1 Time evolution of a white dwarf’s habitable zone 94

4.3.2 Planetary photochemistry environments for different stages in a WD’s evolution 96

4.3.3 UV surface environment around an evolving WD 100

CONTENTS

| | | |
|-----------|---|------------|
| 4.3.4 | Planetary environments for planets in the HZ through the evolution of a WD | 105 |
| 4.4 | Discussion | 111 |
| 4.4.1 | How could white dwarf planets form? | 111 |
| 4.4.2 | Only dry planets? White dwarfs start with an extremely hot phase | 112 |
| 4.4.3 | A white dwarf planet's evolution differs from that of Earth | 113 |
| 4.5 | Conclusions | 113 |
| 5 | Planetary Spectra and Biosignatures of Earth-like Planets Orbiting in the White Dwarf Habitable Zone | 116 |
| 5.1 | Introduction | 116 |
| 5.2 | Methods | 118 |
| 5.2.1 | WD cooling and spectral models | 118 |
| 5.2.2 | Planetary atmospheric models and spectra | 119 |
| 5.3 | Results: Transmission spectra of Earth-like planets orbiting WDs | 120 |
| 5.3.1 | Transmission spectra of planets orbiting WDs at the Earth-equivalent distance | 120 |
| 5.3.2 | Transmission spectra of rocky planets in the WD HZ throughout white dwarf cooling | 126 |
| 5.4 | Discussion & Conclusion | 128 |
| IV | Conclusions | 130 |
| 6 | Conclusions and future prospects | 131 |
| | References | 134 |

List of Figures

| | | |
|-----|---|----|
| 2.1 | IUE red giants fit to HR-diagram | 39 |
| 2.2 | Red giant spectra | 40 |
| 2.3 | Luminosity and habitable zone evolution for 1.3, 2.3, and 3.0 M_{\odot} red giants | 45 |
| 2.4 | Temperature/chemical profiles for planets orbiting red giants | 48 |
| 2.5 | Comparisons of incident/surface UV and ozone production for planets orbiting red giants | 49 |
| 2.6 | Temperature/chemical profiles of planets orbiting red giants throughout evolution | 53 |
| 2.7 | Incident/surface UV flux for planets orbiting red giants | 55 |
| 3.1 | IUE red giant spectra scaled to the solar constant | 68 |
| 3.2 | Temperature/chemical profiles for planets orbiting red giants | 71 |
| 3.3 | Reflectance/emission spectra of planets orbiting red giants at 1 AU equivalent | 73 |
| 3.4 | O ₂ feature for planets orbiting red giants at high resolution | 76 |

LIST OF FIGURES

| | | |
|-----|---|-----|
| 3.5 | Red giant luminosity evolution and resulting reflectance/emission spectra of orbiting planets | 78 |
| 3.6 | Required integration times for observations with LUVOIR-A | 81 |
| 4.1 | White dwarf luminosity evolution | 88 |
| 4.2 | White dwarf spectra scaled to the 1 AU equivalent | 89 |
| 4.3 | Evolution of a white dwarf's habitable zone | 95 |
| 4.4 | Temperature/chemical profiles for planets orbiting white dwarfs at the 1 AU equivalent distance | 98 |
| 4.5 | Surface UV environment for planets orbiting white dwarfs at the 1 AU equivalent distance | 103 |
| 4.6 | UV surface environments for planets orbiting white dwarfs throughout cooling: Case A | 106 |
| 4.7 | UV surface environments for planets orbiting white dwarfs throughout cooling: Case A | 109 |
| 4.8 | Temperature/chemical profiles for planets orbiting white dwarfs throughout cooling | 110 |
| 5.1 | Temperature/chemical profiles of planets orbiting white dwarfs at the 1 AU equivalent distance and throughout cooling | 121 |
| 5.2 | Transmission spectra for planets orbiting white dwarfs at the 1 AU equivalent distance and throughout cooling | 123 |

LIST OF FIGURES

| | |
|--|-----|
| 5.3 Spectral features for planets orbiting white dwarfs at the 1 AU equivalent distance | 125 |
| 5.4 Spectral features for planets orbiting white dwarfs throughout cooling . . . | 127 |

List of Tables

| | | |
|------|---|----|
| 2.1 | Padova catalog stellar lifetimes | 32 |
| 2.2 | HZ constants from Ramirez & Kaltenegger (2018) | 35 |
| 2.3 | IUE spectra hosts | 38 |
| 2.4 | HZ boundaries and semimajor axis evolution | 43 |
| 2.5 | Post-MS HZ lifetime | 44 |
| 2.6 | Model Summary for Earth-Equivalent Distances | 50 |
| 2.7 | UV Integrated Fluxes for Earth-Equivalent Distances | 52 |
| 2.8 | Model Summary throughout post-MS evolution | 53 |
| 2.9 | UV Integrated Fluxes Throughout Post-MS Evolution | 54 |
| 2.10 | Luminosity class III stars within 30 pc | 57 |
| 3.1 | Properties of the selected red giant hosts | 65 |
| 4.1 | Model summary for Earth-equivalent irradiance | 97 |

LIST OF TABLES

| | | |
|-----|---|-----|
| 4.2 | UV Integrated Fluxes | 101 |
| 4.3 | UV Integrated fluxes compared to Earth | 102 |
| 4.4 | Case A & Case B Results | 105 |
| 4.5 | UV Integrated fluxes evolution | 108 |
| 4.6 | UV Integrated fluxes evolution Earth comparison | 111 |
| 5.1 | Model summary for planets orbiting white dwarfs | 122 |

Part I

Introduction

Chapter 1

The search for life in the universe

Astronomy has been a part of human culture for as long as there have been humans. Even before our species understood even the simplest concepts about the world around us, we have always been fascinated by the night sky. And as our knowledge of our place in the universe grew, so did one of humanity's most compelling questions: "Are we alone?" To continue on our path to answer this question, we need to understand where to look for life, how to look for life, and study the nature of stars unlike our own.

1.1 Where to look for life?

Early humans learned that the night sky was not just beautiful, but that it was predictable. They used it to measure the passing of time, and determine when they should grow and harvest their crops. However, they discovered that several of these star-like objects followed a different pattern, and were referred to by the ancient Greeks as *πλανήτης* (*planētēs*), meaning "wanderers", which we now know to be planets in our

CHAPTER 1. THE SEARCH FOR LIFE IN THE UNIVERSE

own Solar System. Our own planet, Earth, was thought to be the center of the universe, with all the planets and stars revolving around us. This view was challenged during the renaissance era, when astronomer Nicolaus Copernicus posthumously published his work *De revolutionibus orbium coelestium* (*On the Revolutions of the Heavenly Spheres*), asserting that the Earth and the other planets orbited the Sun, and that the stars in the sky were much farther from us than the distance between Earth and the Sun (Copernicus 1543). Although this model accurately predicted the movements of the planets, it was not taken seriously amongst the majority of astronomers. However, a few were swayed. Several decades later Italian astronomer Giordano Bruno published his work *De l'infinito universo et mundi* (*On the infinite universe and worlds*) with the idea that the stars we saw in the sky in the sky were other Suns that hosted their own planets, some of which supported life, and that Earth was just one of many habitable worlds (Bruno 1584). These views combined with his other denials of Catholic doctrines resulted in his execution, although his ideas survived. A couple of decades later the Copernican revolution was in full swing, and thanks to scientists such as Johannes Kepler, Galileo Galilei, and Issac Newton, by the end of the 16th century the scientific community had accepted the heliocentric view as a fact, and Earth was considered just a planet of the Solar System, rather than the center of the universe.

By the 20th century, the world was a vastly different place, and leaps and bounds of technological and scientific advancement had been made. In 1926, another leap into our understanding of humanity's place in the universe was made when astronomer Edwin Hubble discovered that our local universe was simply the Milky Way galaxy, and that the universe was comprised of countless extremely distant galaxies, all containing billions of stars (Hubble 1926). Our place in the universe was further demoted to just orbiting a

CHAPTER 1. THE SEARCH FOR LIFE IN THE UNIVERSE

typical star in a galaxy, far from the old ideas of being the center of everything. Every discovery seemed to point us further in the direction that we were not special, and that the universe was more vast than humanity had ever imagined. It was this train of thought that caused Italian physicist Enrico Fermi to ask his colleagues, “but where is everybody”? If our galaxy alone had billions of stars like our Sun, why hadn’t we already been visited by other intelligent civilizations? Even if interstellar travel took millions of years, many of our galaxy’s stars are billions of years older than the Sun, so the aliens should have had plenty of time to make themselves known. This question served as the foundation for what is commonly referred to as the Fermi Paradox, which was outlined in Hart (1975).

The following decade after Fermi’s question the first radio SETI (Search for Extra-Terrestrial Intelligence) experiments were carried out. Two studies (Cocconi & Morrison 1959; Drake 1961) independently chose to search nearby stars looking for signals at 1420 megahertz, corresponding to the famous 21-cm hydrogen line, which astronomer Frank Drake described as a “natural hailing wavelength”. They reasoned that if an intelligent species had emerged and began to develop radio astronomy, that studying hydrogen would be one of the first steps. The authors acknowledged that their work could be considered more in the realm of science-fiction rather than science, but Cocconi & Morrison (1959) also pointed out “the probability of success is difficult to estimate, but if we never search the chance of success is zero”. In 1961 the first SETI meeting, commonly referred to as “The Greenbank Conference” took place, where 10 individuals, including Frank Drake and Carl Sagan, came together to seriously discuss how to look for life in the universe. It was at this meeting that the famous Drake Equation (Drake 1965) was first written down, simply as a sort of ‘agenda’ for the meeting to cover. This

CHAPTER 1. THE SEARCH FOR LIFE IN THE UNIVERSE

team later dubbed themselves “The Order of the Dolphin”, as one of their members, neurophysiologist John Lilly, had done work using communications with dolphins to study how we might communicate with other life forms (Lilly 1961). Around this point in time the first references were also made to the concept of a habitable zone (Huang 1959,1960), the region around a star where liquid water could exist on the surface of a rocky planet, along with concept of using atmospheric composition to look for life, searching signals known as biosignatures (Lovelock 1965). However, with no known planets outside our Solar System, these ideas were not well studied.

More and more scientists began to think about how radio SETI could be carried out (e.g. Shklovskii & Sagan 1966), while others thought of other interesting methods for finding intelligent civilizations by thinking about energy consumption (e.g. Dyson 1960; Kardashev 1964). However, many felt that the search for life was fruitless, that with the strict constraints on the evolution of life that it was safe to say Earth was the only inhabited planet (e.g. Tipler 1980). Astronomers Carl Sagan and Frank Drake fought hard against these views, citing the “principle of mediocrity”, which implies that Earth is the norm, rather than special (Sagan & Newman 1983). The SETI Institute was founded in 1984, although it was often faced with extreme pessimism and claims that it was a waste time (Tipler 1993), along with frequent funding cancellation (Garber 1999). However, by the mid-1990s the scientific discussion around the search for life began to change, as a new class of objects was found: exoplanets.

1.1.1 Exoplanets entering the scene

Exoplanets, planets that orbit stars or stellar remnants other than our Sun, were first discovered around a stellar remnant, a pulsar (Wolszczan & Frail 1992), although this discovery was quickly joined by 51 Pegasi b, a gas giant orbiting a Sun-like star (Mayor & Queloz 1995). 51 Pegasi b, like most early exoplanet discoveries, was found via the radial velocity method, which uses the Doppler effect to detect the wobble of star caused by an orbiting planet. This was the predominant method of exoplanet detection until the early 2000's, when a planet previously detected with this method was re-detected using the transit method (Charbonneau et al. 2000). This method uses the photometric monitoring of stars to look for dips in brightness caused by an orbiting planet eclipsing their host star. The transit method found its first new exoplanet in 2003 (Konacki et al. 2003), and began to rival the radial velocity method in effectiveness. Direct imaging, a method in which coronagraphs and adaptive optics are used to directly observe a planet orbiting a host star (e.g. Bonneau et al. 1975), made its first confirmed discovery a year later (Chauvin et al. 2004), although detection rates via this method remained low.

The planets discovered within the first decade of exoplanet detection were often large gas giants on short period orbits, owing mainly to the biases of both the radial velocity and transit methods to detect such planets. Despite these known biases some continued to speculate that our Solar System could still be unique (e.g. Beer et al. 2004), with smaller, longer period planets still absent from the exoplanet sample. Detection efforts increased, with large ground based surveys such as WASP (Pollacco et al. 2006), and the first ever space-based transit survey, CoRoT (Baglin et al. 2006). Direct imaging succeeded in discovering its first multiple planet system (Marois et al. 2008)),

CHAPTER 1. THE SEARCH FOR LIFE IN THE UNIVERSE

and launched several large imaging efforts (e.g. Macintosh et al. 2008; Beuzit et al. 2008; Tamura 2009).

The real revolution in exoplanet detection began in 2009 with the launch of the *Kepler Space Telescope*, designed specifically to detect exoplanet transits (Borucki et al. 2010). *Kepler* continuously monitored over 150,000 stars in the “Kepler field”, with a cadence of 30 minutes. Shortly after the number of confirmed exoplanets passed 1,000 in early 2014, the *Kepler* mission announced over 700 additional planets (Lissauer et al. 2014; Rowe et al. 2014). At this point astronomers had realized that multi-planet systems are extremely unlikely to be mimicked by background sources, which was the largest uncertainty for exoplanet detections with the *Kepler* mission. *Kepler*’s second reaction wheel failed in 2013, bringing the original mission to a close, but starting a secondary mission *K2* which surveyed different parts of the sky in the galactic plane for shorter time periods (Howell et al. 2014). When the mission came to a close in 2018, it had discovered over 2,000 exoplanets, with over 2,000 candidates still waiting to be confirmed.

The *Kepler* mission not only significantly increased the number of known exoplanets, but also provided first insights into their diversity. Discoveries included multi-planet systems (e.g. Rowe et al. 2014), planets around binary stars (e.g. Doyle et al. 2011; Hibbert 2011), and most excitingly for those interested in the search for life, Earth-sized planets in their stars’ habitable zones (e.g. Gaidos 2013; Quintana et al. 2014; Kane et al. 2016, Berger18).

During this period of time smaller surveys made additional discoveries of Earth-sized planets in their habitable zones, including around our closest star system (Anglada-

Escudé et al. 2016), and a multiple planet system, TRAPPIST-1, with five small planets, three of which reside in the habitable zone (Gillon et al. 2017). As more and more discoveries are made, predictions of what fraction of stars host a small, rocky planet in their habitable zone, η_{\oplus} (eta Earth), has become more optimistic. Multiple estimates predict an occurrence rate of $\sim 25\%$ (e.g. Petigura et al. 2013; Dressing & Charbonneau 2015; Barbato et al. 2018; Hsu et al. 2019), which bodes well for the search for life.

In 2018 the Transiting Exoplanet Survey Satellite (TESS) launched, with the objective of carrying out an all-sky exoplanet search, and an expected yield of 10,000 planets (Ricker et al. 2014). Not only will TESS be able to look into the habitable zones of a number of stars (Kaltenegger et al. 2019), but it has also already found its first Earth-sized habitable zone planets (e.g. Gilbert et al. 2020).

At the time of this thesis, there are currently 4,171 known exoplanets, with thousands of candidates awaiting confirmation¹. With an ever-growing substantial list of known exoplanets, the field of exoplanet atmospheric characterization was born.

1.1.2 Exoplanet atmospheric characterization

Of the currently known exoplanets, over three-quarters of them are known to transit their stellar hosts (3194 of 4171), enabling the possibility of transmission and emission spectroscopy (e.g. Seager et al. 2000; Brown 2001). When a planet transits its star, a portion of the star's light will pass through the planetary atmosphere, allowing for characterization via transmission spectroscopy. On the opposite side of the transit as

¹<https://exoplanetarchive.ipac.caltech.edu>

CHAPTER 1. THE SEARCH FOR LIFE IN THE UNIVERSE

the planet is about to move behind its host star, emission spectroscopy can probe the dayside of the planet in secondary eclipse measurements.

The first planets to be characterized were hot, large gas giants, not only because they were the first planets discovered, but because atmospheric characterization is easier for planets with larger atmospheric scale heights. The first detected transiting planet, HD 209458b, was also the first planet to be characterized via both transmission spectroscopy (Vidal-Madjar et al. 2003, 2004) with HST, and emission spectroscopy (Deming et al. 2005) with Spitzer, resulting in detections of Na, H, O, and C, along with estimates of the atmosphere's brightness temperature.

Numerous emission spectroscopy observations were taken by Spitzer in the following decade (e.g. Deming et al. 2007; Demory et al. 2012), and improved techniques were able to detect atmospheric thermal inversions in gas giant planets (e.g. Knutson et al. 2008; Kreidberg et al. 2014; Diamond-Lowe et al. 2014; Line et al. 2016). Continued efforts have allowed characterization of smaller planets such as multiple studies of a ~ 8 Earth mass planet 55 Cancri e (e.g. Demory et al. 2012; Tsiaras et al. 2016; Ridden-Harper et al. 2016; Zhang 2019), and a detection of H₂O on sub-Neptune K2-18b (e.g. Benneke et al. 2019; Tsiaras et al. 2019).

Although lessons learned from larger planets have allowed researchers to infer that LHS 3844b, an extremely hot terrestrial planet, does not possess a substantial atmosphere (Kreidberg et al. 2019), further atmospheric characterization of small rocky planets is currently not possible. However, terrestrial planet characterization is expected to be achievable with proposed upcoming space missions such as the *James Webb Space Telescope* (JWST, Gardner et al. 2006), the *Large UV/Optical/IR Surveyor* (LUVOIR,

Bolcar et al. 2016), the *Habitable Exoplanet Observatory* (HabEx, Mennesson et al. 2016), and the *Origins Space Telescope* (Battersby et al. 2018) along with the *Widefield Infrared Survey Telescope* (WFIRST) if equipped with a starshade (Spergel et al. 2015). With advanced instrumentation, future ground-based missions could also allow for imaging of Earth-sized planets with the *Extremely Large Telescopes* (ELTs, e.g. Kawahara et al. 2012; Snellen et al. 2013, 2015; Lovis et al. 2017; Lin & Kaltenegger 2020). For a recent overview of upcoming missions and their capabilities for characterizing terrestrial planets see Fujii et al. (2018) and Schwieterman et al. (2018).

Simulations of how well these specific missions can constrain atmospheric abundances of Earth-sized planets have been performed extensively by a number of groups for JWST transmission (e.g. Krissansen-Totton et al. 2018; Lustig-Yaeger et al. 2019a) and emission spectroscopy (e.g. Koll et al. 2019), as well as for LUVOIR (Kawashima & Rugheimer 2019) and the ELTs (e.g. Snellen et al. 2015; Lin & Kaltenegger 2020). Along with these, other studies have focused on atmospheric retrieval models designed specifically for Earth-like planets (e.g. Feng et al. 2018; Tremblay et al. 2020). But until these missions begin, efforts have been focused on how to best identify life based off of atmospheric composition and identify the best planets to prioritize for observations (e.g. Hegde et al. 2015; Schwieterman et al. 2016).

1.2 How could we identify life?

During the 1990 Galileo spacecraft’s fly-by of Earth, astronomer Carl Sagan arranged for it to take spectral data of Earth before proceeding to Jupiter. Using this data they were able to “discover” life on Earth, just by looking at the atmospheric composition they

gleaned from spectroscopy, with the signals indicative of life referred to as ‘biosignatures’, such as water, oxygen, and methane (Sagan et al. 1993). This proof of concept experiment demonstrated the ability to detect life via atmospheric characterization, a method that could be extended to exoplanets. With upcoming telescopes like JWST and the ground-based ELTs, we will be able to begin characterizing exoplanet atmospheres, but it will still be difficult, time intensive process, limited to very few planets. So how will we prioritize which planets to assess first?

1.2.1 The habitable zone: a starting point

The habitable zone (HZ) is defined as the distance from a star where liquid water could exist on the surface of a rocky planet, to guide the search for remotely detectable signs of life in a planet’s atmosphere. While planets outside the HZ are by no means not considered habitable, it is unknown if subsurface life in outer planetary systems (e.g. in an ocean under an ice layer) could easily interact with the atmosphere, and thus become remotely detectable to our telescopes over large distances.

The HZ was originally proposed by Huang (1959). Even before exoplanets were discovered this idea was further expanded upon (e.g. Rasool & de Bergh 1970; Hart 1979; Hart & Jakosky 1987; Kasting et al. 1993). It is often now referred to as the liquid water habitable zone (Kasting & Catling 2003), and applies primarily to Earth-like planets, which can maintain geological activity (see e.g. Kasting et al. 1993).

Initial methods of 1D modeling for the HZ were laid out in Kasting et al. (1993), assuming an Earth-like N_2 - CO_2 - H_2O atmosphere, using limits of recent Venus and early Mars as the inner and outer edges, respectively. These limits were invoked from the fact

that there is evidence that both Venus and Mars initially had surface water, although Venus' was lost in a “runaway greenhouse” process (e.g. Ingersoll 1969; Cockell 1999), and Mars' to the lack of a substantial atmosphere (e.g. Kulikov et al. 2007). These Venus/Mars limits are often referred to as the “empirical” HZ, while the “conservative” HZ limits are defined with the inner edge at the runaway greenhouse limit that would result in total water loss (e.g. Kasting 1988; McKay & Stoker 1989; Kasting et al. 1993; Kulikov et al. 2007), and the outer limit where the maximum greenhouse effect could adequately warm a planet with CO₂ (e.g. Kasting et al. 1993) using Earth-like models, which do not account for cloud feedback.

Even now the concept and limits of the HZ are still constantly being reevaluated and expanded upon (e.g. Lammer et al. 2009; Kopparapu et al. 2013). The HZ has been adapted to binary star systems (e.g. Kaltenegger & Haghighipour 2013), stars throughout evolution (e.g. Lopez et al. 2005; Danchi & Lopez 2013; Ramirez & Kaltenegger 2014, 2016), planets with different surfaces (e.g. Madden & Kaltenegger 2020), planets with H₂-dominated atmospheres (Pierrehumbert & Gaidos 2011; Ramirez & Kaltenegger 2017), and CH₄-dominated atmospheres (Ramirez & Kaltenegger 2018).

More computationally intensive 3D models have been able to study the effects of a variety of different parameters on planetary climate including atmospheric circulation, land/ocean fraction, and rotation rate (e.g. Forget & Pierrehumbert 1997; Lorenz et al. 1997; Joshi 2003; Leconte et al. 2013, 2015; Kopparapu et al. 2016; Yang et al. 2017; Gómez-Leal et al. 2018). Though very different in terms of complexity and computation times, 3D and 1D models agree on outer HZ limits (e.g. Kaltenegger 2017). Certain factors such as planetary rotation rate can have a strong impact on inner limits, particularly with slow rotating/tidally-locked planets that can remain cooler due to

Hadley cell expansion (e.g. Yang et al. 2014). For a wide parameter space, however, 1D models which assume effective heat transport from the day to the night side are still reliable and the only way to explore a wide parameter space.

Although it is unlikely that all life in the universe would evolve similarly to life on Earth, thus producing similar gases, beginning our search for life with Earth as the model is not unreasonable, as it is the only life we currently know to exist. It will be a useful tool in prioritizing which planets to atmospherically characterize first.

1.2.2 Which biosignatures are ‘enough’?

The concept of biosignatures as a method for searching for life in the universe was first discussed by Lovelock (1965), Lederberg (1965) and Lippincott et al. (1967). Though there are many different ideas for what a biosignature could consist of, the most commonly used definition is that it must be something purely of biological or anthropogenic origin (Des Marais et al. 2002, 2008). Similar to Carl Sagan’s study of the Galileo spacecraft’s spectroscopic measurements of Earth to look for life (Sagan et al. 1993), several other studies have treated Earth as an exoplanet, in efforts to determine what types of remote measurements are indicative of life (e.g. Kaltenegger et al. 2007; Kaltenegger & Traub 2009; Robinson et al. 2011; Hegde et al. 2015; Schwieterman et al. 2015; Seager et al. 2016; O’Malley-James & Kaltenegger 2018a,b).

The variety of ideas for potential biosignatures include chlorofluorocarbons as markers for anthropogenic pollution (e.g. Lin et al. 2014), land/ocean mapping via time-dependent spectrophotometric measurements (e.g. Ford et al. 2001; Cowan et al. 2009; Kawahara et al. 2012), general atmospheric disequilibrium (e.g. Krissansen-Totton

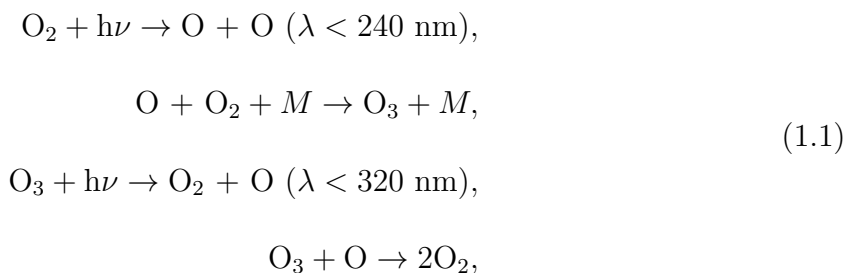
CHAPTER 1. THE SEARCH FOR LIFE IN THE UNIVERSE

et al. 2016), biofluorescence (O'Malley-James & Kaltenegger 2018a), and ocean glint detections at large phase angles (e.g. Williams & Gaidos 2008; Robinson et al. 2010; Zuger et al. 2010). For full reviews of biosignatures and how to evaluate their detections, see such reviews as Des Marais et al. (2002); Kaltenegger (2017); Schwieterman et al. (2018); Catling et al. (2018) or Walker et al. (2018). For the purposes of this thesis, we will focus on gaseous biosignatures pairs as first defined in Lovelock (1965), Lederberg (1965), and Lippincott et al. (1967), and more recently updated in Meadows (2006, 2008).

Below I will briefly describe the Earth's individual chemicals of the primary biosignature gas pairs, their sources, relevant chemistry, and locations of their spectral features.

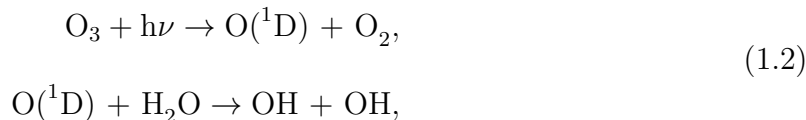
Oxygen/ozone (O_2/O_3)

Modern Earth's atmosphere is roughly 21% oxygen (O_2), with the main source coming from surface life. Ozone (O_3), is created from UV photolysis of O_2 molecules via the Chapman reactions (Chapman 1930):



where M is a background molecule such as N_2 . O_3 , which is the primary mechanism for shielding the surface from harmful UV photons on modern Earth, has its production rates dictated not only by the amount of O_2 , but the amount of UV light emitted by the

planet’s host star. Not only can O₃ be used to predict the amount of O₂ (Leger et al. 1993; Des Marais et al. 2002), but its photolysis also creates hydroxyl (OH) as follows:



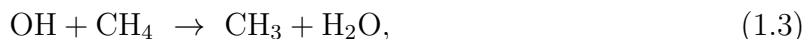
where O(¹D) is an O atom in an excited singlet state. OH is known as the “detergent of the atmosphere”, due to its numerous reactions that take other chemicals out of the atmosphere. Even while comparing planets with the same O₂ abundance, a different stellar environment can cause significantly different O₃ production rates (e.g. Segura et al. 2003; Grenfell et al. 2007; Rugheimer et al. 2013; Grenfell et al. 2014).

The dominant O₂ features are strong, narrow absorption features at 0.76 (A-band), 0.69 (B-band), and 1.27 μm, with a weaker feature at 6.4 μm that overlaps with an H₂O feature.

O₃ has features at complementary wavelengths, with strong features centered at 9.65 μm and from 0.5-0.7 μm (the Chappius band). Further O₃ features are present at 2.05, 2.15, 3.3, 3.6, 4.6, and 4.8 μm.

Methane (CH₄)

Methane (CH₄) is a reducing gas with a lifetime of 10 to 12 years in modern Earth’s atmosphere (Houghton et al. 2004) due to depletion via reactions with oxidizing species and UV photolysis. It has both anthropogenic and natural sources including termites, wetlands, rice fields, and natural gas release from human activities (e.g. Rugheimer et al. 2013). Its primary sink is OH via the reaction:



and is very sensitive to the amount of incident UV. Low stellar UV fluxes can result in a build-up of CH₄ as there is less photolysis and smaller amounts of OH (created via O₃ photolysis).

The strongest CH₄ features in modern Earth's atmosphere are at 1.65, 2.4, 3.3, and 7-8 μm, with weaker bands at 0.6, 0.7, 0.8, 0.9, 1.0, 1.1, and 1.4 μm.

Nitrous oxide (N₂O)

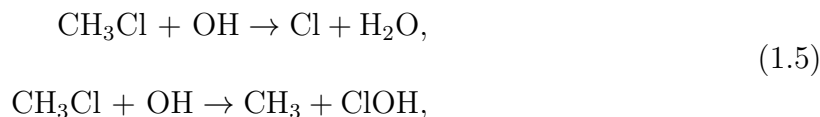
Nitrous oxide (N₂O) is another greenhouse gas that is created naturally in soil via nitrification and denitrification, and also as a result through agriculture. It is an often cited biosignature (e.g. Sagan et al. 1993; Rauer et al. 2011; Rugheimer et al. 2013, 2015a) due to small amounts of abiotic sources. Similarly to CH₄, it could reach high abundances in an Earth-like atmosphere in a stellar environment with low UV levels (e.g. Meadows 2006; Kaltenegger et al. 2007; Segura et al. 2005; Rugheimer et al. 2015a). Its primary sink is via direct UV photolysis and by-products of O₃ photolysis through the reaction:



N₂O has strong bands at 3.7, 4.5, 7.8, 8.6, and 17 μm, and weaker bands between 1.3, 4.2, 9.5, and 10.7 μm. However, most of these features overlap with stronger features from other molecules on modern Earth.

Methyl chloride (CH₃Cl)

Major methyl chloride (CH₃Cl) sources on modern Earth are biological/anthropogenic in origin, including ocean algae, phytoplankton, and a variety of tropical plants, although many of its biological production mechanisms are not well characterized (Rhew & Mazéas 2010). Its primary sources of depletion are UV photolysis and reactions with OH via:



sometimes creating additional atmospheric H₂O in the process.

The main spectral features of CH₃Cl occur at 3.3, 7, 9.7, and 13.7 μm for modern Earth. However, like CH₄ and N₂O, a lower UV environment could cause a build-up of CH₃Cl to detectable levels (Segura et al. 2005; Rugheimer et al. 2013).

Water (H₂O)

Water (H₂O) has always been strongly acknowledged as a necessity for life as we know it. Current measurements and models strongly suggest that it was delivered via comets early on in Earth's history (e.g. Morbidelli et al. 2000; Albarède 2009) and was potentially the location of Earth's first lifeforms (e.g. Baross & Hoffman 1985; Maher & Stevenson 1988; Nisbet & Sleep 2001). Atmospheric H₂O can be created via previously discussed reactions between OH with CH₄ or CH₃Cl (Equations 1.3, 1.5), along with H₂:



Atmospheric H₂O above the ozone layer is primarily removed via UV photolysis, with the H₂ often escaping into space afterward. H₂O has strong, wide absorption bands

CHAPTER 1. THE SEARCH FOR LIFE IN THE UNIVERSE

at 0.9, 1.1, 1.4, 1.9, 5, and 17 μm .

Although all the molecules mentioned above, except for water, individually have strong biological or anthropogenic sources, it is important to consider the possibilities for false positives. O_2 , which is the most abundant in modern Earth's atmosphere of these bioindicators, in particular has many potential false positives, meaning that it has mechanisms that can cause it to build up in the absence of life. Although O_2 is created on Earth primarily by life, on lifeless planets it can still exist in large quantities due to photolysis of oxygen-containing molecules such as CO_2 or H_2O , or from the residual O_2 of an escaping ocean during e.g. a runaway greenhouse stage (e.g. Kasting et al. 1993; Domagal-Goldman et al. 2014; Tian et al. 2014; Wordsworth & Pierrehumbert 2014; Harman et al. 2015; Meadows et al. 2018).

For this reason, it is a combination of atmospheric gases which is indicative of biology and a biosignature, rather than a single atmospheric gas in isolation that would imply life. A joint detection of O_2/O_3 along with CH_4 is currently one of the most robust biosignature pairs (e.g. Sagan et al. 1993; Des Marais et al. 2002; Kaltenegger et al. 2007; Kaltenegger 2017; Schwieterman et al. 2018), and for good reason. Since CH_4 is a reducing species, large amounts of CH_4 and O_2 shouldn't be able to exist together without both of them being continuously outgassed from the planetary surface. While CH_4 can be produced in large quantities geologically, the large amounts of oxygen needed for it to remain detectable in the presence of CH_4 points to the biological origin.

At this point in time we are not aware of any potential false positives for these biosignature combination pairs discussed in Lovelock (1965), Lederberg (1965), and Lippincott et al. (1967) for a temperate planet which does not undergo a runaway

CHAPTER 1. THE SEARCH FOR LIFE IN THE UNIVERSE

greenhouse stage. However, the history of exoplanet discoveries has taught us to be open-minded.

It is important to acknowledge that for a planet around a Sun-like star it will be difficult to detect features indicating life with the next generation of telescopes. For instance, with transmission spectroscopy, H₂O is the most difficult species to find for modern Earth (e.g. Kaltenegger & Traub 2009) as most of Earth's water is below 10 km, a region that can't be probed in transmission spectroscopy in the visible to IR wavelength region (e.g. Kaltenegger & Traub 2009; B  tr  mieux & Kaltenegger 2013). Depending on the wavelength observed, different species might not show absorption features or they might overlap, making identification challenging. The chemical composition as well as spectra of our own planet has also changed considerably throughout its geological evolution (e.g. Kaltenegger et al. 2007; Rugheimer & Kaltenegger 2018; Kaltenegger et al. 2020). For different stellar hosts, the chemical composition as well as the spectra of a planet with Earth's rates differ considerably (e.g. Segura et al. 2003, 2005; Rugheimer et al. 2013, 2015a; Schwieterman et al. 2018).

Throughout all of this we should also remember that Earth has had long periods with life without a unique signature of that life in its atmosphere. Therefore, it that it is unlikely that all life in the universe would have a detectable impact on their atmospheres (e.g. Cockell 2014; Reinhard et al. 2017).

1.3 What role does stellar evolution play?

When characterizing the atmosphere of an exoplanet, it is essential to understand the host star. Even a planet with the exact same initial conditions will evolve to have different atmospheric compositions (and therefore different strengths of biosignatures) if subjected to a different stellar spectral energy distribution (SED) (e.g. Segura et al. 2003, 2005; Rauer et al. 2011; Rugheimer et al. 2013, 2015a; Arney et al. 2017). For example, an Earth-like planet around an M-type star would have different amounts of specific chemicals in its atmosphere compared to an Earth-like planet around an F-type star, even given the same outgassing rates, because of the difference in atmospheric photochemistry. As discussed in the previous section, many atmospheric species such as O_3 , CH_4 , N_2O , and CH_3Cl have production and destruction rates that strongly depend on the amount of UV photons incident upon the atmosphere (e.g. Segura et al. 2003; Grenfell et al. 2007; Rugheimer et al. 2013).

As the influence of the SED of the host star shows, not only is it important to consider the effect of a different type of host star, it is also very important to consider the evolution of the star as well. To date the majority of studies that simulate exoplanet atmospheres concentrate on main sequence (MS) stars (e.g. Segura et al. 2003, 2005; Rugheimer et al. 2013, 2015a,b; Arney et al. 2017), although as the star evolves, the HZ will as well (e.g. Lopez et al. 2005; Danchi & Lopez 2013; Ramirez & Kaltenegger 2016). Even while studying planets around MS M dwarfs, evolution must be considered, as these low mass stars experience an extended amount of time on the pre-MS, where stellar luminosity is significantly higher (e.g. Ramirez & Kaltenegger 2014; Tian et al. 2014).

The post-main sequence is also very important. After all the core hydrogen of a

CHAPTER 1. THE SEARCH FOR LIFE IN THE UNIVERSE

MS star has been converted into helium, fusion stop in the core. Energy leakage from the core becomes greater than the energy generated from the core, causing the core to contract, signaling the end of the MS and the beginning of the star's journey up the red giant branch. Cores of stars with masses greater than $0.4 M_{\odot}$ will eventually reach high enough temperatures (100 million K) as they contract to ignite helium fusion in their cores, ending their trip up the red giant branch. Stars with cores less than $0.4 M_{\odot}$ will not obtain the temperatures necessary for helium fusion and will begin to slowly contract until electron degeneracy pressure becomes great enough to stabilize the core. Stars with masses less than a few solar masses will undergo helium core fusion for several million years until core helium is depleted, allowing the star to once again journey up the red giant branch, on what is called the asymptotic red giant branch. Here they become "planetary nebula" as they shed their envelopes, revealing their extremely hot cores composed mostly of carbon and oxygen, supported by electron degeneracy pressure. This type of stellar remnant is called a "white dwarf".

Although the first discovered exoplanets were found around a stellar remnant - a neutron star (Wolszczan & Frail 1992) - planet searches for such objects have not been prioritized. While no rocky planets have yet been found orbiting post-MS stars, such planets would give us insights into the lifetime of planetary biospheres and therefore provide very interesting targets for characterization.

During the red giant phase of stellar evolution there are significant changes in stellar parameters of surface temperature, radius, and luminosity. Thus planets which were initially frozen at large semimajor axes could provide temperate conditions as their host brightens. While the expulsion of material that leads to a white dwarf stellar remnant has been discussed to potentially disrupt planetary orbits, initially frozen planets could

get scattered inward into the white dwarf HZ, or disks could provide material for second generation planets. These stages of a star's life could provide intriguing insights into the persistence or second genesis of life.

The primary purpose of this thesis is to create a starting place to begin seriously exploring the habitability potential of such red giant stellar hosts and white dwarf stellar remnants. Below I briefly summarize the evolution of red giants and white dwarfs, which will be expanded upon in the following chapters.

1.3.1 Red giant evolution

Red giant branch

As a star begins to climb the red giant branch (RGB) its contracting core is made of He with H burning in the surrounding shell. The large and growing luminosity from this H burning shell causes the outer layers of the star to begin to expand. During H shell fusion He is deposited onto the core, causing mass to increase and contraction to continue. The enveloping H burning shell will continue to become hotter and denser, resulting in higher and higher H burning rates and greatly increasing stellar luminosity. This ever increasing energy flux forces continued expansion of the envelope. The star's surface temperature decreases with expansion until it reaches roughly 3000 K, where it stabilizes due to the H⁻ ion opacity feedback mechanism. A 3000 K blackbody is red, hence the term "red giant star".

As luminosity increases the stellar envelope becomes increasingly more loosely bound, so that radiation pressure drives mass loss. During this time the convection zone

deepens and travels to the point where it reaches depths that have been modified by nucleosynthesis, allowing those materials to be carried to the surface and outer regions of the star. The outermost layers of the atmospheres of late-type giant and super giant stars have temperature and pressures well suited for formation of grains that then can condense out of the gas. The mass loss experienced by these stars is in the form of a slow wind, with $1 M_{\odot}$ stars losing about $0.3 M_{\odot}$ over the course of their time on the RGB. Near the tip of the RGB, core density becomes so large that electron degeneracy pressure begins to be an important contributor to the core's pressure balance. As core contraction continues, degeneracy pressure will eventually begin to dominate thermal gas pressure.

Stars with masses less than $\sim 2 M_{\odot}$ will undergo a "helium flash" in their cores. Following the flash, the onset of this new energy generation in the core causes the core to stabilize, ending the star's journey up the RGB. The helium flash is a direct result of electron degeneracy pressure stronger than the thermal gas pressure. Because helium reaction rates are very sensitive to gas temperature, if at some point the core reaches the required 100 million K, the onset of helium fusion will heat the gas locally. However, since the gas is supported by electron degeneracy pressure, this added gas (ion) temperature does not significantly affect the pressure support, so the gas does not expand and cool as it would within non-degenerate gases. As a result, hot spots become hotter and hotter, leading to runaway helium fusion which only halts when extreme temperatures capable of expanding the core are reached, slowing reaction rates and bringing a balance such that energy leaking from the core is replaced by the core's nuclear energy generation rate, letting the core structure stabilize. These greatly reduced energy generation rates allow the outer envelope to fall back toward the core, forming a horizontal branch (HB) star with effective surface temperatures near 5000 K. Stars with masses greater than

$2 M_{\odot}$ are able to transition more smoothly into He core fusion, and do not undergo a helium flash.

Horizontal branch

He fusion now occurs in the core via the triple alpha process, creating C and O. Since the core has “popped up”, reactions rates within the core are greatly reduced from the helium flash, along with reduced luminosity from the H burning shell as well. The total stellar luminosity of the HB is on the order of 40 to 100 L_{\odot} , factors of 10 to 100 less than at the tip of the RGB. Stars with higher masses experience a greater increase of surface temperature due to higher pressure in their cores. When all of the He in the core is exhausted, the star moves on to the asymptotic giant branch (AGB).

Asymptotic giant branch

Stars leaving the horizontal branch with masses 0.6 to 10 M_{\odot} travel to the AGB and return to a red giant-like state. During this phase the star alternates between He shell burning creates C and O, and at H shell burning creating He shell flashes. This stage is described initially as the early-AGB (E-AGB) and later as the thermally pulsing-AGB (TP-AGB) which are described below.

During the E-AGB He is being fused into C and O in a shell around the core, similar to how H fuses into He in a shell during the RGB. Like on the RGB, the star once again cools and expands from the shell fusion. The TP-AGB begins once the He in the shell is exhausted, the core is made up primarily of C and O, neither of which the interior is hot enough to fuse. This begins a cycle of thermal pulsations that will last throughout the

rest of the RGB. H fusion begins creating He once again in a thin shell around the C and O shell, causing a buildup of He on the core that leads to a He shell flash. During the flash the star will expand and cool, halting the H shell burning, After the flash He shell fusion begins again now that it has been replenished by the H shell burning, until once again it is depleted. This restarts the H thin shell fusion, and the He shell flash cycle, or thermal pulsation, cycle repeats.

Each thermal pulse experienced by the star results in a more loosely bound envelope causing mass loss, as on the RGB. Over half of a star's original mass can be lost during the AGB during these cycles. In addition, this continued mass loss creates a circumstellar envelope that grows from each thermal pulsation. A possible end state of these stars after losing most of their mass and fusion ends as a planetary nebula with a white dwarf as the stellar remnant.

1.3.2 High mass stars after AGB

For the purposes of this thesis, we will only discuss stars that will end fusion permanently after the AGB, but there are more massive stars that follow different paths, which will only be briefly discussed here. Stars with masses greater than $4 M_{\odot}$ achieve internal temperatures in which C can then be fused into heavier elements, and then followed by Ne, O, and finally Si. As the nuclei become more massive, they are less efficient during the fusion process and therefore experience shorter and shorter fusion timescales. For example, a for a $25 M_{\odot}$ star:

- H fusion lasts 7 million years

CHAPTER 1. THE SEARCH FOR LIFE IN THE UNIVERSE

- He fusion lasts 500,000 years
- C fusion lasts 600 years
- Ne fusion last 1 year
- O fusion lasts 6 months
- Si fusion lasts 1 day

after which the core is made of Fe. This cycle must end for even the most massive stars after its core become Fe, which is the nuclei with the highest binding energy per nucleon. Due to this, fusion would absorb energy rather than emitting, meaning that a star's Fe core has reached an end point for fusion energy generation. The core then collapses to a solar-mass object only 10 km in radius - a neutron star supported by neutron degeneracy pressure. This is an eternally stable configuration for core masses less than 2 to 3 solar masses. The gravitational energy released from the core collapse is manifested to the outside universe as a supernova.

1.3.3 White dwarf evolution

After a star halts fusion it can either (a) find an alternative pressure source, or (b) collapse into a black hole. Stellar remnants with masses under $1.4 M_{\odot}$ can balance the inward force of gravity with electron degeneracy pressure according to the Chandrasekhar limit. Masses between $1.4 M_{\odot}$ and $3 M_{\odot}$ will become neutron stars maintained by neutron degeneracy pressure, and more massive stellar remnants will collapse into a black hole. For the purposes of this thesis, we will focus on white dwarfs.

White dwarfs at the core of planetary nebula initially have extremely high surface temperatures ($>100,000$ K), and cool down progressively over time. The primary heating mechanism that slows cooling down occurs when the interior crystalizes at around 4000 K. The latent heat from the phase transition heats the white dwarf, extending the cooling timescale by roughly 30%. After the white dwarf has cooled completely it becomes a so called ‘black dwarf’, but the predicted timescales indicate that the universe is too young for these objects to exist yet.

1.3.4 What does this thesis contribute to our understanding?

The work in this thesis significantly advances our understanding of planetary habitability and potential biosignatures of planets orbiting red giants and white dwarfs. Although previous work had been done on habitable zone evolution for these types of host stars (e.g. Barnes & Heller 2013; Ramirez & Kaltenegger 2016), the studies presented here are the first to model atmospheric changes from these hosts both at snapshots in time as well as throughout their evolution. These results will be essential to plan observations and search for biosignatures as well as interpret observations if we find rocky planets in the HZ of red giants or white dwarfs.

In Part II of this thesis, Chapter 2 calculates the evolving HZ and atmospheric composition for Earth-like planets orbiting a range of red giants, while Chapter 3 simulates reflected light and emission spectra for such planets. Part III discusses habitability timescales and resulting atmospheric properties for planets around white dwarfs in Chapter 4, and biosignatures via transmission spectroscopy in Chapter 5. Conclusions and the future outlook are discussed in Chapter 6.

Part II

Dying to live: habitability around red giants

Chapter 2

Atmospheres and UV Environments of Earth-like Planets throughout Post-main-sequence Evolution

This thesis chapter originally appeared in the literature as Kozakis & Kaltenegger (2019a) in the Astrophysical Journal.

2.1 Introduction

As a star evolves, the orbital distance where liquid water is possible on the surface of an Earth-like planet, the so-called habitable zone (HZ), evolves as well. While stellar properties are relatively stable on the main sequence (MS), post-MS evolution of a star involves significant changes in stellar temperature and radius, which is reflected in the changing irradiation at a specific orbital distance during the red giant branch (RGB), and

CHAPTER 2. HABITABLE PLANETS ORBITING RED GIANTS

for stars massive enough ($> \sim 0.5 M_{\odot}$), the horizontal branch (HB) and the asymptotic giant branch (AGB).

To explore post-MS planetary systems for signs of life, it is critical to understand how the host star influences signs of life in the atmosphere during post-MS evolution. The host star's drastically changing temperature and luminosity not only change the orbital distance of the HZ, but stellar mass loss can also erode a planet's atmosphere through resulting stellar winds. The majority of studies on habitability of rocky planets and moons have focussed on planetary systems around MS stars, with only some work done on habitability around pre-MS and post-MS stars (see e.g. Lopez et al. 2005; Stern & Spencer 2003; Danchi & Lopez 2013; Ramirez & Kaltenegger 2014, 2016), or stellar remnants (e.g. Wolszczan & Frail 1992; Barnes & Heller 2013; Kozakis et al. 2018). However, no study has explored the evolution of the atmospheres and potential detectable biosignatures or UV surface environment for such post-MS planets yet.

Liquid surface water is used because it remains to be demonstrated whether subsurface biospheres, for example under an ice layer on a frozen planet, can modify a planet's atmosphere in ways that can be detected remotely. Although planets located outside the HZ are not excluded from hosting life, detecting biosignatures remotely on such planets should be extremely difficult (see also Ramirez 2018). During post-MS evolution the orbital distance of the HZ often moves out past the system's original frost line, where water can remain in frozen form solely based on stellar irradiation at this orbital distance. In our Solar system 99.99% of H_2O is located beyond the frost line (Stern & Spencer 2003), presenting the opportunity for surface habitability of initially frozen planets and moons in the outer Solar System during the star's post-MS evolution.

CHAPTER 2. HABITABLE PLANETS ORBITING RED GIANTS

As of now there are tens of known gaseous planets around red giant (RG) stars (e.g. Jones et al. 2014), although a terrestrial planet orbiting an RG has yet to be discovered. However, due to the wide separation of the post-MS HZ, such planets could be resolved via direct imaging by upcoming telescopes like the ELT (see also Ramirez & Kaltenegger 2016).

For planets orbiting post-MS stars several studies suggest the possibility of life developing on planets orbiting subgiant or RG hosts (e.g. Lopez et al. 2005), which strongly depends on the time required for life to evolve compared to the star’s post-MS lifetime. Ramirez & Kaltenegger 2016 have added the possibility that ice on initially frozen planets and moons could melt during the RG phase of their host stars, revealing life that initially developed under the surface.

In this study we explore the influence of post-MS stellar irradiation on the climate as well as its surface UV environment for Earth-like planets in the post-MS HZ. We focus on host stars with masses of 1.0 to 3.5 M_{\odot} , which can undergo the post-MS phase in a galaxy the age of our Milky Way. We use observed and modeled spectra of close-by RGs for our stellar models. Some of these RGs can be placed onto one evolutionary track, thus giving us first insight into a planet’s changing environment during the post-MS phase of its host star.

We first model the joint evolution of the star and the orbital distance of its post-MS HZ, along with stellar mass loss and its impacts on planetary orbital radii and atmospheric erosion following Ramirez & Kaltenegger (2016), although with an extension to higher mass stars (1.9 to 3.5 M_{\odot}). We then model the atmospheres of Earth-like planets in the post-MS HZ using a 1D coupled climate/photochemistry code to explore

the chemistry and UV surface environment of our model planets in the post-MS HZ. We focus on the change of atmospheric signatures which can indicate life on a planet: ozone and oxygen in combination with a reducing gas like methane or N_2O (see e.g. review Kaltenegger 2017 for details). We also show climate indicators for our model planets like water and CO_2 , which in addition can indicate whether the oxygen production can be explained abiotically. Section 4.2 explains our methods, Section 4.3 shows our results, and Sections 4.4 and 4.5 discuss and conclude our work.

2.2 Methods

We model the evolution of post-MS host stars and their effects on planetary orbits for 1 Earth-mass planets to calculate how long such a planet could stay within the boundaries of the post-MS HZ, as well as the effect of the host star’s evolution on the atmospheres and UV surface environment of our model planets during the time in the post-MS HZ.

Table 2.1:: Padova catalog stellar lifetimes

| Mass (M_{\odot}) | MS (Myr) | Post-MS (Myr) | RGB (Myr) | HB (Myr) | AGB (Myr) |
|-------------------------|-------------|------------------|--------------|-------------|--------------|
| 1.0 | 11680 | 1011 | 851 | 133 | 27 |
| 1.3 | 4348 | 663 | 529 | 124 | 10 |
| 1.5 | 2901 | 294 | 157 | 125 | 12 |
| 1.7 | 1964 | 236 | 88 | 136 | 12 |
| 1.9 | 1409 | 238 | 52 | 171 | 15 |
| 2.0 | 1205 | 260 | 38 | 206 | 16 |
| 2.3 | 822 | 260 | 9 | 226 | 25 |
| 2.5 | 651 | 201 | 6 | 175 | 20 |
| 3.0 | 396 | 104 | 2 | 92 | 10 |
| 3.5 | 263 | 58 | 1 | 51 | 6 |

2.2.1 Post-MS HZ boundaries

We use stellar evolutionary tracks from the Padova catalog (Bertelli et al. 2008, 2009) which model stellar evolution from the zero-age-main sequence (ZAMS) to the first significant thermal pulse on the AGB. All tracks used in this study have a Solar-like metallicity with $Z = 0.017$ and $Y = 0.26$, from which we obtain the changing luminosity, temperature, and surface gravity, as well as the predicted time points for the beginnings of the RGB, HB, and AGB.

As shown in Table 2.1, timescales for the phases of stellar evolution are highly dependent on stellar mass. While MS lifetimes are always longer for smaller masses, post-MS timescales, particularly the length of the relatively stable HB, do not linearly correlate with host mass. Stars below $2 M_{\odot}$ (0.8 to $2.0 M_{\odot}$) undergo a helium flash, which greatly increases the luminosity in the post-MS phase. Stars that don't undergo the helium flash experience a less extreme luminosity change during the RGB phase, and spend a significantly higher percentage of their post-MS lifetimes on the HB. As a result, the absolute length of the HB peaks for stellar masses of $2.3 M_{\odot}$ (see Table 2.1 and Figure 2.1).

The HZ is defined as the region around one or multiple stars in which liquid water could be stable on an Earth-like rocky planet's surface (e.g. Kasting et al. 1993; Kaltenegger et al. 2013; Kane & Hinkel 2013), facilitating the remote detection of possible atmospheric biosignatures. The width and orbital distance of a given HZ depends to a first approximation on two main parameters: incident stellar flux and planetary atmospheric composition. The incident stellar flux depends on the stellar luminosity, stellar spectral energy distribution, the planet's orbital distance (semimajor axis), and

the eccentricity of the planetary orbit. The warming due to atmospheric composition depends on the planet’s atmospheric makeup, energy distribution, and resulting albedo and greenhouse warming.

In the literature, very different values of stellar irradiance are used as boundaries for the HZ (see review Kaltenegger 2017). Here we use the empirical habitable zone boundaries, based on the Solar flux received by our neighboring rocky planets, Venus and Mars, when we can exclude liquid water on their surfaces. This recent Venus and early Mars irradiation and resulting HZ limits were originally defined using a 1D climate model by Kasting et al. (1993), and updated in Kopparapu et al. (2013) and Ramirez & Kaltenegger (2017, 2018) for MS stars with effective temperatures (T_{eff}) between 2,600 and 10,000 K. Note that the inner limit of the empirical HZ is not well known because of the lack of a reliable geological surface history of Venus beyond about 1 billion years due to resurfacing of the stagnant lid, which allows for the possibility of a liquid surface ocean. However, it does not stipulate a liquid ocean surface.

We calculate the flux boundaries (S_{eff}) of the post-MS HZ boundaries for the evolving stellar luminosity (Table 2.1) during the post-MS. Equation 2.1 gives a third-order polynomial curve fit of the modeling results for host stars as shown in Kaltenegger (2017), based on values derived from models by Kasting et al. (1993) and Kopparapu et al. (2013, 2014), and an extension of that work to 10,000 K by Ramirez & Kaltenegger (2018). The flux values of the HZ are defined by,

$$S_{\text{eff}} = S_{\text{Sun}} + aT^* + bT^{*2} + cT^{*3} + dT^{*4}, \quad (2.1)$$

where $T^* = T_{\text{eff}} - 5780$, and S_{Sun} is the stellar incident values at the HZ boundaries in our Solar System. Table 2.2 (Ramirez & Kaltenegger 2018) shows the constants a ,

CHAPTER 2. HABITABLE PLANETS ORBITING RED GIANTS

b , c , and S_{Sun} needed to derive the stellar flux at the HZ limits valid for T_{eff} between 2,600 to 10,000 K. The inner boundaries of the empirical HZ (recent Venus) as well as an alternative inner edge limit for 3D Global Climate models (3D; Leconte et al. 2013) and the outer limits (early Mars) are all included. The outer HZ limit in 3D and 1D models are consistent and therefore not given in separate columns in Table 2.2 (see e.g. Turbet et al. 2017; Wolf et al. 2018). However climate models still show limitations due to unknown cloud feedback for higher stellar irradiation. Thus, we use the empirical HZ based on recent Venus and early Mars flux limits for our calculations here, even though the inner limit is uncertain as explained before. Table 2.2 provides values to estimate the size of the empirical HZ as well as models of the HZ based on 3D atmospheric models for a planet orbiting our Sun (Leconte et al. 2013) and adapted for different host stars (Ramirez & Kaltenegger 2014).

The orbital distance of the HZ boundaries around a star with luminosity L can be calculated from the incident stellar flux S_{eff} using

$$d = \sqrt{\frac{L/L_{\odot}}{S_{\text{eff}}}}, \quad (2.2)$$

with L measured in Solar units (L_{\odot}) and the orbital distance d in AU.

Table 2.2:: HZ constants from Ramirez & Kaltenegger (2018)

| Constants | Recent Venus limit (inner edge) | 3D model limit (inner edge) | Early Mars (outer edge) |
|------------------|------------------------------------|--------------------------------|----------------------------|
| S_{Sun} | 1.7665 | 1.1066 | 0.324 |
| a | 1.335E-4 | 1.2181E-4 | 5.3221E-5 |
| b | 3.1515E-9 | 1.534E-8 | 1.4288E-9 |
| c | -3.3488E-12 | -1.5018e-12 | -1.1049E-12 |

2.2.2 Planetary semimajor axis evolution

Significant stellar mass loss occurs on the RGB and AGB, both impacting the orbital radii of orbiting planets, as well as potentially eroding planetary atmospheres. We model stellar mass loss on the RGB (\dot{M}_{RGB} in M_{\odot}/year) using the modified Reimers Equation (Reimers 1975; Vassiliadis 1993) and the Baud & Habing (1983) parameterization for the AGB (\dot{M}_{AGB} in M_{\odot}/year) following Ramirez & Kaltenegger (2016),

$$\dot{M}_{RGB} = -\frac{4}{3} \times 10^{-13} \frac{L}{gR_{star}}, \quad (2.3)$$

$$\dot{M}_{AGB} = -\frac{4}{\times} 10^{-13} \frac{M_i}{M_{star}} \frac{L}{gR_{star}}, \quad (2.4)$$

where L is stellar luminosity, g is gravity, and R is radius, and M_i and M_{star} are the initial and current stellar mass, with everything in solar units.

Orbital variation that will occur as a result of the host star's mass loss can be approximated as (assuming the planetary mass is negligible compared to its host's mass),

$$\frac{1}{D} \frac{dD}{dt} = -\frac{1}{M_{star}} \frac{dM_{star}}{dt}, \quad (2.5)$$

where D is the orbital distance. This can be integrated to obtain,

$$D(t) = D_o \frac{M_i}{M_{star}(t)}, \quad (2.6)$$

where D_o is the initial orbital distance and M_i is the initial stellar mass. Using Equations 2.3 and 2.4 to model $M_{star}(t)$, we calculate the planet's $D(t)$ for a given D_o .

2.2.3 Planetary atmospheric erosion

We model planetary atmospheric erosion following Ramirez & Kaltenegger (2016), using the formalism from Canto & Raga (1991) to model planetary atmospheric erosion from stellar winds caused by mass loss. Planetary atmospheric loss per unit time (\dot{M}_a) from the stellar winds is approximated by,

$$\dot{M}_a \approx -2\alpha\pi R_p^2 \rho_w v_w. \quad (2.7)$$

In the stellar wind flow v_w is sound speed, ρ_w is density, and α is the entrainment efficiency. Using the relation of,

$$\dot{M}_{star} = 4\pi D^2 \rho_w v_w, \quad (2.8)$$

we can simplify \dot{M}_a as,

$$\dot{M}_a \approx -2\alpha\pi R_p^2 \frac{\dot{M}_{star}}{4\pi D^2} \quad (2.9)$$

$$= -\frac{\alpha \dot{M}_{star}}{2} \left(\frac{R_p}{D}\right)^2. \quad (2.10)$$

Following Ramirez & Kaltenegger (2016) we use an entrainment efficiency of $\alpha = 0.2$ for our Earth-like atmospheres, assuming an Earth-mass planet with a 1 bar surface pressure. Substituting in \dot{M}_{star} from Equations 2.3 and 2.4 we calculate planetary atmospheric loss throughout the post-MS.

2.2.4 Post-MS stellar model spectra

The stellar input spectra consist of a combination of observed data in the UV (where models poorly represent stellar irradiation) from the International Ultraviolet Explorer

(IUE)¹, an astronomical observatory satellite primarily designed to take ultraviolet spectra. We use type III luminosity class stars drawn from Lopez et al. (2005), Luck & Heiter (2005), and Stock et al. (2018) with available long wave (LW) and short wave (SW) IUE spectra from 1216 to 3347 Å in combination with synthetic spectra from the Pickles Atlas (Pickles 1998) from 3347 to 45450 Å following Rugheimer et al. (2013). Our star sample is drawn primarily from close-by post-MS stars, but includes more distant targets to allow for a more complete sample of observed IUE data for a range of post-MS stars with different spectral types, predicted masses, and evolutionary phases.

Table 2.3:: IUE spectra hosts

| Mass (M _⊙) | Spectral Type | Star Name | Star T _{eff} (K) | Model T _{eff} (K) | Dist. (pc) | Radius (R _⊙) | # SW spectra | # LW spectra | Scale factor | Evolution stage |
|---------------------------|------------------|--------------|------------------------------|-------------------------------|---------------|-----------------------------|-----------------|-----------------|-----------------|--------------------|
| 3.0 | G5 III | HD 74772 | 5118 | 5164 | 70.18 | 12.90 | 2 | 2 | 2.0 | HB |
| 3.0 | G8 III | HD 148374 | 4948 | 5011 | 155.28 | 14.52 | 2 | 1 | 2.2 | HB* |
| 2.3 | K0 III | β Gem | 4865 | 4853 | 10.36 | 8.8 | 12 | 9 | 2.4 | HB |
| 3.0 | K0 III | β Ceti | 4797 | 4853 | 29.5 | 16.78 | 5 | 4 | 2.4 | HB |
| 1.3 | K2 III | ι Draconis | 4445 | 4457 | 31.03 | 11.99 | 1 | 2 | 2.7 | HB |
| 1.3 | K2 III | θ Doradus | 4320 | 4457 | 151 | 16 | 1 | 1 | 1.5 | HB/AGB* |
| 2.0 | K3 III | α Boo | 4286 | 4365 | 11.26 | 25.4 | 29 | 10 | 1.4 | RGB |
| 2.3 | K5 III | γ Draconis | 3989 | 4009 | 47.3 | 53.4 | 4 | 2 | 2.2 | HB/AGB* |
| 2.0 | M5 III | γ Cru | 3626 | 3819 | 27.2 | 84 | 28 | 11 | 2.2 | AGB* |

*Indicates that the target’s evolutionary stage was determined by HR-diagram fitting

We predict the IUE target’s original mass using HR-diagram fitting with the Padova evolutionary tracks and, if available, also use the predicted evolutionary phase from Stock et al. (2018). For stars without an estimated evolutionary phase, we use the predicted age from HR-diagram fitting (see Figure 2.1). Table 3.1 lists stellar data along with the number of short wave (1150 to 1979 Å) and long wave (1979 to 3347 Å) IUE spectra median combined for each target, as well as the scale factor applied to match up the combined spectrum to the corresponding Pickles Atlas synthetic spectrum.

¹<http://archive.stsci.edu/iue>

Figure 2.1 shows the spectra for the 9 post-MS stars in Table 3.1 for an 1 AU-equivalent distance from the star, where a planet would receive the same irradiation as present-day Earth.

2.2.5 Modeling planetary atmospheres and UV surface environments

We use EXO-Prime (see e.g. Kaltenegger et al. 2010), a coupled 1D radiative-convective atmosphere code based on iterations of a 1D climate model (Kasting & Ackerman 1986; Pavlov et al. 2000; Haqq-Misra et al. 2008) and 1D photochemistry model (Pavlov & Kasting 2002; Segura et al. 2005, 2007) developed for rocky exoplanets. Models simulate the effects of stellar and planetary conditions on exoplanet atmospheres and surface environments and are run to convergence following Segura et al. (2005). Model atmospheres extend to an altitude of 60 km (pressure of 1 mbar) divided up into 100 parallel planes using a stellar zenith angle of 60° . Long wave IR fluxes are calculated with

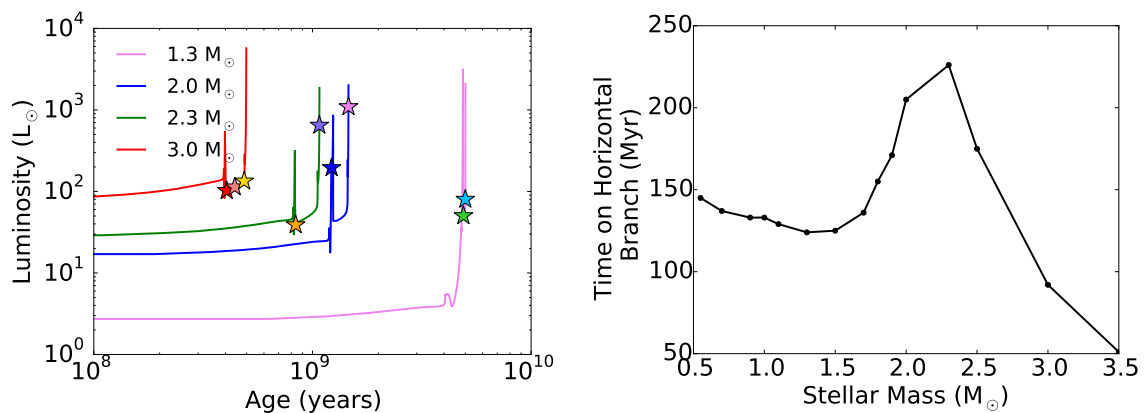


Figure 2.1: (Left) Post-MS IUE targets (marked as stars) fit to the Padova evolutionary tracks and (right) the length of the HB for each specific mass track. More information on targets shown in Table 3.1.

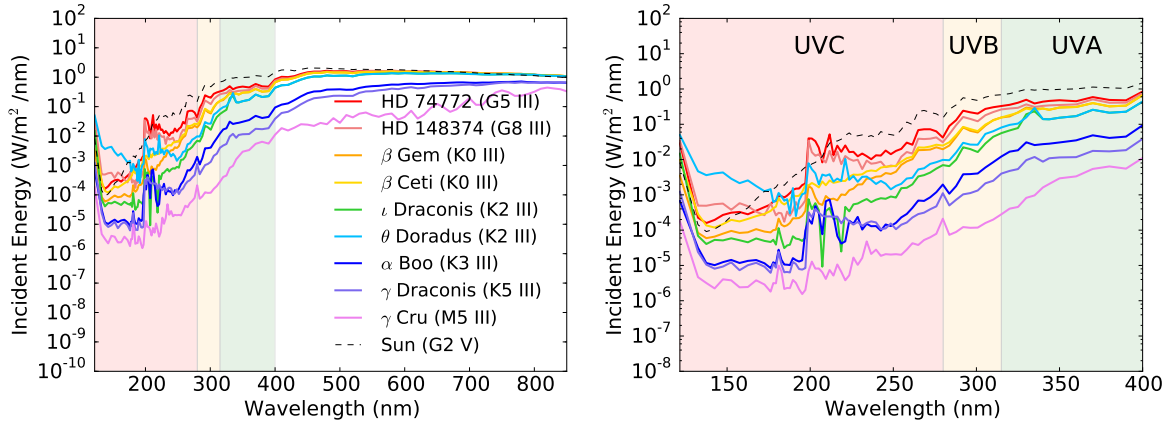


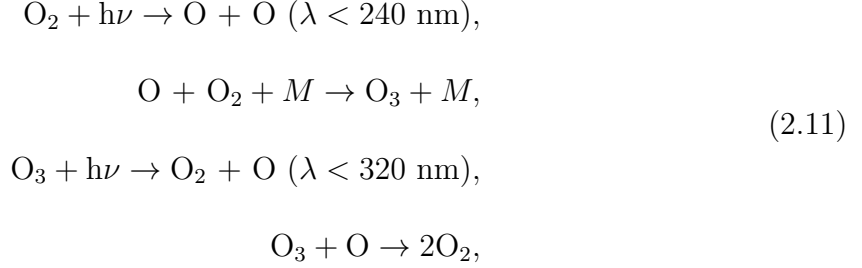
Figure 2.2: Red giant spectra scaled to the Earth-irradiation based on a combination of IUE data and Pickles model spectra for our grid stars (Table 3.1). The UV irradiation present-day Earth receives from the Sun (G2 V) is shown as a black dotted line.

a rapid radiative transfer model, and short wave visible/near-IR fluxes are calculated with a two stream approximation following Toon et al. (1989) with atmospheric gas scattering. The photochemistry code includes 55 chemical species with 220 reactions solved with a reverse-Euler method originally developed by Kasting et al. (1985).

We scale the incident top-of-the-atmosphere stellar flux for our planet models to match the total integrated flux of the Sun-Earth system to compare the effects of post-MS stellar irradiance to present-day Earth. Planetary outgassing rates are kept constant for H_2 , CH_4 , CO , N_2O , and CH_3Cl and maintain constant mixing ratios of O_2 at 0.21 and CO_2 at 3.55×10^{-6} , while N_2 concentrations vary to reach the initial surface pressure model condition (following Segura et al. 2003, 2005; Rugheimer et al. 2013, 2015a,b; Rugheimer & Kaltenecker 2018; Kozakis et al. 2018).

Many reactions in Earth’s atmosphere are driven by the Sun’s UV flux. Some atmospheric species exhibit noticeable features in our planet’s spectrum as a result directly or indirectly from biological activity. Oxygen or ozone in combination with a

reducing gas like methane is currently our best biosignature, indicating biological activity on a temperate rocky planet (see review Kaltenegger 2017). Ozone (O_3) is created and destroyed with UV photons through the Chapman reactions (Chapman 1930),



where M is a background molecule such as N_2 . These reactions are primarily responsible for ozone production on present-day Earth and are dependent on the UV portion of the stellar host's spectrum.

In addition, atmospheric ozone levels determine the amount of UV flux that reaches the planetary surface on present-day Earth (see e.g. Rugheimer et al. 2015a; O'Malley-James & Kaltenegger 2017; Kozakis et al. 2018), which can impact surface life. We focus here in particular on UVB (280-315 nm) and UVC (100-280 nm). UVB irradiation, which can be damaging for surface life is partially shielded by ozone, whereas UVC irradiation, which is energetic enough to cause DNA damage, is almost entirely shielded by ozone, along with being the primary source that creates ozone. We explore the UV environment on the surface of our model planets following Rugheimer et al. (2015a), O'Malley-James & Kaltenegger (2017), and Kozakis et al. (2018) and compare it to present-day Earth's.

2.3 Results

2.3.1 Orbital distance of the post-MS HZ

We modeled the orbital distance of post-MS HZ for host stars of 1.0 to 3.5 M_{\odot} . Then we calculated the initial semimajor required for a planet to spend the maximum amount of time in the post-MS HZ while undergoing semimajor axis evolution (see Equation 2.6). Post-MS stars that undergo a helium flash (0.8 to 2 M_{\odot}) sustain significantly larger luminosity increases (factors of order 1000) when compared to higher mass stars that do not experience helium flashes (factors of order 100). As a result planets around lower mass stars are subject to larger amounts of semimajor axis variation due to higher stellar mass loss rates.

Table 2.4 shows the factor by which stellar luminosity increases on the post-MS, the post-MS HZ boundaries for the beginning and end points of the HB (the most stable part of the post-MS), and the semimajor axis evolution of the orbit of a planet which could spend the maximum possible time in the post-MS HZ. Post-MS HZ orbital distances are comparable for lower mass stars (1.0 and 1.3 M_{\odot}) and higher mass stars (2.0 and 2.3 M_{\odot}) due to the much higher luminosity increase for our grid stars that undergo helium flashes ($< 2 M_{\odot}$). Greater luminosity increases during the post-MS additionally cause higher stellar mass loss rates (Equations 2.3 and 2.4), which in turn cause larger variations in an orbiting planet's semimajor axis for our lower mass grid stars (Equation 2.6).

Table 2.4.: HZ boundaries and semimajor axis evolution

| Track Mass (M_{\odot}) | L factor increase | HB start (AU) | | HB end (AU) | | Semimajor axis* (AU) | | |
|-------------------------------|------------------------|---------------|----------|-------------|----------|----------------------|----------|--------|
| | | Inner HZ | Outer HZ | Inner HZ | Outer HZ | Initial | HB start | HB end |
| 1.0 | 4457 | 5.1 | 12.7 | 5.6 | 13.9 | 10.0 | 12.3 | 12.3 |
| 1.3 | 1258 | 5.6 | 14.0 | 12.0 | 31.0 | 12.5 | 13.8 | 13.9 |
| 2.0 | 126 | 5.2 | 12.6 | 12.2 | 31.0 | 12.2 | 12.3 | 12.3 |
| 2.3 | 68 | 5.0 | 12.0 | 10.5 | 26.4 | 12.0 | 12.0 | 12.0 |
| 3.0 | 74 | 7.5 | 18.3 | 13.3 | 33.3 | 18.2 | 18.2 | 18.2 |
| 3.5 | 73 | 10.5 | 25.6 | 14.7 | 36.7 | 25.0 | 25.0 | 25.0 |

*Semimajor axis values correspond to the orbit that spends the maximum amount of time in the post-MS HZ

2.3.2 Post-MS habitable zone lifetime

For the modeled post-MS HZs and orbital evolution of 1 Earth-mass planets for stars of masses 1.0 to 3.5 M_{\odot} , we explore the longest time a planet can orbit within the post-MS HZ. We also estimate the resulting planetary atmosphere erosion due to the host star’s mass loss (see Table 2.5). Note that the longest time spent in the post-MS HZ does not need to be continuous due to the host stars changing luminosity in the post-MS phase. Thus we distinguish between the time an Earth-mass planet can spend continuously in the post-MS HZ (post-MS CHZ), and the maximum time a planet can spend in the post-MS HZ which is not continuous and can put the planet in a temporary runaway greenhouse state due to the large increase of stellar luminosity during the peak of the RGB (see Figure 3.5 and discussion).

A star with a ZAMS mass of 1.0 M_{\odot} has a total lifetime of 12.7 Gyr, spending only 8% of its life on the post-MS with 851 Myr on the RGB, 133 Myr on the HB, and 27 Myr on the AGB. The initial semimajor axis for a planet leading to the maximal time in the post-MS HZ is 10.0 AU. It spends 66 Myr in the post-MS HZ on the RGB, 22 Myr outside of the post-MS HZ during the RGB peak, where stellar irradiation exceeds the

CHAPTER 2. HABITABLE PLANETS ORBITING RED GIANTS

empirical HZ limits, and then remains in the post-MS HZ for 153 Myr on the HB. The stellar irradiation exceeds the empirical HZ limits again during the AGB. Stellar winds erode about 10% of the planet’s original atmosphere when its stars irradiation exceeds the empirical HZ limits during the AGB.

A star with a ZAMS mass of $1.3 M_{\odot}$ has a total lifetime of 5.0 Gyr, spending 13% of its life on the post-MS with 529 Myr on the RGB, 124 Myr on the HB, and 10 Myr on the AGB. The initial semimajor axis for a planet leading to the maximum amount of time in the post-MS HZ is 12.5 AU. It spends 49 Myr in the post-MS HZ on the RGB, 38 Myr outside of the post-MS HZ during the RGB peak, where stellar irradiation exceeds the empirical HZ limits, and then remains in the post-MS HZ for 105 Myr on the HB and the beginning of the AGB. Stellar winds erode about 5% of the planet’s original atmosphere when its stars irradiation exceeds the empirical HZ limits during the AGB.

Table 2.5:: Post-MS HZ lifetime

| Track Mass (M_{\odot}) | Total post- MS (Myr) | Max HZ (Myr) | Max CHZ (Myr) | Time outside HZ ¹ (Myr) | Atmosphere Eroded (%) |
|-------------------------------|-------------------------|-----------------|------------------|---------------------------------------|--------------------------|
| 1.0 | 1011 | 219 | 153 | 22 | 10 |
| 1.3 | 663 | 154 | 105 | 38 | 5 |
| 2.0 | 260 | 191 | 163 | 50 | 1 |
| 2.3 | 260 | 259 | 257 | 4 | 0.1 |
| 3.0 | 104 | 101 | 97 | 1 | 0.01 |
| 3.5 | 58 | 56 | 56 | 0 | 0.1 |

*Planetary parameters are those of the orbit of maximum time in the HZ

¹ Time spent outside of the HZ during the RGB after initially entering HZ

A star with a ZAMS mass of $2.0 M_{\odot}$ has a total lifetime of 1.5 Gyr, spending 18% of its life on the post-MS with 38 Myr on the RGB, 206 Myr on the HB, and 16 Myr on the AGB. The initial semimajor axis for a planet leading to the maximum amount of time in the post-MS HZ is 12.2 AU. It spends 28 Myr in the post-MS HZ on the

CHAPTER 2. HABITABLE PLANETS ORBITING RED GIANTS

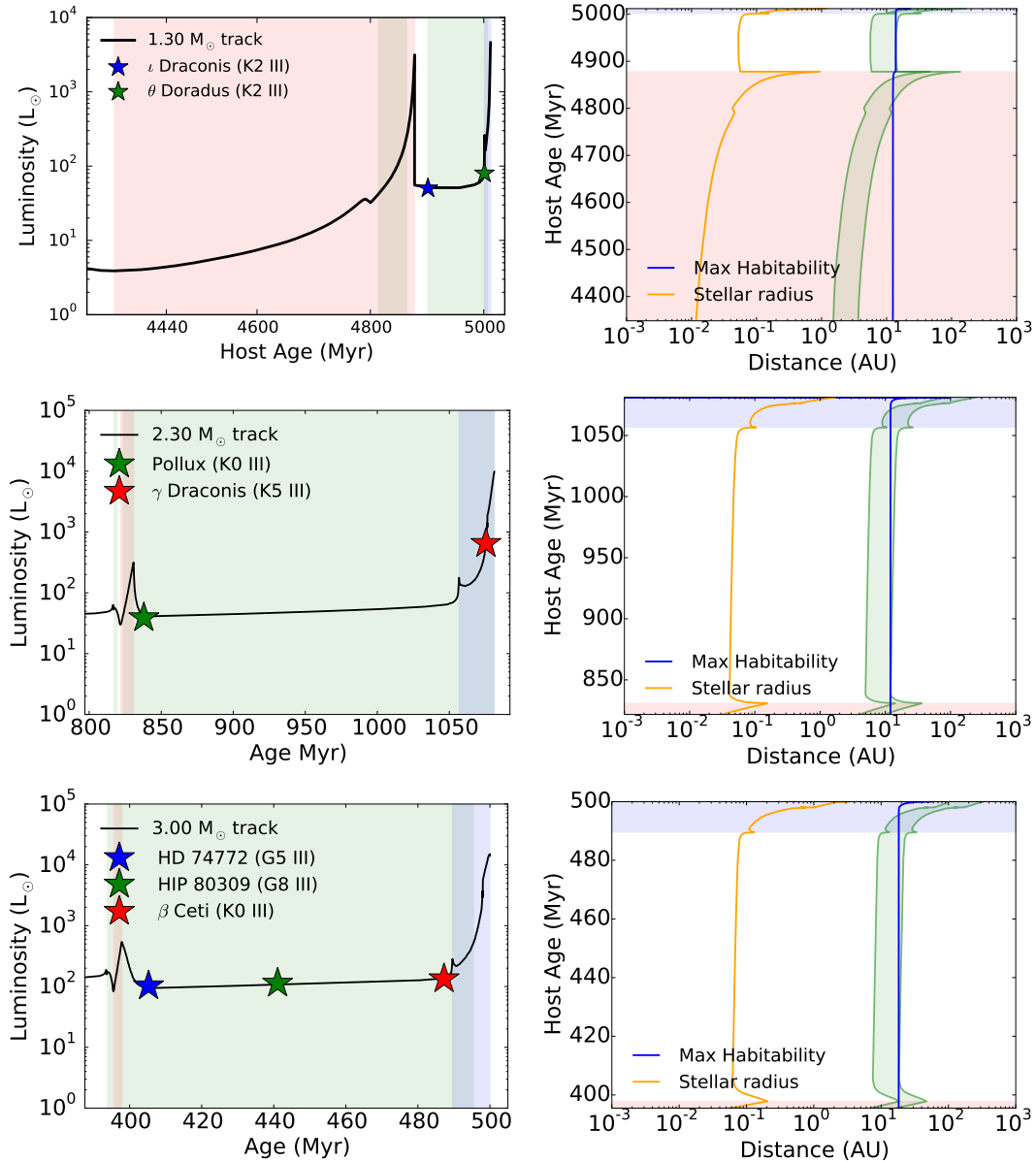


Figure 2.3: (Left) Stellar luminosity versus stellar age during the post-MS with grid stars indicated on the evolutionary track with stars, and (right) evolution of the orbital distances of the post-MS HZ for (top) a 1.3, (middle) a 2.3, and (bottom) a 3.0 M_{\odot} track star. For the plots on the left the red zone indicates the RGB, the blue zone the AGB, and the green zone the time that the model planet passes through the HZ. The points of evolution modeled in Section 2.3.4 are marked with stars. For plots on the right the green zone indicates the changing orbital distance of the HZ, the orange line the evolution of the host star's radius, and the blue line the orbital evolution of an Earth-sized planet spending the maximum amount of time in the HZ.

CHAPTER 2. HABITABLE PLANETS ORBITING RED GIANTS

RGB, 50 Myr outside of the post-MS HZ during the RGB peak, where stellar irradiation exceeds the empirical HZ limits, and then remains in the post-MS HZ for 163 Myr on the HB. Stellar winds erode about 1% of the planet's original atmosphere when its stars irradiation exceeds the empirical HZ limits during the AGB.

A star with a ZAMS mass of $2.3 M_{\odot}$ has a total lifetime of 1.08 Gyr, spending 24% of its life on the post-MS with 9 Myr on the RGB, 226 Myr on the HB, and 25 Myr on the AGB. The initial semimajor axis for a planet leading to the maximum amount of time in the post-MS HZ is 12.0 AU. It spends 2 Myr in the post-MS HZ on the RGB, 4 Myr outside of the post-MS HZ during the RGB peak, where stellar irradiation exceeds the empirical HZ limits, and then remains in the post-MS HZ for 257 Myr on the HB and the beginning of the AGB. Stellar winds only erode 0.1% of the planet's original atmosphere when its stars irradiation exceeds the empirical HZ limits during the AGB.

A star with a ZAMS mass of $3.0 M_{\odot}$ has a total lifetime of 500 Myr, spending 21% of its life on the post-MS with 2 Myr on the RGB, 92 Myr on the HB, and 6 Myr on the AGB. The initial semimajor axis for a planet leading to the maximum amount of time in the post-MS HZ is 18.2 AU. It spends 1.5 Myr in the post-MS HZ on the RGB, 0.5 Myr outside of the post-MS HZ, when stellar irradiation exceeds the empirical HZ limits, 2 Myr in the post-MS HZ on the RGB, 0.3 Myr outside of the post-MS HZ, when stellar irradiation exceeds the empirical HZ limits, and then remains in the post-MS HZ for 97 Myr on the HB and the beginning of the AGB. Stellar winds only erode 0.01% of the planet's original atmosphere when its stars irradiation exceeds the empirical HZ limits during the AGB, due to the wide orbital separation and the brevity of the star's lifetime in our model.

A star with a ZAMS mass of $3.5 M_{\odot}$ has a total lifetime of 321 Myr, spending 18% of its life on the post-MS with 1 Myr on the RGB, 51 Myr on the HB, and 6 Myr on the AGB. Due to a smaller overall luminosity change for stars this massive, a continuous post-MS HZ (CHZ) for a planet exists. The initial semimajor axis for a planet leading to the maximum amount of time of 56 Myr in the post-MS HZ is 25 AU from the RGB to the AGB. Stellar winds erode about 0.1% of the planet's original atmosphere when its stars irradiation exceeds the empirical HZ limits during the AGB, despite the large semimajor axis because of prolonged exposure to high stellar mass loss rates on the AGB.

2.3.3 Planets at Earth equivalent orbital distances

We modeled atmospheres of Earth-like planets at distances where they receive the same integrated flux as present-day Earth ($S_{\text{eff}} = 1$) with surface pressures of 1.0 bar. We focus on the change of atmospheric signatures which can indicate life on a planet, ozone and oxygen in combination with a reducing gas like methane or N_2O , as well as climate indicators such as water and CO_2 , which can also indicate whether the oxygen production can be explained abiotically (see review Kaltenegger 2017). We also explore the amount of UV flux reaching the model planetary surface in the post-MS HZ throughout the host star's evolution later in Section 2.3.4. Temperature and mixing ratios of the resulting model atmospheres are shown for all planet models for our our grid stars in Figure 2.4, with present-day Earth's profiles shown as black dashed lines for comparison.

As a star expands and cools during the post-MS phase, the peak of the stellar spectrum shifts to redder wavelengths, which heat planetary surfaces more efficiently for Earth-like planet with a mostly $\text{N}_2\text{-H}_2\text{O-CO}_2$ atmosphere (see e.g. Kasting et al. 1993).

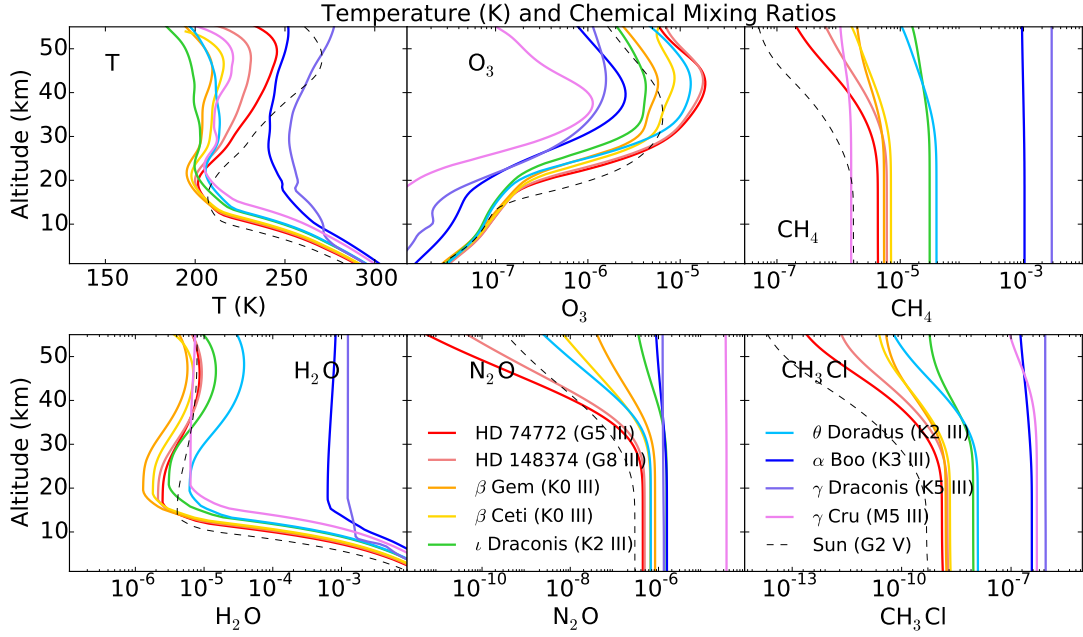


Figure 2.4: Temperature and atmospheric mixing ratio profiles for an Earth-like planet orbiting our grid post-MS stars at the Earth-equivalent distance.

This is partly due to the effectiveness of Rayleigh scattering, which decreases at longer wavelengths. A second effect is the increase in NIR absorption by H_2O and CO_2 as the star’s spectral peak shifts to these wavelengths, meaning that the same integrated stellar flux that hits the top of a planet’s atmosphere from a cool red star warms a planet more efficiently than the same integrated flux from a star with a higher effective surface temperature. This causes planetary surface temperatures to be lower for planets orbiting hotter stars than cooler stars, even with the same amount of total integrated incident flux, as shown in Figure 2.4 and Table 5.1.

Note that due to the drop in stellar temperature during expansion on the RGB the average surface temperature of a post-MS star is lower than for MS stars with similar masses. All grid stars in our study have lower effective temperatures than the Sun, and

as a result all calculated surface temperatures for planets receiving Earth-like irradiation are higher than present day Earth's (shown as a dashed black line), ranging from 1.1 K for the hottest to 18.2 K higher for the coolest post-MS grid star.

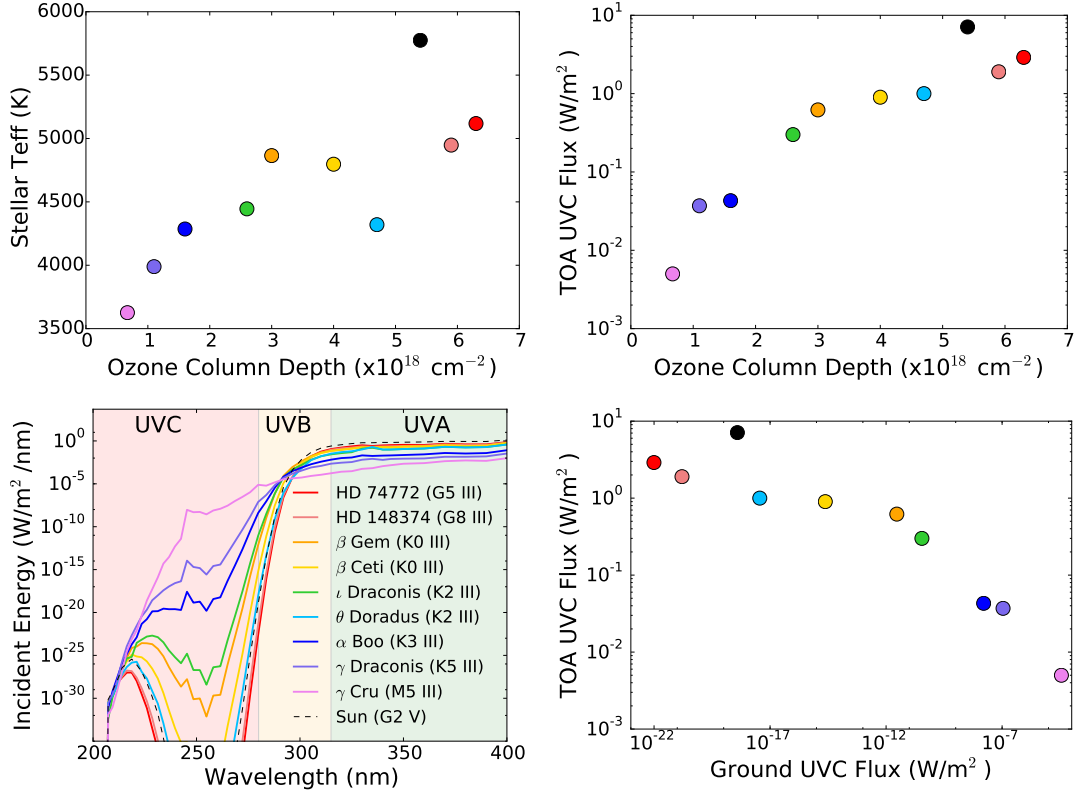


Figure 2.5: (Top, left) Incident top of the atmosphere (TOA) integrated UVC flux versus post-MS grid stars effective temperature, (bottom, left) ground UV flux shown as a function of wavelength for Earth-like planet models, (top, right) TOA integrated UVC flux versus total ozone column depth, and (bottom, right) TOA integrated UVC flux versus ground integrated UVC flux. The different colored dots/lines indicate individual post-MS grid host stars for the planet model, the black dots/line shows present-day Earth for comparison.

Planets orbiting cooler stars in the HZ can receive lower levels of UV flux (see Figure 2.2), impacting ozone production rates. As seen in Equation 4.1 ozone creation requires short wavelength UV photons ($\lambda < 240 \text{ nm}$), resulting in larger amounts of ozone for planets experiencing higher amounts of incident UVC ($100 \text{ nm} < \lambda < 280 \text{ nm}$).

CHAPTER 2. HABITABLE PLANETS ORBITING RED GIANTS

Since our target stars all have lower UVC radiation than the Sun, model atmospheres at the Earth-equivalent distance tend to have lower ozone production rates, resulting in smaller ozone column depths (Table 5.1 and Figure 2.5). The calculated ozone column depth of the planet orbiting in the HZ of the coolest grid star is only 11% that of the hottest grid host star planet in the HZ, and 12% of the column depth on present day Earth.

This lower amount of incident UV flux causes lower photolysis rates in the upper atmosphere with planets orbiting cooler stars experiencing less photolysis related depletion (see Figure 2.4). This effect is particularly relevant for CH_4 , N_2O , and CH_3Cl which are also heavily depleted via reactions with OH, a byproduct of ozone photolysis. The comparable/higher levels of these species should maintain the detectability of both gases in combination as a sign for biological activity on a planet. Our post-MS model planet photochemistry profiles are consistent with studies of cooler MS stars (e.g. Segura et al. 2005; Rugheimer et al. 2013, 2015a).

Table 2.6:: Model Summary for Earth-Equivalent Distances

| Spectral Type | Star Name | Stellar T_{eff} (K) | Surface T_{eff} (K) | UVB TOA W/m^2 | UVC TOA W/m^2 | Ozone Column Depth (cm^{-2}) |
|---------------|-------------------|------------------------------|------------------------------|------------------------|------------------------|---|
| G2 V | Present day Earth | 5775 | 288.2 | 18.9 | 7.1 | 5.4×10^{18} |
| G5 III | HD 74772 | 5118 | 289.3 | 8.3 | 2.9 | 6.3×10^{18} |
| G8 III | HD 148374 | 4948 | 294.5 | 5.8 | 1.9 | 5.9×10^{18} |
| K0 III | β Gem | 4865 | 295.0 | 3.1 | 0.62 | 3.0×10^{18} |
| K0 III | β Ceti | 4797 | 295.5 | 3.2 | 0.90 | 4.0×10^{18} |
| K2 III | ι Draconis | 4445 | 298.6 | 0.96 | 0.30 | 2.6×10^{18} |
| K2 III | θ Doradus | 4320 | 299.1 | 1.4 | 1.0 | 4.7×10^{18} |
| K3 III | α Boo | 4286 | 303.6 | 0.19 | 0.043 | 1.6×10^{18} |
| K5 III | γ Draconis | 3989 | 304.7 | 0.063 | 0.037 | 1.1×10^{18} |
| M5 III | γ Crucis | 3626 | 306.4 | 0.0054 | 0.0050 | 6.7×10^{17} |

Table 5.1 shows the TOA integrated flux for UVB and UVC at the 1 AU-equivalent

distance, as well as the resulting ozone column depth and average surface temperature for Earth-like planetary models with 1 bar surface pressure. It also shows present-day Earth values for comparison in the first line.

UV ground fluxes vary drastically as a function of wavelength due to the wavelength dependent nature of ozone shielding effectiveness. Because we use observed UV data for our grid stars, and these stars are at different stages in their post-MS evolution the correlation between effective temperature and UVC flux is not exact (see all UV fluxes in Table 4.2). However the correlation between ozone column depth and UVC surface irradiation is clearly shown in Figure 2.5.

Although planets with cooler post-MS host stars generally have lower levels of incident UVC flux, the lower amounts also decreases ozone production, allowing a higher percentage of UVB and UVC radiation to reach their surfaces compared to planets orbiting post-MS stars with higher incident UVC flux. The differences in the attenuation percentage is most significant for UVC flux which is almost entirely shielded by ozone. As seen in Figure 2.5 higher incident UVC flux correlates with higher ozone column depth and lower ground UVC as a result of ozone shielding. Note that both β Ceti and θ Doradus have high UVC flux compared to the grid stars with similar surface temperature, and HR-diagram fitting matches both stars to a later stage in the post-MS evolution. All model planets for post-MS host stars with lower effective temperatures than the Sun show higher UVC surface levels than present day Earth, with model planets orbiting cooler post-MS hosts generally experiencing higher levels of surface UVC than similar planets orbiting hotter post-MS hosts (see Table 4.2).

Table 2.7:: UV Integrated Fluxes for Earth-Equivalent Distances

| Spectral Type | Star Name | UVB 280 - 315 nm (W/m ²) | | | UVC 121.6 - 280 nm (W/m ²) | | |
|---------------|-------------------|--------------------------------------|--------|-------------|--|---------|-------------|
| | | ITOA | Ground | % to ground | ITOA | Ground | % to ground |
| G2 V | Present day Earth | 18.9 | 2.2 | 11 | 7.1 | 3.9E-19 | 5.4E-18 |
| G5 III | HD 74772 | 8.3 | 0.92 | 11 | 2.9 | 9.9E-23 | 3.4E-21 |
| G8 III | HD 148374 | 5.8 | 0.76 | 13 | 1.9 | 1.6E-21 | 8.4E-20 |
| K0 III | Pollux | 3.1 | 0.69 | 22 | 0.62 | 2.9E-12 | 4.7E-10 |
| K0 III | β Ceti | 3.2 | 0.59 | 19 | 0.90 | 2.4E-15 | 2.7E-13 |
| K2 III | ι Draconis | 0.96 | 0.26 | 27 | 0.30 | 3.5E-11 | 1.2E-8 |
| K2 III | θ Doradus | 1.4 | 0.27 | 19 | 1.0 | 3.6E-18 | 3.4E-16 |
| K3 III | α Boo | 0.19 | 0.065 | 34 | 0.043 | 1.6E-8 | 3.6E-5 |
| K5 III | γ Draconis | 0.063 | 0.023 | 37 | 0.037 | 3.1E-7 | 0.00084 |
| M5 III | γ Crucis | 0.0054 | 0.0025 | 46 | 0.0050 | 3.6E-5 | 0.71 |

2.3.4 Planetary Atmospheres: post-MS evolution

To explore a planet’s characteristics while orbiting an evolving post-MS star, we modeled the same planet at different points along its host star’s stellar evolution. We include the increase of the initial semimajor axis of the planet, which evolves outwards with stellar mass loss (see Section 2.3.1). We model planets orbiting post-MS host stars on three different mass tracks, which we can match our observed post-MS grid stars to specific stellar masses and evolutionary phase (see Table 3.1). Temperature and photochemical profiles of our model planets are shown in Figure 2.6, a summary of results are shown in Table 2.8, and UV surface flux data is summarized in Table 4.5 and compared to present-day Earth.

Planets which would spend the maximum overall time in the post-MS HZ, orbit initially near the outer edge of the post-MS HZ, warming with increasing incident stellar flux as the luminosity of the post-MS host increases. Note that at the outer edge of the post-MS HZ planets initially experience similar to lower levels of UVC flux than present-day Earth, producing slightly lower amounts of ozone. Although less ozone

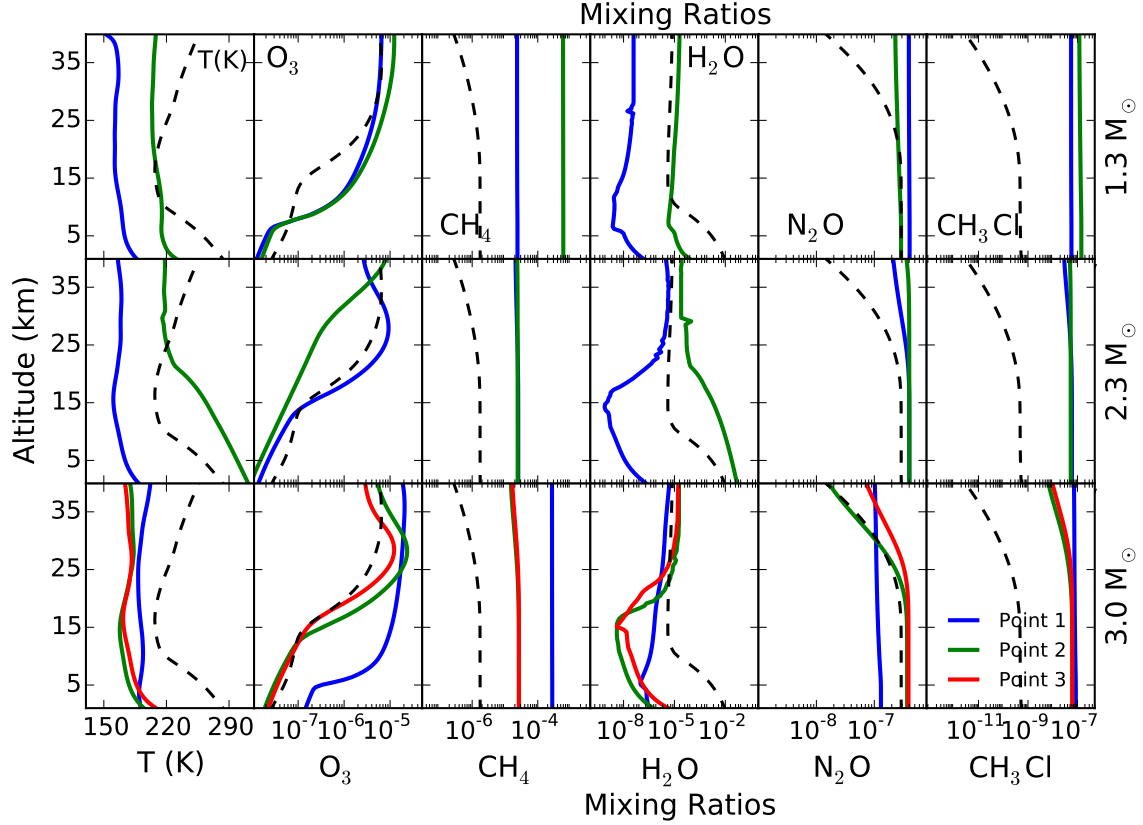


Figure 2.6: Evolving temperature and photochemical profiles of Earth-like planets orbiting post-MS host stars on 1.3 (top), 2.3 (middle), and 3.0 (bottom) mass tracks. Blue lines represent the first point in evolution sampled, green lines the second, and for the 3.0 M_{\odot} track red lines the third.

Table 2.8:: Model Summary throughout post-MS evolution

| Star Name | Track Mass (M_{\odot}) | Evolutionary Stage | Semimajor Axis (AU) | S_{eff} | Surface Pressure (bar) | Ozone Column Depth cm^{-2} |
|-------------------|----------------------------|--------------------|---------------------|------------------|------------------------|-------------------------------------|
| ι Draconis | 1.3 | HB | 13.8 | 0.2689 | 0.95 | 5.1E+18 |
| θ Doradus | 1.3 | HB/AGB | 13.8 | 0.5507 | 0.95 | 1.19E+19 |
| β Gem | 2.3 | HB | 12.0 | 0.2835 | 1.0 | 3.2E+18 |
| γ Draconis | 2.3 | HB/AGB | 12.1 | 1.0647 | 0.99 | 2.5E+18 |
| HD 74772 | 3.0 | HB I | 18.2 | 0.2824 | 1.00 | 5.3E+19 |
| HD 148374 | 3.0 | HB II | 18.2 | 0.3239 | 1.00 | 7.4E+18 |
| β Ceti | 3.0 | AGB | 18.23 | 0.4095 | 1.00 | 4.1E+18 |

shielding exists the lower incident flux produced UV surface environments comparable to present-day Earth for most of our models (Figure 2.6 and Table 2.8). These model atmospheres produce similar to slightly lower amount of ozone but higher amounts of methane than on present-day Earth. N₂O levels are similar while CH₃Cl levels are similar to slightly higher for these post-MS planetary atmospheres. For the 1.3 M_⊙ case there is a slight decrease in UV to the ground from the first to second point in evolution sampled due to an increase in incident UV causing higher ozone production rates. There is an increase of UV to the ground over time for the 2.3 and 3.0 M_⊙ cases resulting from lower amounts of incident UV causing less ozone shielding (see Table 4.5).

Table 2.9:: UV Integrated Fluxes Throughout Post-MS Evolution

| Star Name | Mass (M _⊙) | UVB 280 - 315 nm (W/m ²) | | | UVC 121.6 - 280 nm (W/m ²) | | |
|-------------------|------------------------|--------------------------------------|--------|-------------|--|---------|-------------|
| | | ITOA | Ground | % to ground | ITOA | Ground | % to ground |
| Present day Earth | 1.0 | 18.9 | 2.2 | 11 | 7.1 | 3.9E-19 | 5.4E-18 |
| <i>ι</i> Draconis | 1.3 | 0.26 | 0.052 | 20 | 0.081 | 2.1E-19 | 2.6E-16 |
| <i>θ</i> Doradus | 1.3 | 0.79 | 0.062 | 7.8 | 0.58 | 3.6E-31 | 6.3E-29 |
| <i>β</i> Gem | 2.3 | 0.87 | 0.22 | 25 | 0.18 | 3.7E-12 | 2.1E-9 |
| <i>γ</i> Draconis | 2.3 | 0.067 | 0.020 | 30 | 0.039 | 5.0E-11 | 1.3E-7 |
| HD 74772 | 3.0 | 2.3 | 0.0033 | 0.14 | 0.82 | 2.5E-46 | 3.0E-44 |
| HD 148374 | 3.0 | 1.9 | 0.25 | 13 | 0.60 | 1.3E-23 | 2.1E-21 |
| <i>β</i> Ceti | 3.0 | 1.3 | 0.27 | 21 | 0.37 | 7.7E-15 | 2.1E-12 |

Unlike the profiles shown in Figure 2.4 for models at the Earth-equivalent distance these models are mainly near the outer edge of the post-MS HZ and have lower incident UV flux and therefore lower amounts of upper atmosphere photolysis (Figure 2.6). This is most evident in the nearly vertical profiles of the species most sensitive to photolysis and its products: CH₄, N₂O, and CH₃Cl.

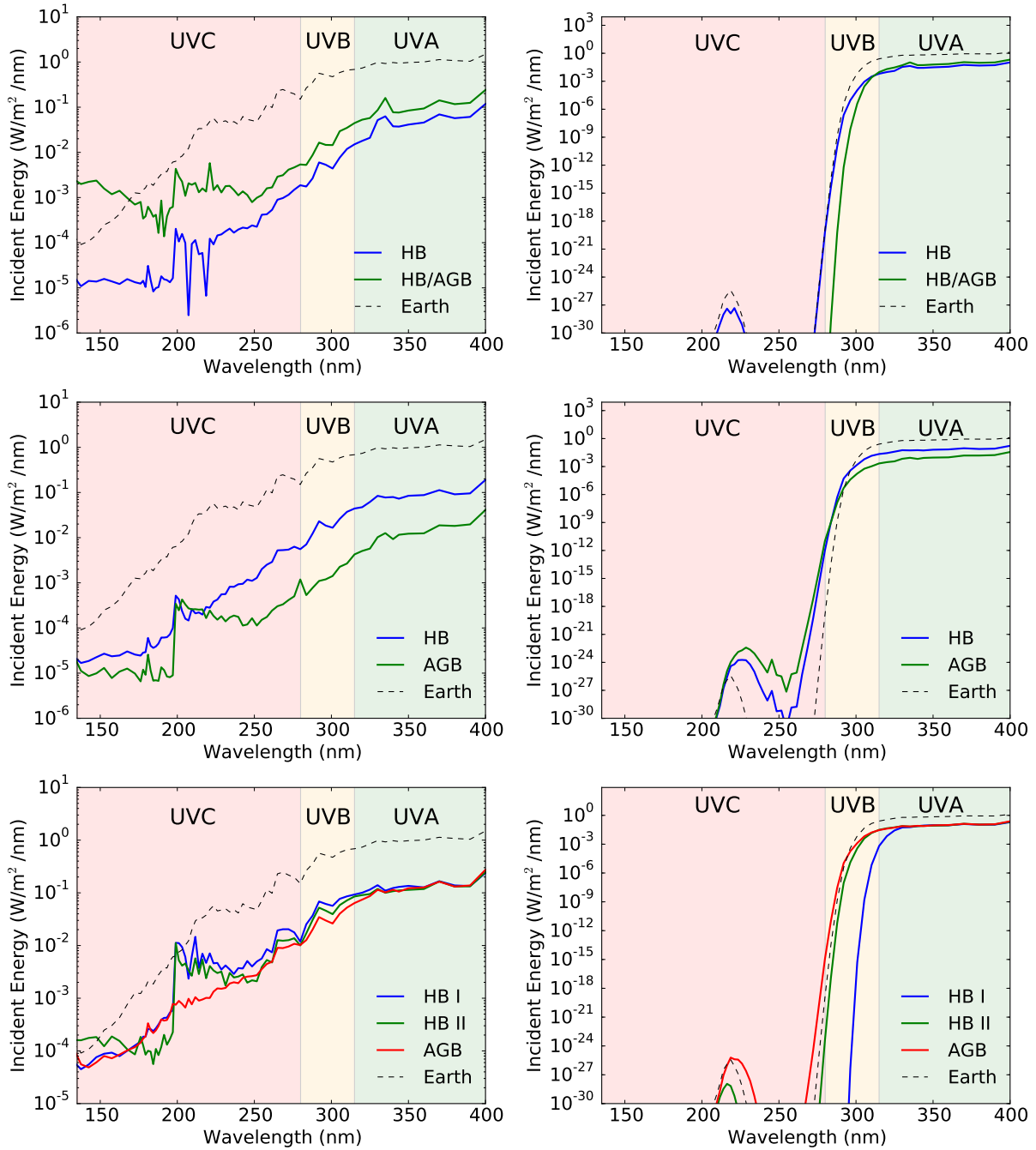


Figure 2.7: Top of the atmosphere and surface UV fluxes for Earth-like planets in the post-MS HZ orbiting post-MS stars. We mimic their host stars evolution by using known stars matched to different parts of their post-MS evolution as marked in Figure 3.5.

2.4 Discussion

2.4.1 How could life form/become detectable on objects

timescales would be too short for the development of life, increasing luminosity during the RGB phase should melt initially frozen surfaces of moons and planets revealing subsurface life (Ramirez & Kaltenegger 2016). Frozen planets and moons are not excluded from hosting life, however it is unknown whether subsurface biospheres, for example under an ice layer on a frozen planet, can modify a planet’s atmosphere in ways that can be detected remotely, thus we concentrate on the liquid water zone in our paper.

2.4.2 Could we directly image planets in the post-MS HZ of red giants?

Upcoming ground-based Extremely Large Telescopes (ELTs) are also designed to characterize exoplanets. Even though a post-MS host star is very bright compared to a MS star, the wider separation of the post-MS HZ when compared to a MS star’s HZ also opens up the possibility of directly imaging planets in the post-MS HZ for closeby systems (see Lopez et al. 2005; Ramirez & Kaltenegger 2016). To further explore this idea, we have compiled a list of post-MS luminosity class III stars within 30 pc and indicate whether these stars have available IUE data (see Table 2.10). We compiled this target list using several published lists (Lopez et al. 2005; Luck & Heiter 2005; Stock et al. 2018) and updated their distances using GAIA DR2 data (Gaia Collaboration et al. 2016).

Comparing the angular separation (θ (arcsec) = a (AU) / d (pc); where a = planet semi-major axis, d = distance to star system) for the angular separation of the 1 AU equivalent distance (Table 2.10) with the inner working angle (IWA) for a telescope, which describes the minimum angular separation at which a faint object can be detected

Table 2.10:: Luminosity class III stars within 30 pc

| Mass (M_{\odot}) | Spectral Type | Star Name | IUE data ¹ | Stellar T_{eff} (K) | Distance (pc) | Radius (R_{\odot}) | 1 AU equiv. (AU) | Ang. Sep. ($''$) | Post-MS (Myr) | HB (Myr) |
|-------------------------|------------------|-----------------------|--------------------------|---------------------------------|------------------|---------------------------|---------------------|-----------------------|------------------|-------------|
| 2.0* | K1.5 III | α Boötis | B | 4286 | 11.3 | 25.4 | 13.98 | 1.24 | 260 | 206 |
| 2.0* | M3.5 III | γ Crucis | B | 3626 | 27.2 | 84 | 33.08 | 1.22 | 260 | 206 |
| 1.3 | K5 III | α Tauri | N | 3910 | 20.5 | 44.13 | 20.21 | 0.99 | 633 | 124 |
| 2.3* | K0 III | β Gem | B | 4865 | 10.4 | 8.8 | 6.24 | 0.60 | 260 | 226 |
| 1.7 | K2 III | α Arietis | S | 4480 | 20.2 | 14.9 | 8.96 | 0.44 | 236 | 136 |
| 2.5 | K0 III | θ Centauri | S | 4980 | 18.0 | 10.6 | 7.87 | 0.44 | 201 | 185 |
| 3.0* | K0 III | β Ceti | B | 4797 | 29.5 | 16.78 | 11.57 | 0.39 | 104 | 92 |
| 1.5 | K2.5 III | ϵ Scorpil | S | 4560 | 23.2 | 12.6 | 7.85 | 0.34 | 294 | 125 |
| 2.3 | K0 III | γ^2 Sagittarii | S | 4769 | 24.9 | 12 | 8.17 | 0.33 | 260 | 226 |
| 1.9 | K0 III | ϵ Cygni | N | 4710 | 23.2 | 10.82 | 7.19 | 0.31 | 238 | 171 |
| 3.0 | G8 III | η Draconis | S | 5055 | 27.3 | 11 | 8.42 | 0.31 | 104 | 92 |
| 1.3 | K2 III | β Ophiuchi | S | 4467 | 24.4 | 12.42 | 7.42 | 0.30 | 663 | 124 |
| 1.5 | K2 III | κ Ophiuchi | S | 4529 | 27.2 | 11 | 6.76 | 0.25 | 294 | 125 |
| 1.5 | K2 III | β Columbae | N | 4545 | 27.8 | 11.5 | 7.12 | 0.26 | 294 | 125 |
| 1.8 | A7 III | γ Boötis | S | 7800 | 26.7 | 3.34 | 6.09 | 0.23 | 157 | 155 |
| 1.7 | K0 III | ν Octantis | S | 4860 | 19.4 | 5.81 | 4.11 | 0.21 | 236 | 136 |
| 1.3 | K1 III | ν^2 CMa | S | 4790 | 19.8 | 4.9 | 3.37 | 0.17 | 663 | 124 |
| 1.8 | A5 III | 111 Her | N | 8153 | 28.3 | 1.83 | 3.64 | 0.13 | 157 | 155 |

¹Key for the IUE data: N = no data, S = short wave data, B = both short wave and long wave data.

*Indicates that target is modeled in this paper

around a bright star we can determine whether planets at such orbital distances could be remotely detected and resolved in the near future. For example the 38 m diameter Extremely Large Telescope should have an IWA of about 6 milliarcseconds (mas) when observing in the visible region of the spectrum (assuming θ IWA $\approx 2(\lambda D)$, where λ is the observing wavelength and D is the telescope diameter). Table 2.10 shows the angular separation of their 1 AU equivalent orbital distance to compare them to predicted inner working angles for ground based telescopes like the ELT with a proposed inner working angle of 6 milliarcseconds (Quanz et al. 2015). Note that we excluded binary systems and variables from our list. The angular separation of the 1 AU equivalent orbital distance during the post-MS for nearby RGs ranges from 1.2 to 0.2 arcseconds, making such observations interesting for upcoming ground-based direct imaging surveys.

2.4.3 Continuous time in the habitable zone

Note that Table 2.5 shows two values for the maximum time a planet orbiting a post-MS host star can stay in the HZ: the time a planet can stay continuously in the post-MS CHZ as well as a longer time period that consists of the sum of the time a planet can spend in the HZ during a star’s post-MS evolution. The sum of time a planet can spend in the post-MS HZ is interrupted by times a planet receives higher luminosity, which should put it into a runaway greenhouse state (see e.g. Kasting et al. 1993), where a planet would boil off surface water and subsequently would lose hydrogen to space. Estimates of the time such water loss would take vary (see e.g. Kasting et al. 1993; Kopparapu et al. 2013). Whether such a runaway greenhouse would be reversible if the irradiation of the star decreases during the HB phase, is unclear, and will depend on many factors, including cloud feedback during the onset of runaway greenhouse stage, which are unknown and will only be constrained once atmospheric observations of such planets are available. Thus Table 2.5 shows both values.

2.4.4 Comparisons to previous studies

Earlier studies have explored the post-MS HZ boundaries and evolution (e.g. Ramirez & Kaltenegger 2016; Danchi & Lopez 2013; Stern & Spencer 2003), however they did not explore planetary climate and UV surface environments on planets in the post-MS HZ. Here we compare our results of post-MS HZ boundary evolution to earlier studies. Note that Ramirez & Kaltenegger 2017, 2018 have expanded the HZ concept to stars with higher surface temperatures, which allows an extension of post-MS HZ calculations to higher mass stars. We calculate post-MS HZ limits, stellar mass loss rates, and planetary

semimajor axis evolution following Ramirez & Kaltenegger (2016), and find consistent results for the overlapping mass range between the two studies (1.0 to 1.9 M_{\odot}). Stern & Spencer (2003) calculates temperate distances and habitability timescales for 1 to 3 M_{\odot} post-MS stars, both of which are consistent with our HZ limits. We also find multiple periods of habitability for a range of semimajor axes during the post-MS, as noted by Danchi & Lopez (2013).

2.5 Conclusions

We explore how long planets could remain in the post-MS HZ for post-MS stars from 1.0 to 3.5 M_{\odot} . We additionally study how the stellar environment would affect the atmospheric composition and potentially detectable biosignatures as well as the surface UV conditions of Earth-mass planets. We model atmospheric erosion and semimajor axis evolution resulting from stellar winds/mass loss.

Less massive grid stars which do undergo a helium flash ($< 2 M_{\odot}$) experience a larger luminosity increase during the post-MS (Table 2.4) causing a more drastic change in the orbital distance of the post-MS HZ compared to the MS HZ as well as higher stellar mass loss rates and semimajor axis variation. We find that the maximum time a planet can spend in the post-MS HZ is between 56 and 257 Myr, for our grid stars, which is highly dependent on the amount of time the host star spends on the relatively stable HB. The wide orbital separation of the post-MS HZ limits atmospheric erosion in our model to about 10% of the initial atmosphere for Earth-like planets with 1 bar surface pressure. Our models are consistent with mass cases from Ramirez & Kaltenegger (2016) that also use the Padova catalog ($\geq 1 M_{\odot}$).

CHAPTER 2. HABITABLE PLANETS ORBITING RED GIANTS

Model planet atmospheres at the Earth-equivalent distance orbiting evolved stars (see Figures 2.4 and 2.5) produce lower amounts of ozone but higher amounts of methane than on present-day Earth, which should maintain the detectability of both gases in combination as a sign for biological activity on a planet. N_2O levels are similar while CH_3Cl levels are similar to slightly higher in the model atmosphere of Earth-like planets orbiting post-MS stars, receiving similar irradiation than Earth does from our Sun.

Lower ozone production results in higher amounts of UVC reaching the surface of our model planets (see Figures 2.4 and 2.5). However, planets on orbits that maximize the overall time in the post-MS HZ spend extended periods of time close to the outer edge of the post-MS HZ, with less incident UVC flux and UVC surface levels comparable to present day Earth (Figures 2.6 and 2.7).

Although the HZ timescales for post-MS stars may not be sufficient for life to develop and evolve, increased luminosity levels cause the post-MS HZ to move past the system's original frost line, potentially melting previously icy planets or moons to reveal subsurface life. In addition, the wider separation of post-MS HZs result in a larger host-planet apparent angular separation, making them interesting targets for direct imaging with upcoming large telescopes, extending the search for habitable planets to older planetary systems.

Chapter 3

High resolution Spectra of Earth-Like Planets Orbiting Red Giant Host Stars

This thesis chapter originally appeared in the literature as Kozakis & Kaltenegger (2019b) on the arXiv, and is currently in press with the Astrophysical Journal.

3.1 Introduction

Although the majority of detected exoplanets orbit main sequence (MS) stars, over 150 exoplanets have already been found around red giant (RG) stars (e.g. Jones et al. 2014; Lopez & Fortney 2016; Grunblatt et al. 2017; Jiang & Zhu 2018). The characteristics of

rocky planets and moons in the post-MS habitable zone (HZ) around RGs are unknown. Therefore, such places could be interesting to search for life (see e.g. Lorenz et al. 1997; Stern & Spencer 2003; Ramirez & Kaltenegger 2016; Kozakis & Kaltenegger 2019a). Until now there have been no spectral models of such planets or moons to explore how to characterize them remotely and assess whether their spectra show biosignatures for such worlds.

When stars exhaust their core hydrogen and leave the MS, their surfaces cool and expand, increasing their overall luminosity and engulfing their inner planetary systems. However, during this time period the orbital distance of their HZ increases past the system's original frost line, where 99.99% of the solar system's water resides (e.g. Stern 2003), suggesting that initially frozen rocky worlds could thaw and become partially to fully ocean-covered worlds during the RG phase of their host star (e.g. Lorenz et al. 1997; Stern & Spencer 2003; Ramirez & Kaltenegger 2016; Kozakis & Kaltenegger 2019a).

The post-MS HZ orbital distance changes significantly during the hydrogen shell fusion on the RG branch (RGB), becomes stable during helium core fusion on the horizontal branch (HB), and returns to rapidly changing on the asymptotic giant branch (AGB) where both hydrogen and helium shell fusion occur. During this period of stability on the HB planets can remain continuously in the post-MS RG HZ for up to 257 million years (Kozakis & Kaltenegger 2019a). Although life might need longer than that time span to originate, with estimates ranging from 0.5 to 1 Gyr (e.g. Furnes et al. 2004; Lopez et al. 2005), subsurface life could evolve under an ice shell during the MS. Such an ice layer could melt during its host star's RG evolution and could reveal such biota through remote observations (Ramirez & Kaltenegger 2016). In our own solar system, both Jupiter and Saturn will remain in the post-MS HZ for the majority of the

CHAPTER 3. PLANETARY BIOSIGNATURES AROUND RED GIANTS

HB, making moons such as Europa, Enceladus, and Titan interesting bodies for future temperate surface conditions in the solar system (see e.g. Lorenz et al. 1997; Stern & Spencer 2003; Ramirez & Kaltenegger 2016; Kozakis & Kaltenegger 2019a).

Several studies explored the nature of the post-MS HZ (e.g. Stern & Spencer 2003; Lopez et al. 2005; Barnes & Heller 2013; Danchi & Lopez 2013; Ramirez & Kaltenegger 2016; Yang et al. 2017) and the resulting planetary atmospheres (Kozakis et al. 2018; Kozakis & Kaltenegger 2019a), but no work had been done to quantify the spectra as well as assess whether the spectra show biosignatures for nominal Earth-like planets orbiting RG stars. Due to the wide orbital separation of the RG HZ, the spectra of such planets could be directly assessed in reflection and emission. Transit probability is significantly lower for RG HZ planets compared to planets in the HZ of MS stars due to the increased orbital distance of the RG HZ.

Assessing biosignature detectability around a wide range of host stars (for MS stars see e.g. reviews by Des Marais et al. 2002; Kaltenegger et al. 2007; Schwieterman et al. 2018; Fujii et al. 2018) is particularly relevant with missions on the horizon that are designed to characterize rocky planet atmospheres, namely JWST (Gardner et al. 2006), ELT (Gilmozzi & Spyromilio 2007), and future mission concepts like ARIEL (Tinetti et al. 2016), Origins (Battersby et al. 2018), HabEx (Mennesson et al. 2016), and LUVOIR (Bolcar et al. 2016).

While the orbital distance of the RG HZ increases significantly due to the higher luminosity of the host RG, increasing the apparent angular separation of such planets compared to MS HZ planets, the contrast ratio between the luminous RG hosts and their HZ planets are also smaller than for similar planets orbiting in the HZ of MS stars.

Although no mission design has yet been optimized for RG HZ planets, the relaxed inner working angle of a coronagraph could counter the increased suppression needed to adjust to the lower contrast ratio at larger angular separations. An adaptation of existing or future concepts could allow probing a new, overlooked parameter space in the search for life in the universe and answer intriguing questions on whether such planets could maintain as well as whether their spectra would show a biosphere in the RG phase of their hosts' evolution.

Note that ground-based high resolution spectroscopy has already characterized atmospheric species for unresolved planets like HD 179949 b using the planet's known motion during the observations (e.g. Snellen et al. 2013; Brogi et al. 2014; Birkby 2018). We extrapolate that a similar approach could be used to counter the increased luminosity of RG hosts to observe their HZ planets, making such planets interesting targets for observations with Extremely Large Telescopes.

As a starting point to explore how to search for life around RG stellar hosts, we simulated Earth-like planets around a variety of RG spectral types (Kozakis & Kaltenegger 2019a). While initially frozen worlds could harbor very different kinds of biota, how life would evolve on such objects is yet unknown. In this study we present spectra for nominal Earth-like planets in the RG HZ both i) at the Earth-equivalent distance, where they receive similar irradiation as modern Earth and ii) for a specific orbital distance in the RG HZ for several points throughout the RG's evolution for stellar mass tracks of 1.3, 2.3 and 3.0 M_{\odot} . For a detailed model description see Kozakis & Kaltenegger (2019a), which discusses the planetary atmospheric models and their corresponding UV surface environments. These models include planetary atmospheric erosion as well as semimajor axis evolution resulting from its host's mass loss during the

CHAPTER 3. PLANETARY BIOSIGNATURES AROUND RED GIANTS

RG phase (Kozakis & Kaltenegger 2019a). Due to the wide orbital separation of the HZ around luminous RGs, planetary atmospheric mass loss via erosion is limited to less than 10% for planets with a 1 bar surface pressure (ibid). A summary of RG hosts and their HZ model data from Kozakis & Kaltenegger (2019a) is shown in Table 3.1.

Table 3.1:: Properties of the selected red giant hosts

| Spectral Type | Star Name | Star T_{eff} (K) | Dist. (pc) | Radius (R_{\odot}) | Planet T_{surf} (K) ^a | 1 AU equiv. dist (AU) | Mass track (M_{\odot}) | a for max HZ (AU) ^b |
|---------------|-------------------|---------------------------|------------|------------------------|---|-----------------------|----------------------------|----------------------------------|
| G5 III | HD 74772 | 5118 | 70.18 | 12.90 | 289.3 | 10.12 | 3.0 | 18.2 |
| G8 III | HD 148374 | 4948 | 155.28 | 14.52 | 294.5 | 10.65 | 3.0 | 18.2 |
| K0 III | β Gem | 4865 | 10.36 | 8.8 | 295.0 | 6.24 | 2.3 | 12.0 |
| K0 III | β Ceti | 4797 | 29.5 | 16.78 | 295.5 | 11.57 | 3.0 | 18.2 |
| K2 III | ι Draconis | 4445 | 31.03 | 11.99 | 298.6 | 7.10 | 1.3 | 12.5 |
| K2 III | θ Doradus | 4320 | 151 | 16 | 299.1 | 8.94 | 1.3 | 12.5 |
| K3 III | α Boo | 4286 | 11.26 | 25.4 | 303.6 | 13.98 | 2.0 | 12.2 |
| K5 III | γ Draconis | 3989 | 47.3 | 53.4 | 304.7 | 25.45 | 2.3 | 12.0 |

^a Planetary surface temperatures were modeled in Kozakis & Kaltenegger (2019a), whereas all other quantities in this table were derived from the host’s stellar parameters

^bSemimajor axis values correspond to a planet’s initial orbital position resulting in the maximum continuous amount of time in the HZ of its RG host, taking stellar mass loss and planetary orbit changes into account

Section 4.2 describes our methods, Section 3.3 discusses the spectra of planets in the post-MS HZ at Earth-equivalent distance as well as throughout their host’s RG evolution, along with a discussion on coronagraph design improvements necessary to enable characterization of RG HZ planets, as well as LUVOIR simulations to simulate required integration time to detect spectral features if current coronagraph designs are used. Section 4.5 discusses and concludes our paper.

3.2 Methods

3.2.1 Stellar Hosts and Planet Atmospheric Spectra Models

We model Earth-like planet reflection and emission spectra orbiting 8 different RG host stars, which have IUE UV data¹. Their incident stellar spectra, which illuminates our model planets, consist of combined IUE and Pickles Atlas (Pickles 1998) luminosity class III spectra (see Table 3.1 and Figure 3.1). We estimate evolutionary phase and mass track using results from Stock et al. (2018) and H-R diagram fitting. For a full description of these stellar spectra see Kozakis & Kaltenegger (2019a). We created the planetary atmosphere models and high resolution spectra using *Exo-Prime* (e.g. Kaltenegger et al. 2020), a 1D coupled climate-photochemistry-radiative transfer code developed for terrestrial planets.

For each planetary atmospheric model, described in Kozakis & Kaltenegger (2019a), *Exo-Prime* generates a high resolution reflection and emission spectra in wavenumber steps of 0.01 cm^{-1} from 0.4 to $20 \mu\text{m}$, using a line-by-line radiative transfer model originally developed to retrieve trace gases in Earth’s atmosphere (Traub & Stier 1976) and later adapted to simulate emergent and transmission exoplanet spectra (e.g. Kaltenegger et al. 2007; Kaltenegger & Traub 2009). For each atmospheric layer line shapes and widths are calculated individually with Doppler- and pressure-broadening with several points per line width. We include the most spectroscopically relevant molecules in our calculations: H_2O , CO_2 , N_2O , NO_2 , HNO_3 , O_3 , CH_4 , O_2 , CO , OH , H_2CO , CH_3Cl , and O , as well as Rayleigh scattering, using the HITRAN 2016 line lists

¹<http://archive.stsci.edu/iue/>

CHAPTER 3. PLANETARY BIOSIGNATURES AROUND RED GIANTS

(Gordon et al. 2017).

We use a Lambert sphere approximation for a disk-integrated planet and model modern Earth-like surfaces for clear sky and 60% coverage of Earth-like clouds (following Kaltenegger et al. 2007). Our modern Earth model surface consists of about 70% ocean, 2% coast, and 28% land, with the land comprised of about 30% grass, 30% trees, 9% granite, 9% basalt, 15% snow, and 7% sand. The 60% coverage by modern Earth-like clouds assumes a distribution of clouds of 40% at 1 km, 40% at 6 km, and 20% at 12 km. We are using the same wavelength dependent cloud albedo for all three cloud layers. Note that we do not change the height or properties of clouds for different host stars. Cloud feedback for different host stars is an area of ongoing research (see e.g. review by Helling 2019). Effects of different cloud coverage and heights on the climate and spectra of Earth-like planets orbiting RG have not been explored in this study, but have been examined for planets orbiting main sequence stars with MS hosts with similar effective stellar surface temperatures (e.g. Fujii et al. 2011; Kitzmann et al. 2011b,a; Zsom et al. 2012; Rugheimer et al. 2013; Kawashima & Rugheimer 2019). All albedo data are from the USGS Digital Spectral Library² and the ASTER Spectral Library³.

All spectra can be downloaded in high resolution (with resolution of a minimum of 100,000 at any wavelength) from the online RG planet spectra catalog (<http://carlsaganinstitute.cornell.edu/data>). Note that we have not added any noise to the spectra to provide theoretical input spectra for any instrument.

For ease of comparison in the figures, we rebin the spectra to a resolution of 140

²<https://www.usgs.gov/labs/spec-lab/capabilities/spectral-library>

³<https://speclib.jpl.nasa.gov>

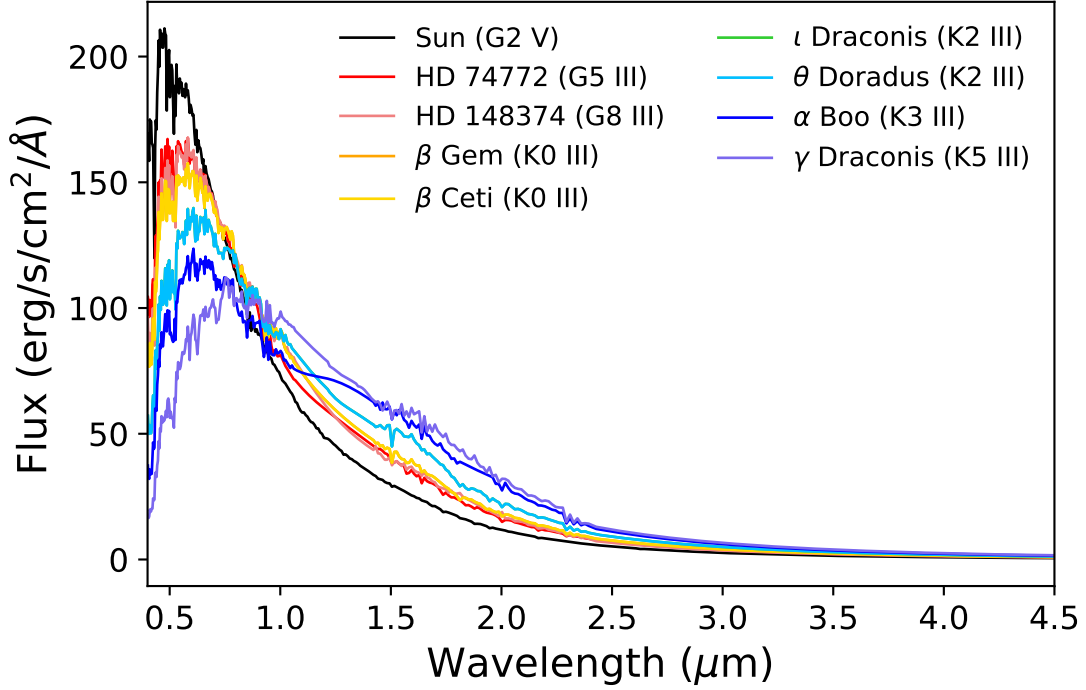


Figure 3.1: Incident stellar spectra of the red giant hosts scaled to the 1 AU-equivalent distance, shown at a resolution of $R = 140$. Red giants with cooler surface temperatures show longer peak wavelengths as well as additional spectral lines due to molecular formation in their atmospheres. See Table 3.1 for information on individual hosts. The solar spectrum is shown for comparison in black.

using a triangular smoothing kernel. We chose the resolution of 140 for our figures based on instruments on JWST (Gardner et al. 2006) with resolution between 100 and 150 and instrument designs for ARIEL (Tinetti et al. 2016), WFIRST (Green et al. 2012), Origins (Battersby et al. 2018), HabEX (Mennesson et al. 2016), and LUVOIR (Bolcar et al. 2016).

3.2.2 Coronagraph simulation of detectability of spectral features

While no existing or proposed instrument concept is optimized to observe RG HZ planets, as an example we use one of the proposed mission concepts, LUVOIR, to estimate the required integration times in the visible to observe spectral features in reflected light for RG HZ planets for i) the current design of one LUVOIR's proposed coronagraphs, and ii) a hypothetical coronagraph design, which allows for a lower contrast ratio by a factor of 100 at the wider orbital separation, corresponding to the RG HZ.

We use a coronagraph noise simulator originally developed for WFIRST-AFTA (Robinson et al. 2016; Lustig-Yaeger et al. 2019a) and system parameters from the LUVOIR Final Report⁴. In particular we use the predicted parameters of LUVOIR-A (15 meters in diameter) and the Extreme Coronagraph for Living Planet Systems (ECLIPS), a coronagraph with imaging spectroscopy for characterizing exoplanetary atmospheres, with a proposed suppression of 10^{10} between its inner working angle (IWA) of $3.5 \lambda/D$ and its outer working angle (OWA) of $64 \lambda/D$. We then hypothesize a coronagraph concept can be optimized for planets in the RG HZ, producing a 10^{12} suppression at the wider RG HZ separation out to an OWA of $230 \lambda/D$.

⁴<https://asd.gsfc.nasa.gov/luvoir/reports/>

3.3 Results: spectra of Earth-like planets orbiting red giant hosts

3.3.1 Spectra of Earth-like planets in the RG HZ receiving modern Earth irradiation

Temperature, chemical mixing ratio profiles (see Figure 3.2), and UV surface environments for our planet models are described in detail in Kozakis & Kaltenegger (2019a). We summarize the major model characteristics of that paper here to link them to the atmospheric features that are shown in the spectra and contrast ratios.

For all models we kept surface outgassing rates at modern Earth levels for H_2 , CH_4 , CO , N_2O , and CH_3Cl and maintain constant mixing ratios of O_2 at 0.21 and CO_2 at 3.55×10^{-6} . The surface pressure is set by the initial 1 bar pressure and consequent atmosphere erosion. Planetary surface temperatures increase with decreasing stellar surface temperature of their RGs hosts due to the shift in peak wavelength to longer wavelengths for cool stars because of the higher efficiency of surface heating via redder light and decreased effectiveness of Rayleigh scattering for longer wavelengths (see e.g. Kasting et al. 1993). This increase in planetary surface temperature for cooler RG hosts increases the amounts of atmospheric H_2O for the warmer model planets.

Planets orbiting hotter RGs receive higher incident UV irradiation, thus show higher ozone (O_3) production, and create more hydroxyl (OH), a by-product of ozone. This leads to lower levels of methane (CH_4) for planets orbiting hotter RGs both due to depletion via OH and higher rates of UV photolysis. Temperature inversion in Earth-like

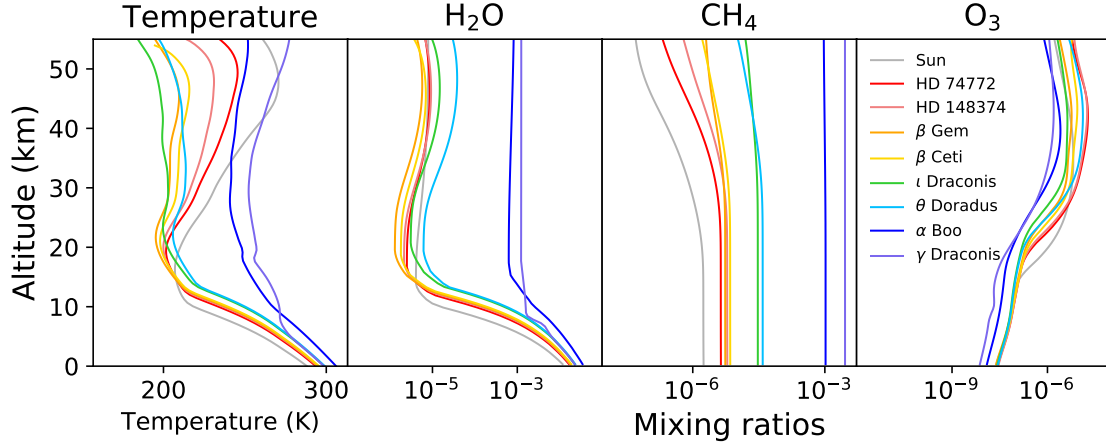


Figure 3.2: Temperature and mixing ratios for H₂O, CH₄, and O₃ for nominal Earth-like planet models orbiting in the habitable zone of 8 red giants within 25pc (T_{surf} 5200 K to 3600 K) at the 1 AU equivalent distance (from Kozakis & Kaltenegger 2019a). RG hosts are ordered from hottest to coolest in the legend, with the modern Earth-Sun system in black for comparison.

atmospheres is primarily caused by atmospheric heating due to ozone absorption and thus becomes more pronounced for planets orbiting hotter RGs. CH₄ concentrations increase in our models for cooler RG hosts, where CH₄ heats the upper atmosphere, further reducing temperature inversion for planets orbiting cooler RG hosts. Several studies have found similar results for planets orbiting in the HZ of MS stars with similar stellar surface temperatures (e.g. Segura et al. 2005; Rugheimer et al. 2015a).

The planet models around the two coolest RGs hosts (α Boo and γ Draconis, a K3 III and a K5 III star, respectively) have high surface temperatures and show stratospheric H₂O mixing ratios of more than 3×10^{-3} , which was initially defined as the boundary of the classical moist greenhouse regime (Kasting et al. 1993). However, recent work using both 1D and 3D models has shown that planet models around cool stars can often reach H₂O mixing ratios within this regime, yet maintain habitable surface

temperatures, particularly around inactive stars (e.g. Kopparapu et al. 2017; Chen et al. 2019). Although planets in the classical moist greenhouse regime have large amounts of stratospheric H_2O that could be susceptible to destruction via photolysis, around inactive cool late K and early M stars the stellar UV flux is low and therefore photolysis rates can remain low. While our models calculate H_2O photolysis rates, they do not include potential H loss as a result.

Figure 3.3 shows the planets' reflection and emission spectra. Atmospheric feature depth in reflection spectra is determined by the abundance of the chemical species and the surface reflectivity for Earth-like atmospheres, while the depth of spectral features in an emission spectra is set by the abundance of the chemical and the temperature at which a chemical absorbs/emits versus the overall emitting temperature of the planet. Higher surface reflectivity results in more reflected starlight and thus deeper spectral features in the visible for the same chemical abundance and incident stellar spectra. Larger temperature contrast between the emitting/absorbing layer compared to the continuum at that wavelength give more depth to spectral features in the infrared for the same chemical abundance. The increasing peak wavelength of the emission for cooler RGs reduces the shortwave incident stellar light, the amount of reflected light and therefore the absorption depth of chemicals in reflected light at short wavelength. Planets orbiting cooler RG hosts also show decreasing temperature inversion in the model atmospheres, reducing the depth of absorption features in the infrared for planets orbiting cooler RGs.

Figure 3.3 shows the spectra of nominal Earth-like planets orbiting RG hosts at the 1 AU equivalent distance, as planetary flux (top row), contrast ratios of the planet to its host star's flux (middle row), as well as the relative absorption of the individual chemicals

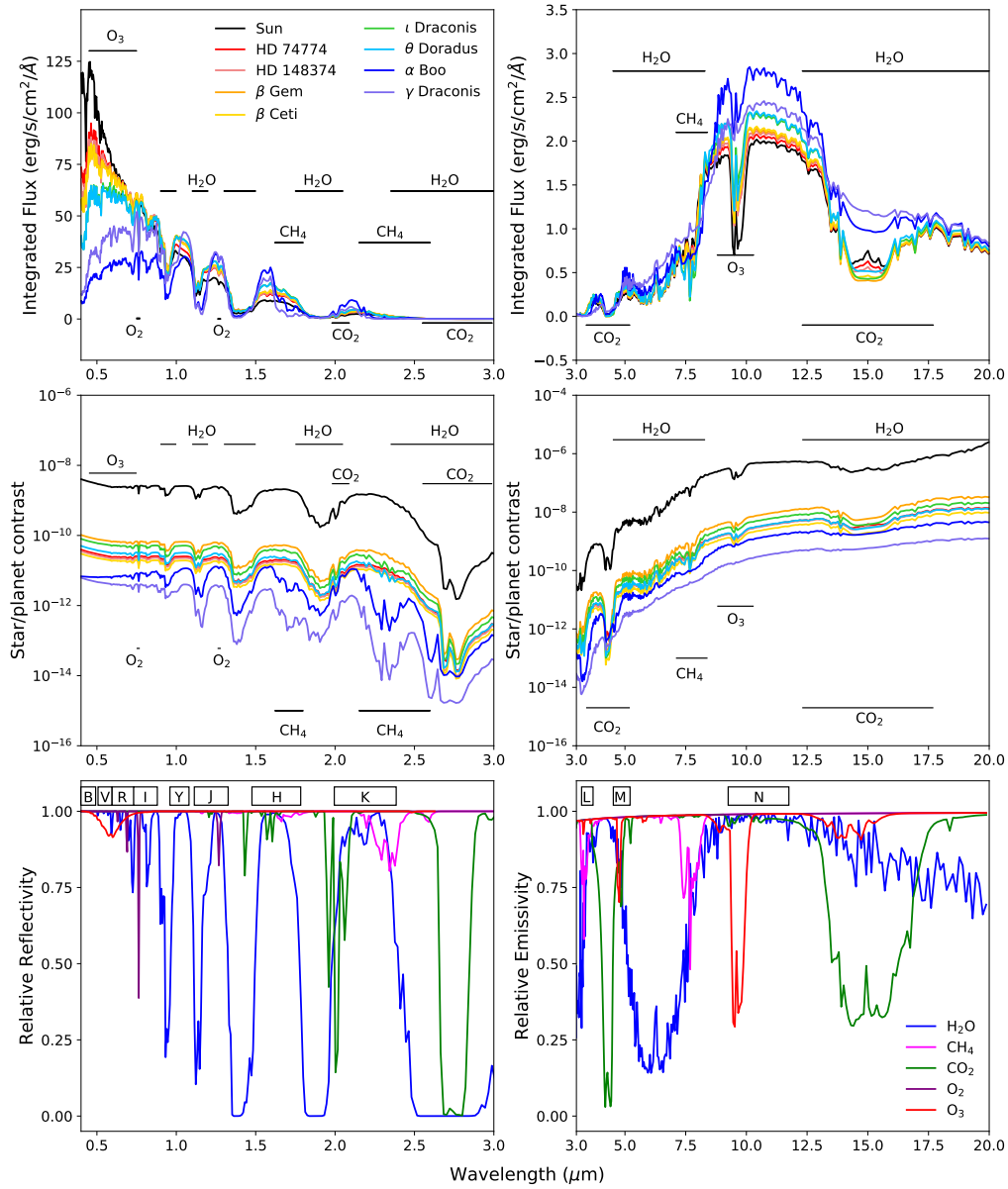


Figure 3.3: Reflection (left) and emission (right) spectra for Earth-like planets orbiting their red giant hosts at the 1 AU equivalent distance. The top row shows the planet’s flux, the middle the contrast ratio between the planet and its host star, and the bottom row the absorption of the major chemical species for the Sun-Earth case are shown individually for reference. RGs are ordered from hottest to coolest in the legend, with the modern Earth-Sun system for comparison.

in the Earth-Sun model for reference, to clarify the overlap of individual spectral lines (bottom row). These individual chemical plots are generated by removing the opacity

of all other molecules from the original atmosphere, and calculating only the opacity due to one particular atmospheric species (see Kaltenegger et al. 2007). Full 0.4-20 μm wavelength coverage for the reflected light and emission spectra are available online at <http://carslaganinstitute.cornell.edu/data>. Due to the host stars' effective temperatures both the effects of reflected light and planetary emission are included in the wavelength range between 2-5 μm , where the contribution of the reflected and emitted flux change over to become the dominant source of the planetary flux. Modern Earth spectra and contrast ratio are shown in black for comparison and labeled "Sun".

At a resolution of $R = \lambda/\Delta\lambda = 140$, shown in (Figure 3.3), all planet spectra show features of H_2O , CO_2 , CH_4 , O_3 and O_2 (top row). Planet spectra in the visible show the lowest flux for planets orbiting cool RG hosts, although their increased surface temperature gives them the largest emission flux in the infrared. The contrast ratio between the host star and its planet generally decreases with decreasing RG surface temperature, making planets orbiting in the HZ of hotter RG hosts easier targets to observe (middle row of Figure 3.3). This is due to the generally larger radii/luminosity of cooler RGs. The contrast ratio in the visible is about 10^3 lower than in the infrared, similar to planets orbiting in the HZ of MS stars. The black line shows the modern Earth-Sun spectra as well as contrast ratio for comparison. While the planetary flux of the modern Earth-Sun system is similar for planets in the HZ of RG hosts, the contrast ratio of the star to planet decreases by about a factor of 15 up to 10^3 for planets orbiting in the HZ of RGs because of the increasing luminosity of the RG hosts, which increase with decreasing surface temperature (see Table 3.1).

H_2O absorption bands are present at 0.9, 1.1, 1.4, 1.9, 5, and 17 μm . The abundance of the H_2O absorption features increase with increasing planetary surface temperature

for cooler RG hosts. In addition, cooler RG hosts provide lower stellar UV environments, decreasing water photolysis. CO₂ shows strong absorption features at 2 and 15 μm . The temperature inversion in the model atmospheres decreases for cooler RG hosts, decreasing the inversion indication in the center of the CO₂ absorption feature at 15 μm for cooler RG hosts.

Hotter RG hosts show increased O₃ production due to higher stellar UV flux, which deepens the 9.6 μm O₃ feature because of the larger temperature difference between the hotter stratosphere and the planet's overall emission temperature for these models. Note that the O₃ feature at 0.6 μm in reflected light is very shallow for all models. Absorption features for CH₄ can be seen at 1.7, 2.4 and 7.7 μm . CH₄ is depleted both through UV photolysis and reactions with OH (a by-product of O₃), causing shallower feature depth in the reflected light at 1.7 and 2.4 μm for hotter RG hosts with more UV. The IR absorption feature at 7.7 μm shows more variation due to the additional effect of the decreasing temperature difference between the absorption layer and the overall planet emission temperature for cooler RG host models.

Absorption features for O₂ (or O₃) in combination with CH₄ (see e.g. Lovelock 1965; Lederberg 1965; Lippincott et al. 1967) can indicate life on a planet like Earth. This combination of features can be seen in Figure 3.3 for all planet models in the RG HZ. The depth of the O₂ feature at 0.76 μm in the reflection spectra becomes difficult to identify at a resolution of 140 for cooler RGs because of the low incident flux level for cool RGs at these wavelengths. As an example of how such features appear in high resolution, Figure 3.4 shows the absorption features of O₂ at 0.76 μm for all planet models at a resolution of $R = 100,000$, which is proposed for several upcoming instruments such as HIRES on the ELT (Gilmozzi & Spyromilio 2007). For ground-based

observations Doppler shift due to the motion of the planet compared to terrestrial features can increase the detectability of spectral features in high resolution (e.g. Snellen et al. 2013; Brogi et al. 2014; Birkby 2018).

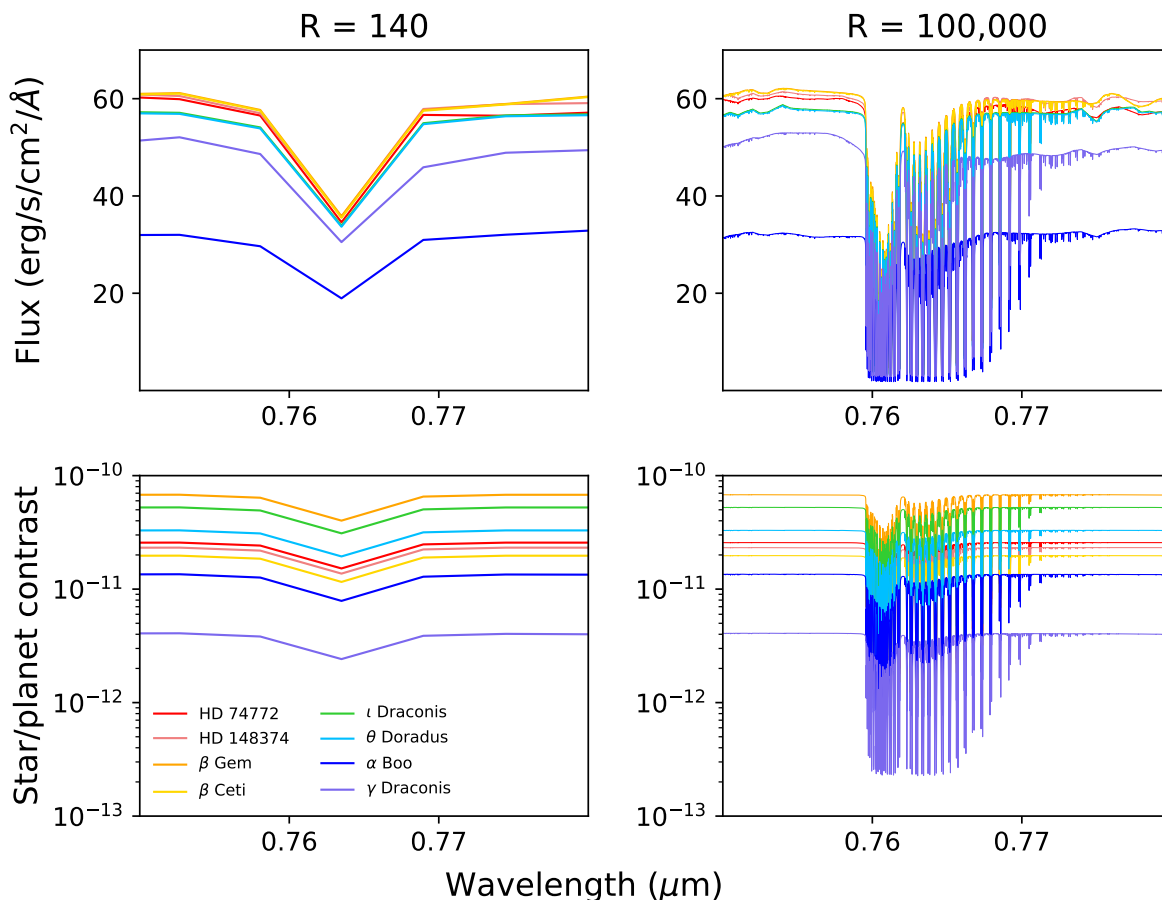


Figure 3.4: O₂ features at 0.76 μm as (top) planet flux and (bottom) star/planet contrast shown at a resolution of (left) 140 and (right) at high resolution of 100,000, as proposed for the HIRES instrument on the ELT.

3.3.2 Spectra of Earth-like planets in the HZ through the red giant's evolution

In this section we discuss the spectra for planet models through their RG's evolution. Temperature and mixing ratios for the major chemicals for all model planets throughout their RGs host star evolution are shown and discussed in Kozakis & Kaltenegger (2019a). We model high resolution spectra for these planets orbiting RG hosts for 3 mass tracks of 1.3, 2.3, and 3.0 M_{\odot} . For each mass track we model the planetary atmosphere at multiple points on the orbit that provides the planet the maximum amount of time continuously in the RG HZ for points in the RG's mass track evolution where we have RG UV data (see Kozakis & Kaltenegger 2019a).

Figure 3.5 shows the evolution of a model planet's spectra set at an initial orbital distance of 12.5 AU from a 1.3 M_{\odot} host star during its RG evolution in planetary flux and planet-to-star contrast ratio as an example for the 3 RG mass tracks modeled. The points in time modeled are shown as star markers on the RG's evolutionary track in the top row. The red zone indicates the RG phase, the blue zone the AGB, and the green zone the time that the specific model planet spends in the HZ during the RG's evolution. Planet spectra for all 3 mass tracks can be downloaded in high resolution from our online spectral database (<http://carlsaganinstitute.cornell.edu/data>).

These planets spend the majority of their time continuously in the RG HZ initially orbit near the outer edge of the RG HZ where the overall incident irradiation is low (Figure 3.5 top right). As a result these planet models initially have cold surface temperatures because we did not change the CO_2 concentration in these models for ease of comparison. Assuming rocky planets in the HZ of RGs could maintain a carbonate

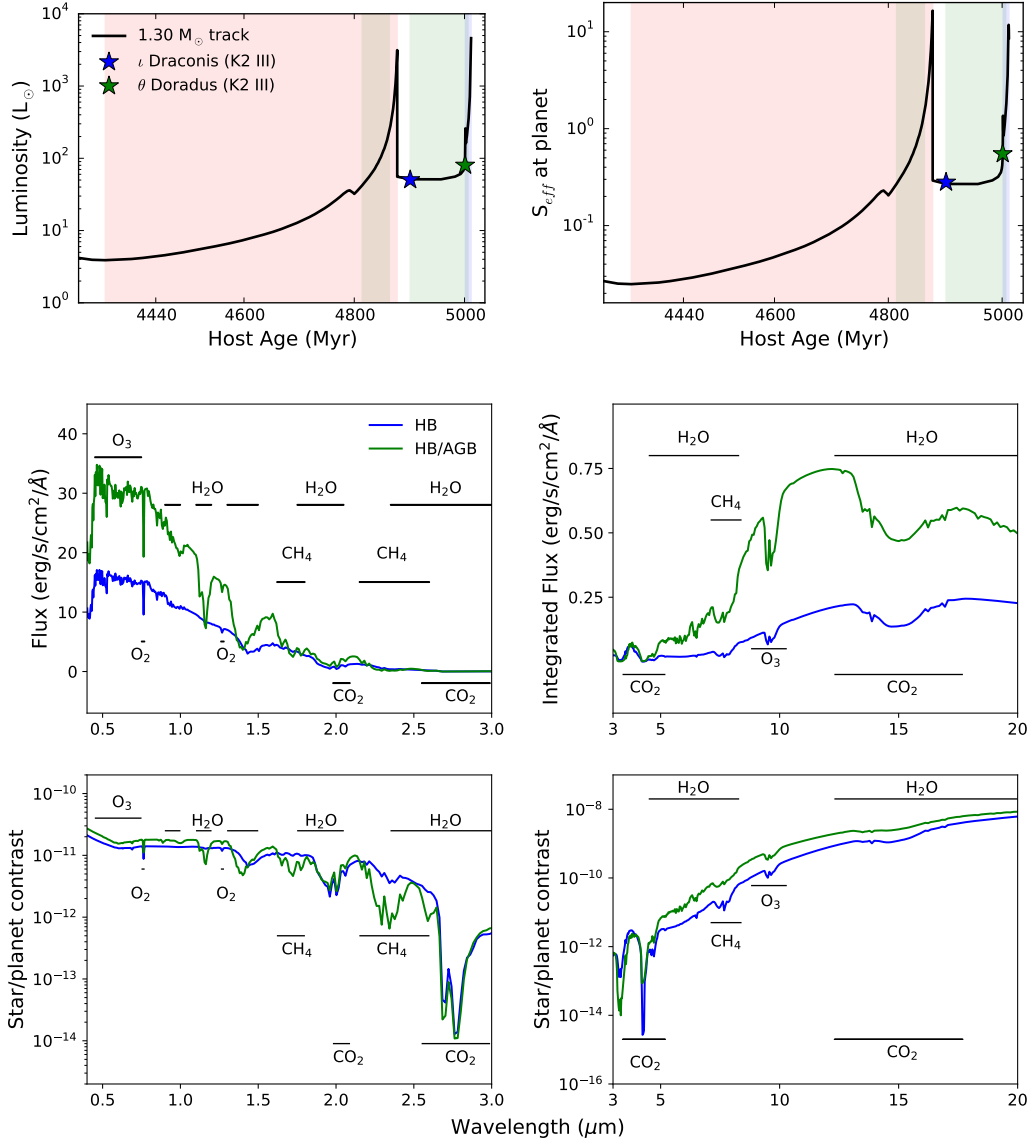


Figure 3.5: Luminosity evolution and spectra of a planet in the HZ of a $1.3 M_{\odot}$ red giant on the orbit giving the maximum amount of time in the RG HZ. The top row shows (left) the luminosity evolution of the red giant host and (right) the changing incident flux upon the planet on an orbit giving it maximum time in the habitable zone. The quantity S_{eff} is the fraction of flux received by the planet compared to modern Earth. The modeled points of evolution are marked with stars. The middle and bottom rows show the spectra of this planet throughout evolution and the star/planet contrast ratios.

silicate cycle until the RG phase of their host, these planets should maintain higher CO_2 concentration in their atmosphere (see e.g. review Kaltenegger 2017). However there

are no models which explore whether the carbonate-silicate or similar cycles could be maintained on frozen planets until the RG phase of their host. Therefore we maintained a modern Earth-analog concentration of CO_2 in our planet models, which initially produce cold environments until the RGs luminosity increases sufficiently to warm the planet.

Cold planetary atmospheres generally have lower H_2O abundance, resulting in initially shallower H_2O spectral features, which become more pronounced with a RGs increasing luminosity and the resulting increase in planetary surface temperature. In the reflected spectra the increase is due to the increasing H_2O abundance, while in the emission spectra the increasing H_2O abundance as well as the increasing planet emission temperature deepen the absorption features. Increasing UV incident flux on the planets over the RG's evolution also increases the O_3 abundance and decreases the CH_4 abundance in the planets' atmospheres (see Figure 3.5 middle).

These model planets initially have low amounts of reflected flux due to the smaller incident amounts of RG host flux at their larger orbital distance and lower emitted flux due to the low planetary surface temperatures at the outer edge of the RG HZ. With increasing incident irradiation at the planet's orbital position from the RG through its evolution (Figure 3.5 top right), the planet's reflected flux increases. The planet's emitted flux also increases due to its increasing surface temperature. Thus a planet in the HZ of a RG displays increasing depth of spectral features in both emitted and reflected flux with its RG's evolution.

Figure 3.5 (bottom) shows that the star to planet contrast ratio stays similar over the RG's evolution for planets at a certain distance within in time they remain in the RG HZ limits, with a slight decrease with the hosts evolution.

3.3.3 Estimated observation times for red giant HZ planets

While no existing or proposed instrument concept has been designed to observe RG HZ planets, as an example of how such planets could be observed, we use one of the proposed coronagraphs of the mission concept, LUVOIR-A, a 15 m diameter space-based telescope concept, to estimate the required integration times in the visible/NIR to observe spectral features in reflected light for RG HZ planets. Using a coronagraph simulator (Robinson et al. 2016; Lustig-Yaeger et al. 2019a) we estimate integration times required to reach a SNR of 5 for our model planets using i) LUVOIR’s ECLIPS coronagraph design, with a proposed suppression of 10^{10} between the IWA of $3.5 \lambda/D$ and the OWA of $64 \lambda/D$, and ii) an imagined hypothetical coronagraph optimized for RG HZ planets, which allows for a larger suppression of 10^{12} at the wider orbital separation of the RG HZ, with an OWA of $230 \lambda/D$. Figure 3.6 shows the results of these simulations for the two closest RGs to Earth, and for all RG hosts used in this paper normalized to a standard distance of 20 pc. About 20 RGs can be found within 30 pc of the Sun (see Table 10 in Kozakis & Kaltenegger 2019a).

Spectra of model planets orbiting cooler RGs generally need longer integration times due to the smaller star-planet contrast ratios (see Figure 3.3). This can be seen comparing integration times of our two closest RGs (seen in the top row of Figure 3.6), β Gem (with the highest contrast ratios of our targets) and α Boo (with the second lowest contrast ratio). For example, to reach a SNR of 5 for the $0.76 \mu\text{m}$ O_2 line with β Gem it would require 12.4 hours of observations with ECLIPS, versus 1.1 hours with our hypothetical optimized coronagraph. For α Boo, located at roughly the same distance, the $0.76 \mu\text{m}$ line cannot be observed with ECLIPS due to the restricting OWA, and

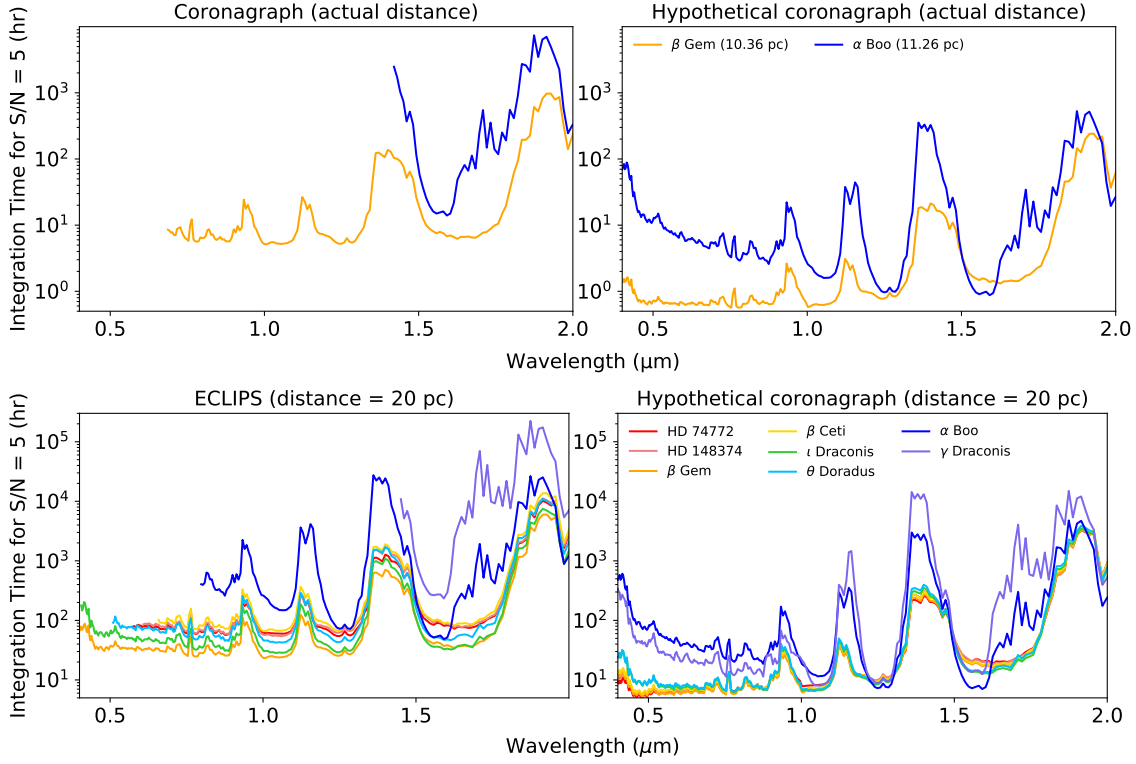


Figure 3.6: Integration times necessary to reach a signal-to-noise ratio of 5 for the 15 m space-based LUVOIR-A concept with (left) the predicted parameters of the ECLIPS coronagraph, and (right) a hypothetical optimized coronagraph with a 10^{12} light suppression at the RG HZ and an OWA of $230 \lambda/D$, for nominal RG HZ planets. Plots on the top row show the two closest RGs to Earth, β Gem and α Boo, at their actual distances of 10.26 pc and 11.36 pc, respectively. The bottom row shows all RG hosts at a standardized distances of 20 pc to compare spectral feature and integration time differences. Wavelengths with no information are due to the system being outside of the OWA for ECLIPS. Longer wavelengths are not shown as the low amount of flux from the star results in very small reflected light fluxes.

would require 6.8 hours of observation with our hypothetical coronagraph, due to the worse contrast ratio.

Assuming that the increased orbital distance of the RG HZ would allow for a increase in light suppression, our envisioned hypothetical, optimized coronagraph, with a 10^{12} suppression at the RG HZ and a large OWA of $230 \lambda/D$, would allow much shorter

integration times than with LUVOIR's ECLIPS. Such a coronagraph would be necessary to effectively characterize RG HZ planets.

3.4 Discussion and Conclusions

While attention is focused on planets orbiting in the HZ of MS stars, detected exoplanets orbiting RG hosts raise the question of the existence of life on initially frozen worlds, persistence of life and how to characterize it on such planets. It is unknown to date, what kind of life could develop and thrive on initially frozen worlds and how such life could evolve during the RG phase of its host on a warming planet. Therefore, as a starting point to explore how to search for life around RG stellar hosts, we simulated Earth-like planets around a variety of RG hosts (Kozakis & Kaltenegger 2019a), both orbiting i) at the distance where they would receive similar irradiation as modern Earth, as well as ii) at a distance which allows for the longest continuous time in the RG HZ.

The high resolution reflection and emission spectra from 0.4 to 20 μm for models of nominal Earth-like planets orbiting in the HZ of RGs (plotted at a resolution of 140 for clarity in Figures 3.3) show atmosphere features of H_2O , CO_2 , CH_4 , O_3 and O_2 . Identification of all spectral features improve with resolution, as shown for one example, O_2 at 0.76 μm in reflected light (plotted at a resolution of 100,000 Figure 3.4 as proposed for spectrographs like HIRES at ELTs).

Our noise-free high resolution spectra (minimum resolution 100,000) is available online to serve as input for simulations of observations for ground- and space-based telescopes. Observation time for specific features will dependent in addition on e.g.

stellar noise and properties and systematics of the observing instrument.

The orbital distance of the RG HZ increases significantly due to the higher luminosity of the host during its RG phase, increasing the apparent angular separation of the RG HZ significantly compared to the MS HZ. However, the contrast ratio between RG hosts and such nominal HZ planets also increases by up to 3 orders of magnitude compared to similar planets orbiting in the HZ of MS stars.

No existing or proposed instrument concept has been envisioned yet to observe terrestrial planets in the RG HZ. Such planets would require larger observation times than planets in the HZ of MS stars, due their RG hosts' increased luminosity. We modeled necessary integration times to reach a SNR of 5 using the proposed future mission concept LUVOIR to quantify the detectibility of such planets (see Figure 3.6). Using predicted parameters of LUVOIR's ECLIPS coronagraph we found that the higher luminosity of RG hosts led to long integration times, and that the larger separation of the RG HZ compared to MS star HZs resulted in spectral cutoffs due to ECLIPS's OWA. Assuming that the increased orbital distance of the RG HZ could allow for a increase in light suppression at that distance, we envision a hypothetical, optimized coronagraph, with a 10^{12} suppression at the RG HZ with a larger OWA, which would reduce the observation times considerably, making terrestrial planet in the HZ of RG interesting targets to observe.

Ground-based high resolution spectroscopy has already characterized atmospheric species for unresolved planets like HD 179949 b using the planets known motion during the observations. We extrapolate that a similar approach could be used to counter the increased luminosity of RG hosts to observe their HZ planets, which would make such

CHAPTER 3. PLANETARY BIOSIGNATURES AROUND RED GIANTS

planets interesting targets for the Extremely large Telescopes like the ELT, GMT and TMT.

Our high resolution spectral database of nominal habitable worlds orbiting evolved RG hosts can be used to explore possibilities for future observations of such planets to assess whether their atmospheres can give us first insights into whether life could survive and thrive on such formerly icy worlds.

Part III

Life after (stellar) death:
habitability around white dwarfs

Chapter 4

UV Surface Environments and Atmospheres of Earth-like Planets Orbiting White Dwarfs

This thesis chapter originally appeared in the literature as Kozakis et al. (2018) in the Astrophysical Journal.

4.1 Introduction

Exoplanets have not yet been discovered orbiting white dwarfs, but have been found around pulsars, indicating that it is possible to have planetary bodies orbiting stellar remnants (Wolszczan & Frail 1992). Exoplanet searches are underway around white dwarfs (WDs) (e.g. Fulton et al. 2014; Fossati et al. 2015; Veras & Gänsicke 2015; Xu

CHAPTER 4. HABITABLE PLANETS ORBITING WHITE DWARFS

et al. 2015), as the similarity with Earth’s size should make Earth-sized exoplanets transiting WDs easier to detect and characterize than such planets around much larger main sequence stars (e.g. via atmospheric profile measurements from transit observations, “weather” modeling from orbital light curves, direct measurement of atmospheric constituents with spectroscopy, etc.) (Agol 2011). Studies of close-by WDs with NASA’s K2 mission (Howell et al. 2014) constrain the occurrence of Earth-sized habitable zone (HZ) planets in those systems to be $< 28\%$ (van Sluijs & Van Eylen 2018a).

Assuming that an Earth-like planet could form or survive around a WD, the WD cooling process will provide a changing luminosity as well as UV environment, which affects an orbiting planet’s temperature, atmospheric photochemistry, and UV surface flux. The luminosity of a cool WD evolves slower than in its initial hot phase, thus cool WDs could provide stable environments for potentially habitable planets (Agol 2011). Several studies have suggested that the unique UV environment would be high enough to sustain complex chemical processes necessary for Earth-like life, while not being strong enough to damage DNA (McCree 1971; Fossati et al. 2012) using estimates assuming present day Earth atmospheres.

Multiple teams have shown that a fraction of WDs show evidence of recent heavy metal pollution, which could signal the existence of either disks or planets (e.g. Koester & Wilken 2006; Koester et al. 2014; Hamers & Portegies Zwart 2016; Klein et al. 2011; Malamud & Perets 2016). For reviews of WD debris disks and pollution see Jura & Young (2014) and Farihi (2016), and for potential post-main sequence planetary evolution see Veras (2016).

Transit simulations using an unchanged present-day Earth-analog atmosphere

composition suggest that the depth of Earth’s biosignatures around a WD would be very strong and detectable by future missions such as *JWST* (Loeb & Maoz 2013). However a WD’s spectral energy distribution (SED) can be significantly different from our present-day Sun. To model the effects of the WD’s emitted flux on the atmosphere as well as the surface UV environment of an exoplanet, we use incident WD SED models at different points of a $0.6 M_{\odot}$ WD’s evolution (Figure 4.1) in our models between 6000 K and 4000 K (Figure 4.2).

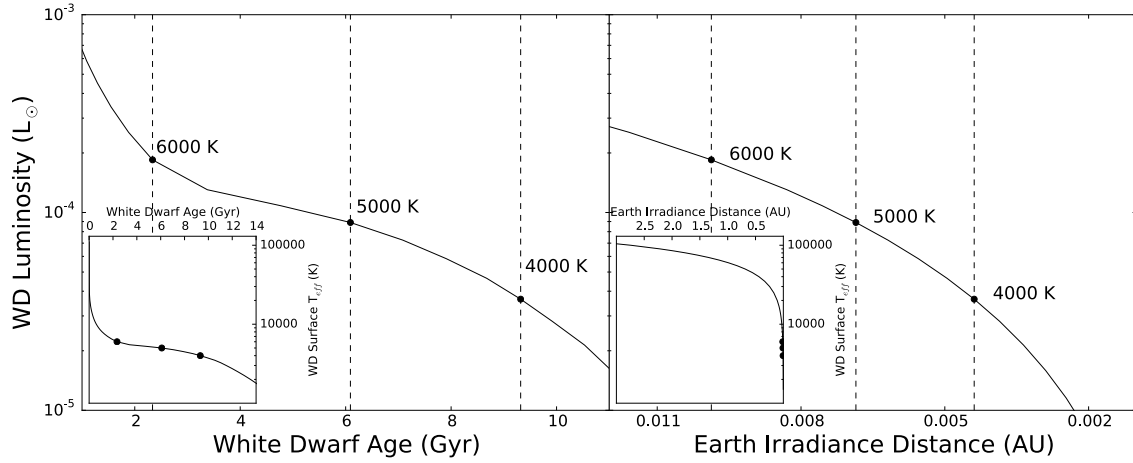


Figure 4.1: White dwarf (WD) luminosity evolution calculated using cooling models from Bergeron et al. (2001) for a $0.6 M_{\odot}$ WD, showing (left) WD luminosity (L_{WD}) versus age of a $0.6 M_{\odot}$ WD model and (right) the 1 AU equivalent orbital distance, where a planet would receive the same irradiance as Earth, for the same WD model. The three points (6000 K, 5000 K, and 4000 K) indicate the WD evolution for the planet models discussed. The inset panels show the same quantities plotted over a larger parameter ranges using the WD’s surface temperature on the y-axis instead of the luminosity (see text).

We model planets orbiting WDs at three points in their evolution (Figure 4.2), with surface temperatures at 6000 K, 5000 K and 4000 K, during which time the WD’s luminosity does not change significantly compared to the early luminosity change in a WD’s evolution (see Figure 4.1). That surface temperature change corresponds to about

7 billion years (Gyr) for a $0.6 M_{\odot}$ WD. We consider planets with eroded atmospheres as well as with higher surface pressure (e.g. super-Earths). We show the atmospheric structure and chemical composition as well as the UV surface fluxes at biologically relevant wavelengths.

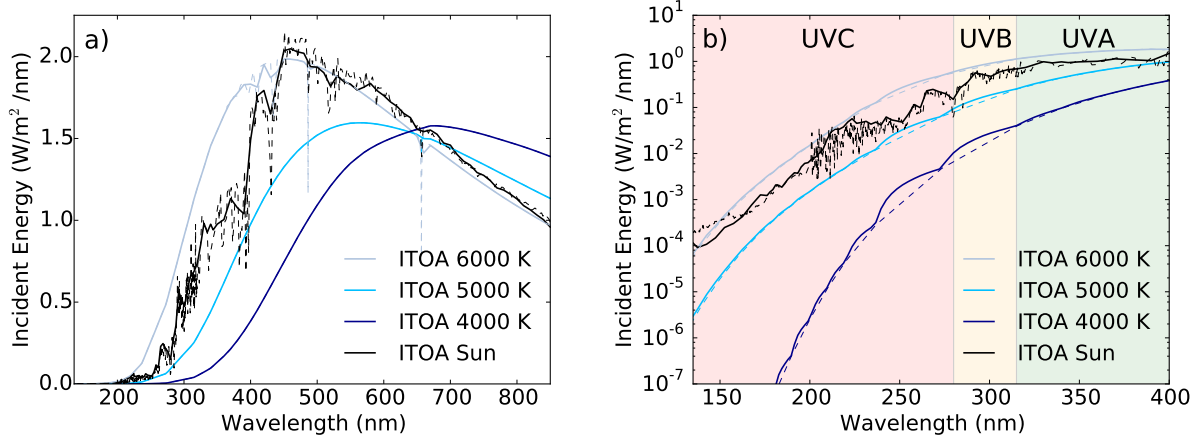


Figure 4.2: Comparisons of the irradiance at the top of the atmosphere (ITOA) for planets orbiting a WD compared to the Earth-Sun system both at high resolution (dashed lines) and binned to the wavelength grid of the climate and photochemistry model resolution (solid lines). All spectra are scaled to the level of present day Earth’s irradiance.

4.2 Methods

4.2.1 Planet model: *EXO-Prime*

We use *EXO-Prime* (see e.g. Kaltenegger et al. 2010); a coupled 1D radiative-convective atmosphere code developed for rocky exoplanets. The code is based on iterations of a 1D climate model (Kasting & Ackerman 1986; Pavlov et al. 2000; Haqq-Misra et al. 2008), a 1D photochemistry model (Pavlov & Kasting 2002; Segura et al. 2005, 2007), which are run to convergence (see details in Segura et al. 2005). *EXO-Prime* models exoplanet

CHAPTER 4. HABITABLE PLANETS ORBITING WHITE DWARFS

atmospheres and environments depending on the stellar and planetary conditions, including the UV radiation that reaches the surface and the planet’s reflection, emission and transmission spectrum. We divide the atmosphere in 100 plane parallel layers for our model up to an altitude of 60 km (or a pressure of 1 mbar) using a stellar zenith angle of 60 degrees.

Visible and near-IR shortwave fluxes are calculated with a two stream approximation including atmospheric gas scattering (Toon et al. 1989), and longwave fluxes in the IR region are calculated with a rapid radiative transfer model (RRTM). A reverse-Euler method within the photochemistry code (originally developed by Kasting et al. 1985) contains 220 reactions to solve for 55 chemical species.

First, we scale the incident WD flux at the top of the model planetary atmospheres to the total integrated flux Earth receives from the Sun (S_{eff}) to model how the WD’s irradiance changes the planetary environment compared to Earth. We then bin the high resolution spectra to the resolution of the wavelength grid of the climate/photochemistry models (both shown in Figure 4.2). We model planets with surface pressures of 0.3 bar (e.g. eroded atmosphere), 1 bar (Earth analogue), and 1.5 bar and 2 bar.

In our planetary models we keep the planetary outgassing rates constant for H_2 , CH_4 , CO , N_2O , and CH_3Cl and maintain the mixing ratios of O_2 at 0.21 and CO_2 at 3.55×10^{-6} to be able to compare the effect of the irradiation on the planetary atmosphere, with a varying N_2 concentration that is used as a fill gas to reach the set surface pressure of the model (following Segura et al. 2003, 2005; Rugheimer et al. 2013, 2015a,b; Rugheimer & Kaltenegger 2018). Note that by keeping the outgassing rates constant, lower surface pressure atmosphere models initially have slightly higher mixing

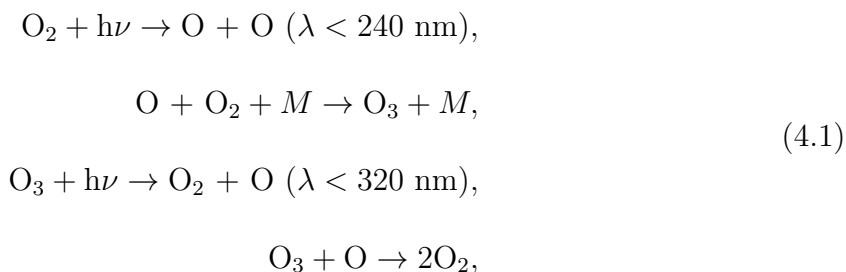
ratios of chemicals with constant outgassing ratios than higher surface pressure models.

4.2.2 White Dwarf Model Spectra

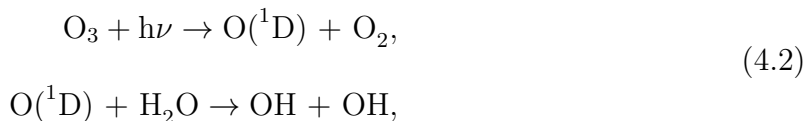
WDs are unique stellar environments with very high surface gravities and extremely dense interiors and physical conditions. They have no internal heat source, and thus cool off over time (Figure 4.1). We use WD spectral energy distribution models (SED) calculated as described in Saumon et al. (2014) (Figure 4.2) as irradiation for the planetary models (see e.g. Bergeron et al. 1997; Kowalski & Saumon 2006; Kilic et al. 2009a,b; Giammichele et al. 2012; Saumon et al. 2014 for detailed discussion on WD spectra). The WD models assume a pure H atmospheric composition with a surface gravity of $\log g = 8.0$ in creating the models for the average mass of WD in the field ($0.6 M_{\odot}$; e.g. Kepler et al. 2016b). The WD radius is then recovered by finding the intersection of the standard surface gravity formula with the WD mass-radius-(temperature) relation for C-O core WDs with thick H layers discussed by Parsons et al. (2017)(see their Figure 9; also see Benvenuto et al. 1999; Fontaine et al. 2001; Parsons et al. 2017 extrapolated to $T < 10,000$ K. The radius of the WD in our model is $0.0128 \pm 0.0001 R_{\odot}$ for surface temperatures of 6000 K to 4000 K. WD spectra are similar to black bodies with only Balmer absorption lines for surface temperatures greater than 5000 K, where hydrogen becomes neutral as shown in Figure 4.2. We use models from Bergeron et al. (2001) for the temperature evolution of the WD (see Figure 4.1).

4.2.3 Photochemistry of some biologically interesting species

Some atmospheric species exhibit noticeable features in our planet’s spectrum as a result directly or indirectly from biological activity. The main ones are oxygen (O_2), ozone (O_3), methane (CH_4), nitrous oxide (N_2O) and methyl chloride (CH_3Cl) (see e.g. Demarais et al. 2012; Kaltenecker 2017). We summarize the most important reactions that influence these species in Earth’s atmosphere here. Many reactions in Earth’s atmosphere are driven by the Sun’s UV flux. Ozone and O_2 are created with UV photons through the Chapman reactions (Chapman 1930),



where M is a background molecule such as N_2 . These reactions are primarily responsible for ozone production on present day Earth. A higher UV flux additionally increases the primary source reactions of tropospheric hydroxyl (OH) for $300 < \lambda < 320 \text{ nm}$ in the troposphere,



reducing O_3 and H_2O . Increased OH is the primary sink for H_2 , CH_4 , CH_3Cl , and CO abundances.

Methane (CH_4) is a reducing gas that has a lifetime of 10-12 years in present day Earth’s atmosphere (Houghton et al. 2004) due to reactions with oxidizing species. It has both natural (termites, wetlands) and anthropogenic sources (rice agriculture, natural

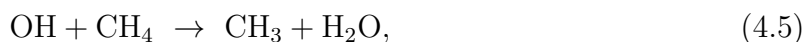
gas). It is oxidized via



creating H_2O and H_2 via photolysis,



Its main sink is due to the reaction,



in the troposphere, and photolysis in the stratosphere. This reaction also creates H_2O in the stratosphere, above where it is shielded by the ozone layer.

On Earth both nitrous oxide (N_2O) and methyl chloride (CH_3Cl) are primarily produced by life, and are depleted by higher amounts of UV. N_2O is a greenhouse gas that is extremely effective when trapping heat. It is produced naturally in soil through nitrification and denitrification, and its anthropogenic source is from agriculture. Photolysis of N_2O occurs for $\lambda < 220$ nm, and is its main sink on present day Earth. Increased O_3 , e.g. due to UV irradiation, is also a sink of N_2O ,

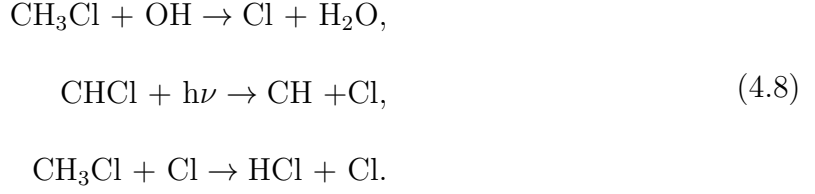


creating NO. It depletes ozone via



On Earth CH_3Cl is naturally produced in oceans via light interacting with sea foam chlorine and biomass and in small amounts by phytoplankton. CH_3Cl reacts with OH creating Cl, a component of chlorofluorocarbons which damage the ozone layer. It is

converted into chlorine via the reactions,



4.3 Results

4.3.1 Time evolution of a white dwarf’s habitable zone

During the cooling process of a WD, its surface temperature as well as its overall luminosity decreases. This, in turn, influences the orbital distance of its HZ. The HZ is the circular region around one or multiple stars in which standing bodies of liquid water could exist on a rocky planet’s surface (e.g. Kasting et al. 1993; Kaltenegger et al. 2013; Haghhighipour & Kaltenegger 2013; Kopparapu et al. 2013, 2014; Ramirez & Kaltenegger 2017) and facilitate the detection of possible atmospheric biosignatures (see e.g. Kaltenegger 2017). The classical, conservative N₂-CO₂-H₂O HZ is defined by the greenhouse effect of two gases: CO₂ and H₂O vapor. The inner edge corresponds to the distance where mean surface temperatures exceed the critical point of water (~647 K, 220 bar), triggering a runaway greenhouse that leads to rapid water loss to space on very short timescales (see Kasting et al. 1993 for details). Toward the outer edge of the classical HZ weathering rates decrease, allowing atmospheric CO₂ concentrations to increase as stellar insolation decreases. At the outer edge, condensation and scattering by CO₂ outstrips its greenhouse capacity, the so-called maximum greenhouse limit of CO₂.

The cooling of a WD translates into an inward shift of the orbital distances of the WD HZ, (Figure 4.3a). In addition to the decrease in overall irradiance (S_{eff}) as the WD cools, some of the change in the HZ orbital distance is also caused by the shift of the peak wavelength of emission of the WD SED to redder wavelengths, which heat the surface of the planet more efficiently than bluer light (e.g. Kasting et al. 1993). A $0.6 M_{\odot}$ WD spends about 7 Gyr cooling from 6000 K to 4000 K, providing a phase during which its luminosity does not rapidly change and thus it could provide temperate conditions for an orbiting planet. The size of the WD HZ is shown in Figure 4.3a as well as the corresponding irradiance of a planet, normalized to the value for Earth (S_{eff}) shown in Figure 4.3b. Because of the small size of a WD compared to the Sun, the WD HZ is a factor of ~ 100 to ~ 1000 times closer to the WD than Earth is to the Sun.

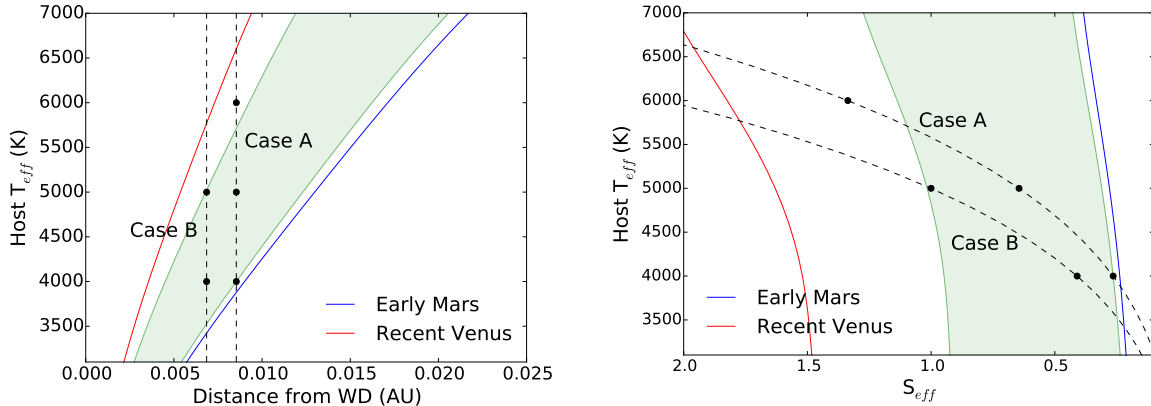


Figure 4.3: Size of a WD’s HZ (left) as well as the corresponding range of WD irradiance, normalized to the value for Earth (S_{eff}) (right). The shaded green region represents the classical HZ for our WD model (following Kopparapu et al. 2014). The red (recent Venus) and blue (early Mars) lines show the limits of the empirical HZ (following Ramirez & Kaltenegger 2017). Two case studies for a planet in the WD’s HZ, Case A and B, are indicated in both panels. The black dots indicate the specific WD surface temperatures and planetary distances/ S_{eff} values we model in this study.

An alternative HZ limit that is not based on atmospheric models (like the classical HZ) but on empirical observations of our Solar System is also shown in Figure 4.3 for

comparison. The inner edge of the empirical HZ is defined by the stellar flux received by Venus when we can exclude the possibility that it had standing water on the surface (about 1 Gyr ago), equivalent to a stellar flux of $S_{eff} = 1.77$, corresponding to a distance of 0.75 AU for Earth’s current Solar flux (Kasting et al. 1993). The “early Mars” limit is based on observations suggesting that the Martian surface may have supported standing bodies of water ~ 3.8 Gyr ago, when the Sun was only 75% as bright as today. For our solar system, $S_{eff} = 0.32$ for this limit, corresponding to a distance of ~ 1.77 AU (e.g. Kasting et al. 1993).

We first explore the range of conditions for Earth-like planets orbiting WDs of different temperatures seen at one point in time (see Sections 3.2 and 3.3). Then we model two case studies, A and B, as shown in Figure 4.3, which explore the environment of a planet in the HZ of a WD as it cools (see Section 3.4).

4.3.2 Planetary photochemistry environments for different stages in a WD’s evolution

The lack of chromospheric activity for a WD at different stages in its evolution causes photochemical differences in the atmospheres of planets orbiting it compared to Earth. We modeled planets with different surface pressures, which receive an equivalent total irradiance as Earth from the Sun (S_{eff}) from a WD at three different stages in its evolution: for WD surface temperatures of 6000 K, 5000 K and 4000 K. We model planets with surface pressures ranging from 2 bar to 0.3 bar. Table 5.1 summarizes the model planet surface temperature and integrated overall ozone column depth (ozone column depth) for the different planetary models as well as our Earth model for comparison.

Table 4.1:: Model summary for Earth-equivalent irradiance

| Host T_{eff} (K) | Pressure (bar) | Surface T_{eff} (K) | Ozone Column Depth (cm^{-2}) |
|------------------------------|-------------------|---------------------------------|--|
| Present day Earth | 1.0 | 288.2 | 5.4×10^{18} |
| 6000 | 0.3 | 280.7 | 3.6×10^{18} |
| 6000 | 1.0 | 285.6 | 5.7×10^{18} |
| 6000 | 1.5 | 288.0 | 6.5×10^{18} |
| 6000 | 2.0 | 289.0 | 6.9×10^{18} |
| 5000 | 0.3 | 282.4 | 2.6×10^{18} |
| 5000 | 1.0 | 290.8 | 3.9×10^{18} |
| 5000 | 1.5 | 295.0 | 4.2×10^{18} |
| 5000 | 2.0 | 298.1 | 4.5×10^{18} |
| 4000 | 0.3 | 282.8 | 1.1×10^{18} |
| 4000 | 1.0 | 294.3 | 1.8×10^{18} |
| 4000 | 1.5 | 300.4 | 2.1×10^{18} |
| 4000 | 2.0 | 305.1 | 2.3×10^{18} |

Figure 4.4 shows the changes in temperature as well as the mixing ratio for O_3 , CH_4 , H_2O , CH_3Cl and N_2O for the different models, compared to Earth.

Figure 4.4 shows that in the model atmospheres H_2O photolysis increases with higher UV levels in the upper atmosphere, where H_2O is not shielded from incoming photons below the ozone layer. N_2O is depleted by photolysis, with a decreasing mixing ratio toward the top of the atmosphere, but remains well mixed beneath the ozone layer, where it is shielded. All higher surface pressure models show increased amounts of CH_4 , N_2O , and CH_3Cl in the upper atmosphere. Atmospheric H_2O increases with higher surface temperatures.

The WD cooling process provides a changing luminosity as well as UV environment at a set orbital distance, as seen in Figure 4.1. The decrease in UV incident flux leads to an overall decrease in the ozone level. Compared to present day Earth's integrated overall ozone column depth, a higher surface pressure atmosphere receiving similar UV

irradiance has a higher ozone column depth, as seen in the values for our planet models with surface pressures above 1 bar orbiting a WD with a surface temperature of 6000 K.

Table 5.1 shows the absolute values for our models as well as present day Earth's.

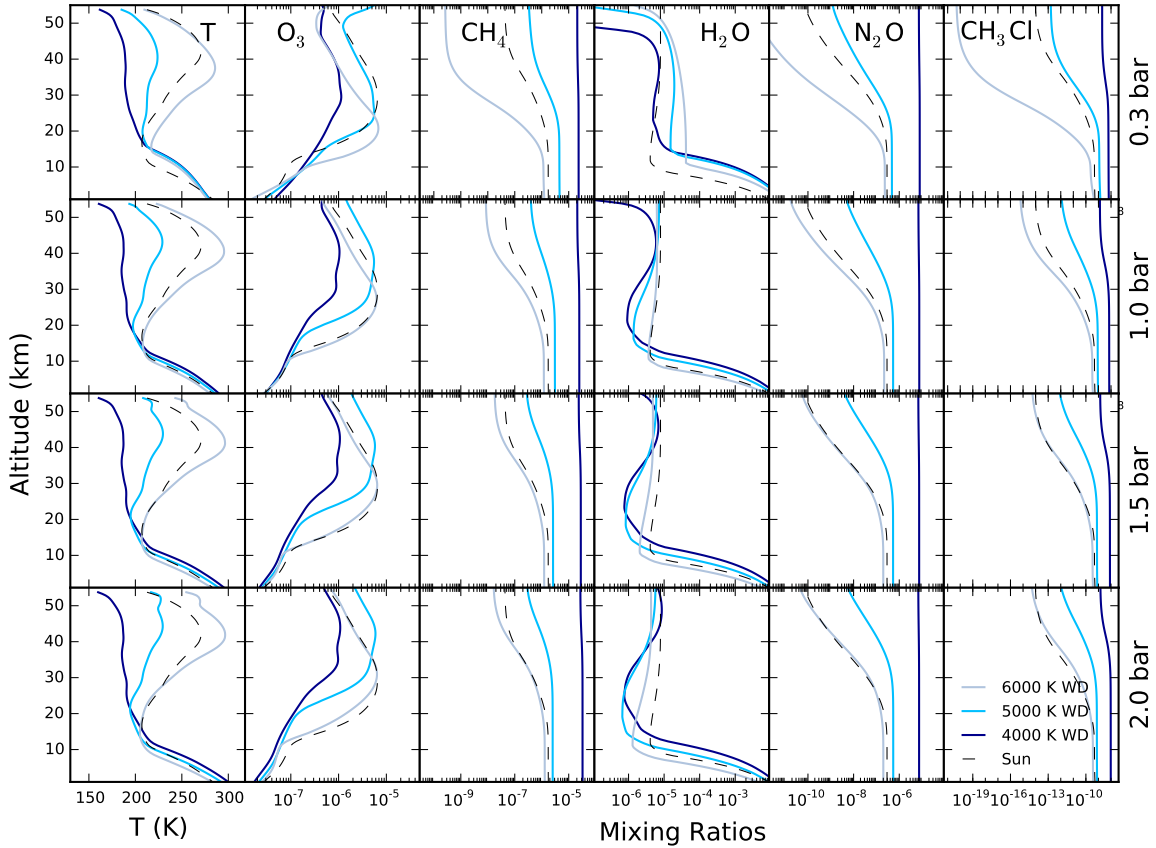


Figure 4.4: Temperature and chemical mixing ratios for some biological interesting species for model planets orbiting a WD (blue solid lines) with 3 different surface temperatures (6000 K, 5000 K and 4000 K). Earth's values are shown for comparison (black dashed line).

WD photochemistry: Earth-analogue: 1 bar surface pressure models

Planet models with a 1 bar surface pressure, analogous to Earth, orbiting WDs show surface temperatures 285.6 K, 290.8 K, 294.3 K for WD surface temperatures of 6000 K,

5000 K and 4000 K respectively.

However, the different WD UV environments compared to the Sun's lead to a 5% increase in ozone column depth for the 6000 K WD surface temperature, and a 28% and 67% decrease of ozone column depth for the 5000 K and 4000 K WDs compared to Earth.

Higher ozone levels cause a higher rate of the R4.2 reaction, producing OH. Increased amounts of OH for higher UV levels depletes CH₄ via the R4.5 reaction, and similarly CH₃Cl via the R4.8 reaction (see Figure 4.4).

WD photochemistry eroded atmospheres: 0.3 bar surface pressure models

Planet models with a 0.3 bar surface pressure, analogous to eroded atmospheres, orbiting WDs show lower surface temperatures than 1.0 bar models, increasing with decreasing WD surface temperature from 280.7 K to 282.8 K, respectively. The different UV WD environments, the decreased overall amount of oxygen, as well as the decreased density of the atmosphere lead to a 33%, 52%, and 80% decrease in ozone column depth compared to Earth. Longer mean-free-paths due to lower atmospheric density result in photolysis occurring at lower altitudes, causing ozone to form closer to the ground (see Figure 4.4).

WD photochemistry: Higher surface pressure planets: 1.5 & 2.0 bar surface pressure models

The 1.5 bar surface pressure models, for higher surface pressure planets, orbiting WDs show surface temperatures of 288.0 K, 295.0 K, 300.4 K for WD surface temperatures of 6000 K, 5000 K and 4000 K respectively. The different UV environments compared to

the Sun and the increase in overall oxygen content as well as density of the atmosphere lead to a 20% increase in ozone column depth for the 6000 K WD surface temperature, and a 22% and 61% decrease in ozone column depth compared to Earth for the 5000 K and 4000 K WDs, respectively.

Planet models with a 2 bar surface pressure show surface temperatures of 289.0 K, 298.1 K, 305.1 K for WD surface temperatures of 6000 K, 5000 K and 4000 K respectively. The different UV environments compared to the Sun and the increase in overall oxygen content as well as density of the atmosphere lead to a 28% increase in ozone column depth for the 6000 K WD surface temperature, and a 17%, and 57% decrease in ozone column depth compared to Earth, less than for the 1.5 bar surface pressure case.

4.3.3 UV surface environment around an evolving WD

The WD cooling process provides a changing luminosity as well as UV environment at a set orbital distance, as seen in Figure 4.2. The UV surface environment for our planetary models from eroded atmospheres to dense atmospheres with increased surface pressure is shown in Figure 4.5, with integrated fluxes for UVA (315-400 nm), UVB (280-315 nm), and UVC (121.6-280 nm) are shown in Table 4.2, with comparisons to the Earth-Sun system's integrated fluxes in Table 4.3. Note that this model does not take scattering or clouds into account and thus overestimates the amount of UV that reaches the surface. However the comparison between the values and models for the UV environment on present-day Earth gives a clearer picture of the level of UV radiation that reaches the ground, compared to our own planet. High energetic UV is capable of causing harm to biological molecules, like DNA (e.g. Voet et al. 1963; Diffey 1991; Matsunaga et al.

Table 4.2:: UV Integrated Fluxes

| Host T _{eff} (K) | Pressure (bar) | UVA 315 - 400 nm (W/m ²) | | | UVB 280 - 315 nm (W/m ²) | | | UVC 121.6 - 280 nm (W/m ²) | | |
|------------------------------|-------------------|--------------------------------------|--------|-------------|--------------------------------------|--------|-------------|--|---------|-------------|
| | | ITOA | Ground | % to ground | ITOA | Ground | % to ground | ITOA | Ground | % to ground |
| Earth* | 1.0 | 72.4 | 50.6 | 70 | 18.9 | 2.2 | 11 | 7.1 | 3.9E-19 | 5.4E-18 |
| 6000 | 0.3 | 113.2 | 105.1 | 93 | 32.4 | 7.4 | 23 | 18.5 | 1.9E-10 | 1.0E-9 |
| 6000 | 1.0 | 113.2 | 78.9 | 70 | 32.4 | 3.5 | 11 | 18.5 | 1.9E-19 | 1.0E-18 |
| 6000 | 1.5 | 113.2 | 67.8 | 60 | 32.4 | 2.5 | 7.6 | 18.5 | 3.3E-22 | 1.8E-21 |
| 6000 | 2.0 | 113.2 | 59.9 | 53 | 32.4 | 2.0 | 6.1 | 18.5 | 1.8E-23 | 9.6E-23 |
| 5000 | 0.3 | 39.4 | 37.6 | 95 | 6.6 | 2.0 | 31 | 2.3 | 6.6E-10 | 2.9E-8 |
| 5000 | 1.0 | 39.4 | 28.6 | 73 | 6.6 | 1.0 | 16 | 2.3 | 2.5E-14 | 1.1E-12 |
| 5000 | 1.5 | 39.4 | 24.6 | 62 | 6.6 | 0.80 | 12 | 2.3 | 1.4E-15 | 6.2E-14 |
| 5000 | 2.0 | 39.4 | 21.7 | 55 | 6.6 | 0.63 | 9.5 | 2.3 | 9.9E-17 | 4.3E-15 |
| 4000 | 0.3 | 10.4 | 10.2 | 98 | 0.98 | 0.47 | 48 | 0.17 | 7.1E-6 | 4E-3 |
| 4000 | 1.0 | 10.4 | 7.9 | 76 | 0.98 | 0.25 | 26 | 0.17 | 2.1E-8 | 1.2E-5 |
| 4000 | 1.5 | 10.4 | 6.8 | 65 | 0.98 | 0.19 | 19 | 0.17 | 1.6E-9 | 9.9E-7 |
| 4000 | 2.0 | 10.4 | 6.0 | 58 | 0.98 | 0.15 | 15 | 0.17 | 2.4E-10 | 1.4E-7 |

*Earth values reflect present day values

1991; Tevini 1993; Cockell 1998; Kerwin & Remmele 2007). Present day Earth surface life is protected by the ozone layer, which shields the surface from the most biologically dangerous radiation (UVC).

Surface UV environments: Earth 1 bar surface pressure models

For comparison we first model the amount of radiation that reaches the Earth’s surface (see also Rugheimer et al. 2015a). For our present-day Earth model the integrated UVA ground flux compared to the UVA ITOA flux is 70%. For integrated UVB flux, which is partially shielded by ozone, 11% of the ITOA UVB flux reaches the surface. The UVC flux is almost completely shielded by an ozone layer, and only $5.4 \times 10^{-18}\%$ of the ITOA integrated UVC flux reaches the surface (see Table 4.5).

WD surface UV environments: Earth-analogue: 1 bar surface pressure models

For our 1 bar surface pressure planet models, the amount of UVA flux at the surface compared to the ITOA integrated flux increases from 70% to 76% for the 6000 K to

Table 4.3:: UV Integrated fluxes compared to Earth

| Host T _{eff} (K) | Pressure (bar) | WD UV/ Present day Earth UV | | |
|------------------------------|-------------------|-----------------------------|------------------|----------------------|
| | | UVA (315-400 nm) | UVB (280-315 nm) | UVC (121.6-280 nm) |
| 6000 | 0.3 | 2.1 | 3.3 | 4.9×10^8 |
| 6000 | 1.0 | 1.6 | 1.6 | 4.9×10^{-1} |
| 6000 | 1.5 | 1.3 | 1.1 | 8.6×10^{-4} |
| 6000 | 2.0 | 1.2 | 0.90 | 4.7×10^{-5} |
| 5000 | 0.3 | 0.74 | 0.90 | 1.7×10^9 |
| 5000 | 1.0 | 0.57 | 0.45 | 6.5×10^4 |
| 5000 | 1.5 | 0.49 | 0.36 | 3.6×10^3 |
| 5000 | 2.0 | 0.43 | 0.28 | 2.6×10^2 |
| 4000 | 0.3 | 0.20 | 0.21 | 1.8×10^{13} |
| 4000 | 1.0 | 0.16 | 0.11 | 5.3×10^{10} |
| 4000 | 1.5 | 0.13 | 0.085 | 4.2×10^9 |
| 4000 | 2.0 | 0.12 | 0.067 | 6.2×10^8 |

4000 K WD surface temperature cases respectively, compared to the 70% for present day Earth models. For UVB, it increases from 11%, to 26% of the ITOA integrated UVB for the 6000 K to 4000 K WD surface temperature cases respectively, compared to 11% for Earth models. The UVC flux is almost completely shielded by an ozone layer, and is only $1.0 \times 10^{-18}\%$ to $1.2 \times 10^{-5}\%$ of the ITOA integrated UVC flux, for the 6000 K to 4000 K WD surface temperature cases respectively, compared to $5.4 \times 10^{-18}\%$ on present day Earth.

WD surface UV environments: Eroded atmospheres: 0.3 bar surface pressure models

For our 0.3 bar surface pressure planet models, the amount of integrated UVA surface flux compared to the ITOA integrated flux increases from 93% to 98% for the 6000 K to 4000 K WD surface temperature cases, compared to 70% for present day Earth models. For integrated UVB flux there is an increase from 23% to 48% of the ITOA UVB for

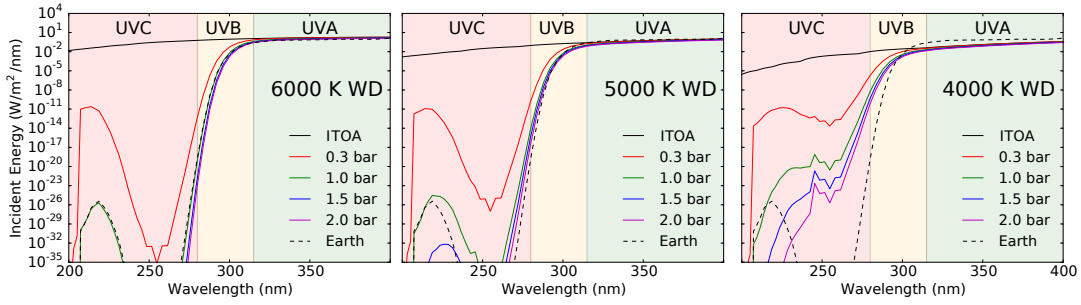


Figure 4.5: Surface UV environment for planetary models with higher surface pressure (2 bar) to small planets or planets with eroded atmospheres (0.3 bar) orbiting WDs (solid lines) compared to present day Earth (dashed lines), and the incident (top-of-atmosphere) irradiation for the WD (black solid line).

the 6000 K to the 4000 K WD surface temperature cases, higher than the 11% for present day Earth. The total integrated UVC surface flux increases from $1.0 \times 10^{-9}\%$ to $4.3 \times 10^{-3}\%$ of the ITOA flux for the 6000 K to the 4000 K WD surface temperature cases, orders of magnitude higher than the $5.4 \times 10^{-18}\%$ for Earth.

WD surface UV environments: higher surface pressure planets: 1.5 bar and 2 bar surface pressure models

For our 1.5 bar surface pressure planet models, the amount of integrated surface UVA flux compared to the ITOA integrated flux increases from 60% to 65% for the 6000 K through 4000 K WD surface temperature cases, less than the 70% for present day Earth models. For UVB surface flux there was an increase of 7.6% to 19% of the ITOA integrated UVB flux for the 6000 K to 4000 K WD surface temperature cases, comparable to 11% for Earth models. The UVC ground flux increased from $1.8 \times 10^{-21}\%$ to $9.9 \times 10^{-7}\%$ of the ITOA integrated flux for the 6000 K to the 4000 K WD surface temperature cases, respectively, compared to $5.4 \times 10^{-18}\%$ for present day Earth.

CHAPTER 4. HABITABLE PLANETS ORBITING WHITE DWARFS

For our 2 bar surface pressure planet models, the amount of integrated UVA ground flux compared to the ITOA integrated flux increases from 53% to 58% for the 6000 K to 4000 K WD surface temperature cases, respectively, less than 70% for present day Earth models. For UVB integrated ground flux there is an increase of 6.1% to 15% of ITOA UVB integrated flux reaching the surface for the 6000 K through 4000 K WD surface temperature cases respectively, comparable to 11% for present day Earth. The integrated UVC flux to the ground increases from $9.6 \times 10^{-23}\%$ to $1.4 \times 10^{-7}\%$ of the original integrated ITOA flux for the 6000 K to 4000 K WD surface temperature cases, respectively, compared to $5.4 \times 10^{-18}\%$ for Earth models.

The planetary models with the 4000 K WD surface temperature host show the highest overall UVC ground flux despite having a lower UVC ITOA integrated flux, because of the lower ozone level in these atmospheres, compared to hotter WD models.

Overall, Figure 4.5 shows that the UV surface environment for our model planets orbiting WDs. The 1 bar surface pressure model for a 6000 K WD surface temperature model receives similar UV surface levels as present day Earth models. Only the 1.5 bar and 2 bar surface pressure models for the same 6000 K WD surface temperature receive a lower UV integrated surface flux than present day Earth. For all other models, the UV surface flux is higher than for present day Earth, especially the UVC environment (see Table 4.3).

Table 4.4:: Case A & Case B Results

| Host (K) | Case A: r = 0.0085 AU | | | Case B: r = 0.0069 AU | | |
|-------------|-----------------------|--------------------------|--|-----------------------|--------------------------|--|
| | S_{eff} | Surface T_{eff} (K) | Ozone Column Depth (cm^{-2}) | S_{eff} | Surface T_{eff} (K) | Ozone Column Depth (cm^{-2}) |
| 6000 | 1.3 | 328.4 | 1.7×10^{18} | 2.1 | RG* | RG* |
| 5000 | 0.64 | 249.6 | 4.4×10^{18} | 1.0 | 290.8 | 3.3×10^{18} |
| 4000 | 0.26 | 191.9 | 9.6×10^{17} | 0.41 | 216.9 | 1.3×10^{18} |

*RG indicates a runaway greenhouse state

4.3.4 Planetary environments for planets in the HZ through the evolution of a WD

We model two case studies, A and B, as shown in Figure 4.3, which explore the environment of a planet with a 1 bar surface pressure (i.e., an Earth analogue) in the HZ of a WD during its evolution. Case A shows the maximum time a planet can stay in the HZ of the WD as the WD cools from 6000 K to 4000 K. This amounts to ~ 6 Gyr for the classical (conservative) HZ and ~ 8.5 Gyr for the empirical HZ. Case B focuses on a planet that initially receives the same irradiance as Earth around a WD with a surface temperature of 5000 K. As the WD cools from 6000 K to 4000 K the planet spends ~ 4 Gyr in the conservative HZ and ~ 7 Gyr in the empirical HZ. Model parameters and results are shown in Tables 4.4 and 4.5, with comparisons to Earth in Table 4.6 for both cases. UV environments are shown in Figure 4.7 for Case A and Figure 4.6 for Case B, and photochemistry is shown in Figure 4.8.

Such a planet could have orbited in the HZ of a cool WD for longer than the Earth has existed. Single-celled life likely emerged on Earth less than 1 Gyr after its formation, with multicellular life following 2.7 Gyr later.

Case A

The orbital distance of 0.0085 AU or 1.3 million km leads to a changing illumination by the cooling WD from S_{eff} of 1.34 for a 6000 K WD surface temperature, to S_{eff} of 0.64 for a 5000 K WD surface temperature, to S_{eff} of 0.26 for the 4000 K WD surface temperature model. This leads to decreasing planetary surfaces temperatures of 328.4 K, 249.6 K, 191.9 K for WD surface temperatures of 6000 K, 5000 K and 4000 K, respectively.

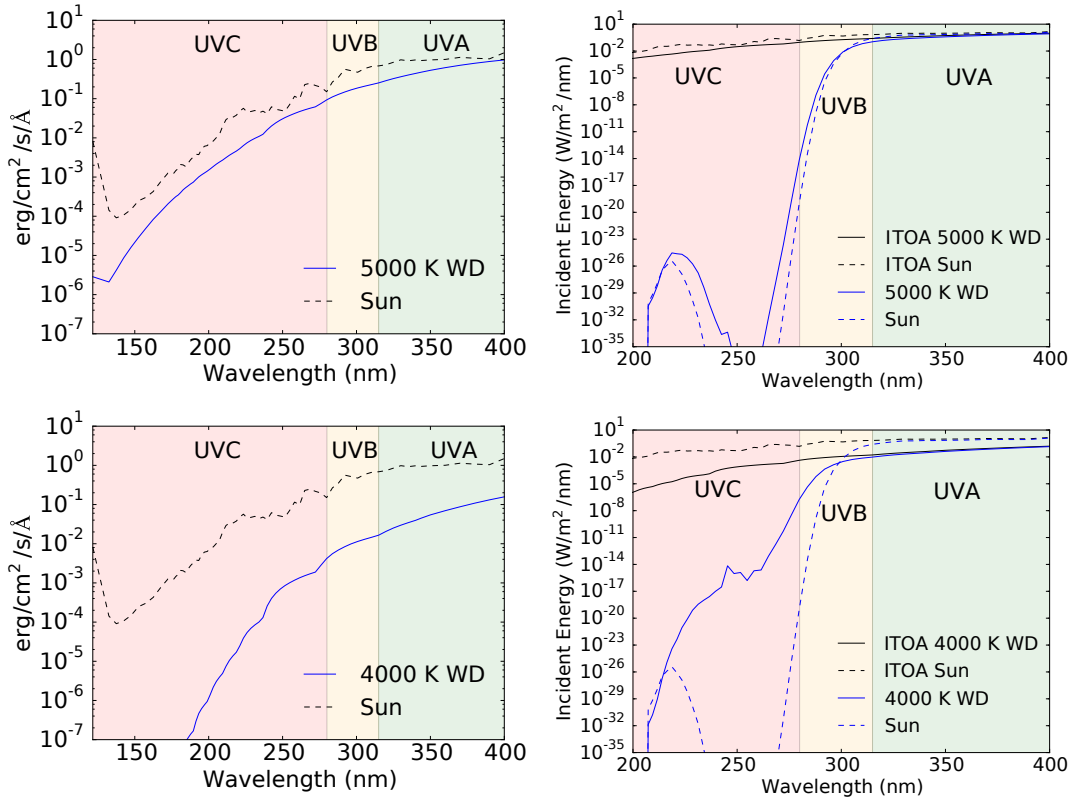


Figure 4.6: UV surface flux for Case B: a planet orbiting at 0.0069 AU, corresponding to $S_{eff} = 1.0$ for the 5000 K WD surface temperature, and $S_{eff} = 0.41$ for the 4000 K WD surface temperature model. At 6000 K the S_{eff} equals 2.07, placing the planet outside of both the conservative as well as empirical HZ.

In our model the planet's surface temperature is on average above freezing for only

a part of the time the planet spends in the WD's HZ, a few billion years (Figure 4.1 and Figure 4.3). However we have not adjusted the CO₂ content in our models, thus if a cycle similar to the carbonate silicate cycle on Earth existed on such a planet, CO₂ concentration should increase, heating the planet's surface temperature and keeping it from freezing. As shortly discussed, a geologically active planet is the underlying assumption of continued habitability during a star's evolution, and is what led to the concept of the HZ (see e.g. Kasting et al. 1993). For a WD, a similar cycle could be possible, extending the time the surface of such a planet can be above freezing to the full range of its time in the WD's HZ.

The different WD UV environments compared to the Sun lead to a 29%, 18%, and 82% decrease in overall ozone column depth compared to Earth. As shown in Figure 4.8, ozone levels are highest for a WD model of 5000 K, providing a slightly higher shielding from UV than present day Earth. However, during both the 6000 K and 4000 K WD surface temperature stages, the UVC flux at the surface increases substantially for different reasons. During the 6000 K WD surface temperature period, UV photons with $\lambda < 320$ [R4.1] are available. These can dissociate ozone, therefore increasing the UV surface flux. The 4000 K WD model has a comparably high amount of surface UVC radiation because low UV irradiation from the 4000 K WD cannot initially produce enough ozone to efficiently shield the surface of the planet.

The amount of UVA integrated surface flux compared to the ITOA integrated flux is 71%, 74%, and 78%, for the 6000 K, 5000 K, and 4000 K WD surface temperature cases, comparable to the 70% for model Earth models. For UVB flux, which is partially shielded by ozone, 24%, 15%, and 32% of the integrated ITOA UVB reach the surface, for the 6000 K, 5000 K, and 4000 K WD surface temperature cases, compared to 11%

CHAPTER 4. HABITABLE PLANETS ORBITING WHITE DWARFS

for present day Earth models. The UVC flux is almost completely shielded by an ozone layer, and the percentage of the integrated ITOA flux reaching the planetary surface $1.0 \times 10^{-5}\%$, $2.4 \times 10^{-14}\%$, and $1.0 \times 10^{-3}\%$, for the 6000 K, 5000 K, and 4000 K WD surface temperature cases, respectively, compared to $5.4 \times 10^{-18}\%$ for present day Earth models.

Table 4.5.: UV Integrated fluxes evolution

| Case | Host T _{eff} (K) | UVA 315 - 400 nm (W/m ²) | | | UVB 280 - 315 nm (W/m ²) | | | UVC 121.6 - 280 nm (W/m ²) | | |
|--------|------------------------------|--------------------------------------|--------|-------------|--------------------------------------|----------------------|-------------|--|-----------------------|-----------------------|
| | | ITOA | Ground | % to ground | ITOA | Ground | % to ground | ITOA | Ground | % to ground |
| Earth* | 5750 | 72.4 | 50.6 | 70 | 18.9 | 2.2 | 11 | 7.1 | 3.9×10^{-19} | 5.4×10^{-18} |
| A | 6000 | 151.3 | 107.0 | 71 | 43.4 | 10.2 | 24 | 24.7 | 2.51×10^{-6} | 1.0×10^{-5} |
| A | 5000 | 25.4 | 18.9 | 74 | 4.3 | 0.64 | 15 | 1.5 | 3.6×10^{-16} | 2.4×10^{-14} |
| A | 4000 | 4.3 | 3.3 | 78 | 0.40 | 0.13 | 32 | 6.8×10^{-2} | 7.0×10^{-7} | 1.0×10^{-3} |
| B | 5000 | 39.4 | 28.6 | 73 | 6.6 | 1.0 | 16 | 2.3 | 2.5×10^{-14} | 1.1×10^{-12} |
| B | 4000 | 2.8 | 2.1 | 77 | 0.26 | 9.2×10^{-2} | 36 | 4.4×10^{-2} | 5.0×10^{-6} | 1.1×10^{-2} |

*Earth values reflect present day values

Case B

The orbital distance of the planet is 0.0069 AU in Case B. This corresponds to an illumination of $1.0 S_{eff}$ for the 5000 K WD, which evolves to $0.41 S_{eff}$ as the WD cools to 4000 K. For Case B planet models the surfaces temperatures are 290.8 K and 216.9 K for WD surface temperatures of 5000 K and 4000 K, respectively. The different UV environments compared to the Sun lead to a 39% and a 77% decrease in overall ozone column depth for WD surface temperatures of 5000 K and 4000 K, respectively, compared to Earth.

The amount of UVA ground flux compared to the ITOA integrated flux is 73% and 77%, for the 5000 K and 4000 K WD surface temperature models, respectively (see Figure 4.6), comparable for the 70% for present day Earth models. For UVB flux, which is partially shielded ozone, only 16%, and 36% of the integrated ITOA UVB reaches

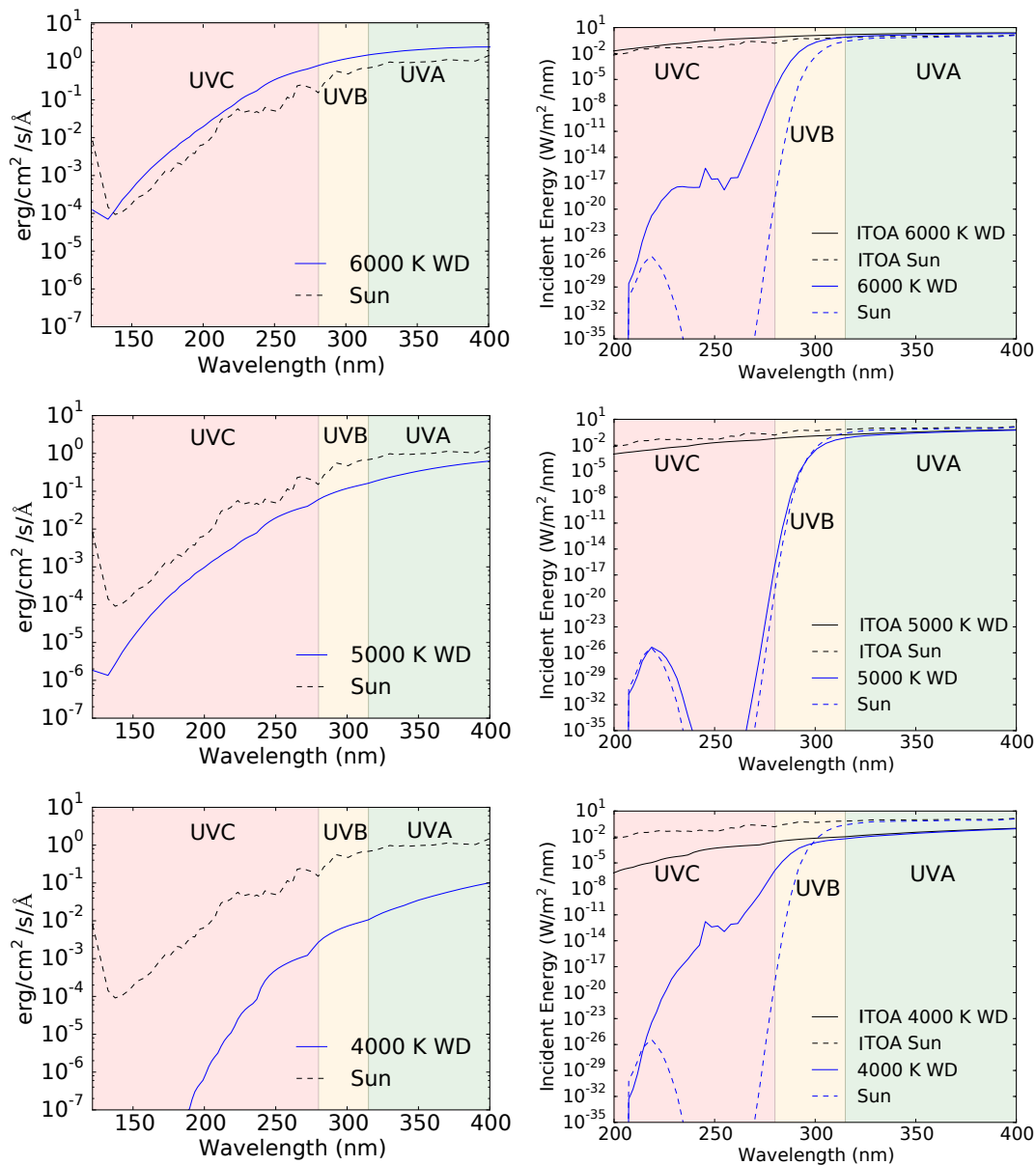


Figure 4.7: UV surface flux for Case A with a planet orbiting at 0.0085 AU from its host, corresponding to $S_{eff} = 1.34$ for the 6000 K model, $S_{eff} = 0.64$ for a 5000 K model, and $S_{eff} = 0.26$ for 4000 K models.

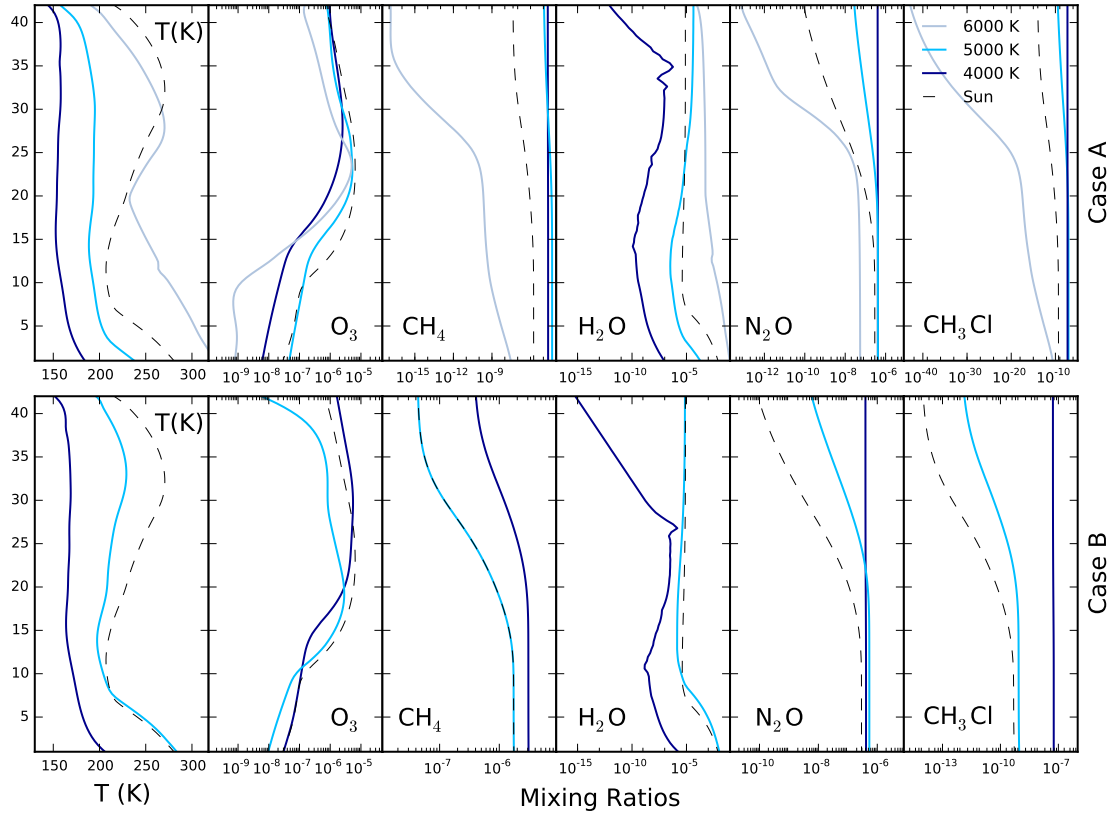


Figure 4.8: Temperature and photochemistry profiles for Case A and B (solid lines), with the Earth-Sun profile for comparison (dashed).

the surface, for the 5000 K and 4000 K WD surface temperature cases, compared to 11% for present day Earth models. The UVC flux is almost completely shielded by an ozone layer, and is $1.1 \times 10^{-12}\%$, and then $1.1 \times 10^{-2}\%$ of the ITOA integrated UVC flux, compared to $5.4 \times 10^{-18}\%$ for present day Earth models.

As the UV levels from the WD decrease, less ozone is produced in the planet's atmosphere and thus UVB and UVC surface levels increase. Average surface temperature decreases below freezing for outgassing rates similar to present day Earth. However, as discussed for Case A, if a carbonate-silicate cycle exists, increased amounts greenhouse gases should increase surface temperatures above freezing for an Earth-like planet even

Table 4.6:: UV Integrated fluxes evolution Earth comparison

| Case | Host T_{eff} (K) | WD UV/Present day Earth UV | | |
|------|------------------------------|----------------------------|----------------------|----------------------|
| | | UVA | UVB | UVC |
| A | 6000 | 2.1 | 4.6 | 6.5×10^{12} |
| A | 5000 | 3.7×10^{-1} | 2.9×10^{-1} | 9.3×10^2 |
| A | 4000 | 6.6×10^{-2} | 5.8×10^{-2} | 1.8×10^{12} |
| B | 5000 | 5.7×10^{-1} | 4.5×10^{-1} | 6.48×10^4 |
| B | 4000 | 4.2×10^{-2} | 4.1×10^{-2} | 1.3×10^{13} |

with decreasing illumination by the cooling WD.

4.4 Discussion

4.4.1 How could white dwarf planets form?

The mechanisms required for a WD planetary system to form as secondary generation objects from a disk or to survive post-main sequence evolution are not well understood. During the post main sequence evolution of the host into a WD, inner rocky planets (within 1-2 AU) would likely be destroyed (e.g. Villaver 2011; Kunitomo et al. 2011; Villaver 2012; Mustill & Villaver 2012; Villaver 2014), while stellar mass loss would cause semimajor axis expansion for outer planets (e.g. Veras 2016; Ramirez & Kaltenegger 2016). Exomoons of outer planets could potentially migrate inward (Veras 2016; Ramirez & Kaltenegger 2016), although the estimated occurrence rate wouldn't explain the rate of polluted WDs (van Sluijs & Van Eylen 2018a; Van Eylen et al. 2018). Second-generation planets could even form from fall-back of debris initially expelled during the post-main sequence evolution of the host star (Veras 2016). An interesting system is WD1145+017, a WD orbited by a rocky minor planet undergoing tidal disintegration at the system's

Roche limit (Vanderburg et al. 2015).

4.4.2 Only dry planets? White dwarfs start with an extremely hot phase

With no stellar mass loss during the WD phase (and assuming rapid tidal circularization of its orbit), a planet should remain at the same orbital distance during a WD's evolution. Due to the extreme change in luminosity early in a WD's evolution (Figure 4.1) a temperate planet around a cool WD would have thus experienced an extremely high luminosity and corresponding surface temperature early in its history. This would initiate a runaway greenhouse process and extreme water loss on such planets early in their history. Similarly for planets orbiting pre-main sequence M-type stars, which also are more luminous initially and should be able to initiate a runaway greenhouse phase and water loss on a temperate planet that can be found in the main sequence HZ later on (see Ramirez & Kaltenegger 2014; Barnes et al. 2015), there may be methods of late water delivery occurring in a WD system after to the WD has cooled to a surface temperature that maintains a slower changing luminosity (e.g. Jura & Xu 2010; Farihi et al. 2013; Malamud & Perets 2016, 2017a,b).

Any Earth-like planet that is orbiting too close to the WD would remain in a runaway greenhouse stage for a certain time, until it entered the WD HZ. Whether or not such planets would have lost all their water at that point would depend strongly on the initial water reservoir, and whether it can be replenished. Thus, whether a WD planet can host water and an Earth-like atmosphere, is an open question and will depend on its evolution as well as when the WD planet is formed, from what materials it is made

of and whether the possibility of a continuous water delivery exists in WD planetary systems.

4.4.3 A white dwarf planet's evolution differs from that of Earth

A planet orbiting a WD will receive decreasing overall energy from its host during the WD's cooling process. Its evolution is very different from that of a planet orbiting a main sequence star, whose luminosity increases with time, pushing the HZ to wider separations. For a planet around a main sequence star, the increase in greenhouse gases at the inner edge of the HZ coupled with the increasing luminosity of the host star limit the time it can remain habitable. If a cycle similar to the carbonate silicate cycle could also operate on WD planets, planets on the inner edge of a WD could build up substantial greenhouse gas amounts in their atmospheres as well; however due to the decreasing luminosity of their WD host, such build up of greenhouse gases could help to maintain warm surface temperature as the WD flux decreases, possibly extending the length of time life could survive on WD planets.

4.5 Conclusions

Our models explore the atmospheric environments of planets orbiting WDs, taking into consideration the changing surface temperatures and UV environments of WDs during their cooling process.

We model the atmospheric composition as well as the UV surface environments of

CHAPTER 4. HABITABLE PLANETS ORBITING WHITE DWARFS

Earth-like planets orbiting WDs during different points throughout a WD's evolution. Our planet models have surface pressures ranging from 2 bar to 0.3 bar, including Earth-analog planets with 1 bar atmospheres, as well as planets with 0.3 bar surface pressure (e.g. eroded atmospheres) and planets with higher surface pressures of 1.5 bar and 2 bar (e.g, super-Earths).

The integrated overall ozone column depth is less than on present day Earth for all our model runs, except for the models with surfaces pressures of 1 bar or above for the WD 6000 K surface temperature model, which provides similar UV to the Sun. The UV surface environment on a planet is controlled primarily by the incoming irradiation and by the planetary atmospheric composition. The UV surface environment for all our planetary models orbiting WDs show increased surface UVC flux up to several orders of magnitude compared to present day Earth, except for the models with surface pressures of 1 bar or above for the 6000 K WD model (see Table 4.5). The UVC can become substantially higher for the cool 4000 K WD surface temperature model runs, making those model planet surface environments harsh for life as we know it.

In addition to individual models that represent a planet orbiting a WD at a certain time during the cooling process (i.e., specific WD surface temperatures), we also model two planets through their evolution while the WD cools, representing two possible tracks through a WD's HZ. Both cases show a decrease of ozone for the three points modeled (for WD surface temperature of 6000 K, 5000 K and 4000 K and the corresponding irradiation on the planets) as well as an increase in UVC surface flux over time.

Due to the extreme change in luminosity early in a WD's evolution a temperate planet around a cool WD would have experienced extremely high luminosity and

CHAPTER 4. HABITABLE PLANETS ORBITING WHITE DWARFS

corresponding surface temperature early in its history, what should initiate a runaway greenhouse process and extreme water loss on such planets early in their history.

Whether or not such planets would have lost all their water at that point would depend strongly on the initial water reservoir, and whether it can be replenished, leaving open the question about whether an Earth-like planet could survive around WDs if formed.

However due to the extremely favorable size ratio of an Earth-like planet compared to a WD, as well as the low luminosity of a WD compared to a main sequence host star, WD exoplanets will make interesting targets for characterization.

Chapter 5

Planetary Spectra and Biosignatures of Earth-like Planets Orbiting in the White Dwarf Habitable Zone

*This thesis chapter originally appeared in the literature as Kozakis et al.
(2020) as an Astrophysical Journal Letter.*

5.1 Introduction

The first discovery of a planetesimal orbiting a white dwarf (WD) in 2015 (Vanderburg et al. 2015) has been joined by other recent discoveries (Manser et al. 2019; Gänsicke et al. 2019), which postulate the first indirect detection of a planet orbiting a WD.

The high occurrence rate of heavy metal WD pollution observed by many groups (e.g. Koester & Wilken 2006; Klein et al. 2011; Koester et al. 2014; Hamers & Portegies Zwart

2016; Malamud & Perets 2016) indicate debris disks or planets around a high percentage of WDs of up to 50% (Schreiber et al. 2019). K2 statistics constrain the rate of WD habitable zone (HZ) planet occurrence to $<28\%$ (van Sluijs & Van Eylen 2018b). Several studies have used WD pollution to infer the dynamical evolution (Veras & Fuller 2019; Veras et al. 2019) and the composition of accreting planets (e.g. Swan et al. 2019), with Bauer & Bildsten 2019 finding WD pollution is sometimes consistent with several Earth masses of rocky debris accretion during the early stages of WD cooling, potentially implying close-in terrestrial planets. WD stellar remnants are only slightly larger than Earth, with long cooling timescales, which give them a long-lived, stable WD HZ, which can provide temperature conditions for rocky planets of ~ 8 billion years (Gyr) (Kozakis et al. 2018). Therefore rocky planets in the WD HZ are interesting planets both to search for as well as to characterize second-generation terrestrial planets.

Multiple studies have addressed the possibility of WD planet detection via transits (e.g. Agol 2011; Loeb & Maoz 2013; Cortés & Kipping 2019) and several searches are already underway (e.g. Fulton et al. 2014; Veras & Gänsicke 2015; Xu et al. 2015; Wallach et al. 2018; Bell 2019; Dame et al. 2019). The potential for habitable planets orbiting in the WD HZ during its cooling process (e.g. Agol 2011; Barnes & Heller 2013; Kozakis et al. 2018) and the UV surface environment and its potential impact on surface life have been discussed by several teams (e.g. McCree 1971; Fossati et al. 2012; Kozakis et al. 2018). A first estimate for the strength of transmission spectral features for Earth-like planets around WDs has been explored by Loeb & Maoz (2013), who used the modern Earth transmission spectrum in lieu of atmospheric models for Earth-like planets orbiting WDs. While this was a useful first approach, the different irradiation environment around a WD compared to around the Sun, especially in the UV, changes

the atmospheric composition as well as the spectral features compared to modern Earth. We show the modern Earth transmission spectrum (Kaltenegger & Traub 2009) in our transmission spectra figures for comparison.

This paper provides the first high-resolution transmission spectra database for Earth-like planets orbiting WD from 6,000 to 4,000 K both for planets i) receiving Earth-analog irradiation from the WD at one point in its evolution, as well as ii) for a planet at a specific orbital distance, which would allow for the longest continuous time in the WD HZ during the WD’s evolution (the atmosphere models are discussed in detail in Kozakis et al. 2018). During the WD cooling process planets in the WD HZ will experience a constantly decreasing overall incident flux, along with decreasing incident UV flux, which impact the planet’s climate and atmospheric photochemistry (ibid). Section 2 describes our models, Section 3 presents our results, and Section 4 summarizes and discusses our findings.

5.2 Methods

5.2.1 WD cooling and spectral models

Newly formed WDs are extremely hot (up to 100,000 K), however they gradually cool over time due to a lack of an internal heat source. An average WD has cooled to 6,000 K after ~ 2 Gyr, but then takes an additional ~ 8 Gyr to reach 4,000 K (Bergeron et al. 2001), providing planets nearly twice Earth’s lifetime in the continuous WD HZ (as discussed in detail in Kozakis et al. 2018). To explore WD planet evolution throughout their host’s cooling, we model the photochemistry and climates of such planets using

WD spectral models described in Saumon et al. (2014) for WD hosts at 6,000, 5,000, and 4,000 K. The models assume pure hydrogen atmospheres for the average WD mass of $0.6 M_{\odot}$ (Kepler et al. 2016a). These WD spectra only show hydrogen lines above 5,000 K, and are essentially black bodies under 5,000 K, at which point hydrogen becomes neutral (ibid).

5.2.2 Planetary atmospheric models and spectra

To model planetary atmospheres and resulting spectra we use *Exo-Prime* (see e.g. Kaltenegger 2010) which couples a 1D climate code (based on Kasting & Ackerman 1986; Pavlov et al. 2000; Haqq-Misra et al. 2008), a 1D photochemistry code (based on Pavlov & Kasting 2002; Segura et al. 2005, 2007), and a radiative transfer code (based on Traub & Stier 1976; Kaltenegger & Traub 2009). This code was designed for rocky planets and models temperature, chemical profiles, UV surface fluxes, and emergent and transmission spectra. Figure 5.1 and Table 5.1 summarize the model parameters, temperature and chemical mixing ratios of the WD planet models described in detail in Kozakis et al. (2018).

Using WD irradiation spectra (described above) as incoming irradiation, we divide the atmosphere into 100 parallel layers up to a pressure of 1 mbar. To model planets at the Earth-equivalent distance we scaled the integrated flux of the WD input stellar spectrum to the solar constant. After the models are run, we factor in limitations in the atmospheric depths we can probe due to refraction, which changes based on the geometry of the system. Outgoing light rays must be parallel to reach a distant observer, thus rays that are bent strongly in dense, deep regions of a planetary atmosphere will

not contribute to the observed signal. Due to this effect, an Earth-analog planet's atmosphere at 1AU orbiting a Sun-sized star can only be probed down to about 12.7 km above the planetary surface (e.g. (Bétrémieux & Kaltenegger 2014; Macdonald & Cowan 2019)), while for a planet around a WD, the atmosphere of a planet receiving Earth-analog irradiation can be observed down to 6.5 km above the surface (Macdonald & Cowan 2019). Therefore we cut our spectra off at the effective height equivalent to the system's lowest observable altitude.

All spectra are calculated at high resolution 0.01 cm^{-1} covering wavelengths from 0.4 to $20 \mu\text{m}$ and are publicly available online¹. All transmission spectra are plotted at a resolution of $\lambda/\Delta\lambda = 700$ in the figures for clarity.

5.3 Results: Transmission spectra of Earth-like planets orbiting WDs

5.3.1 Transmission spectra of planets orbiting WDs at the Earth-equivalent distance

As a WD cools, its UV flux steadily decreases, causing significant changes in our model planets' atmospheric photochemistry, which is highly sensitive to the amount of incoming UV radiation (see Figure 5.1) (as discussed in detail in Kozakis et al. 2018 and shortly summarized here). Ozone (O_3) production requires high energy UV photons with $\lambda < 240 \text{ nm}$, causing production rates to decrease for planets orbiting cooler WDs

¹<http://carlsaganinstitute.org/data/>

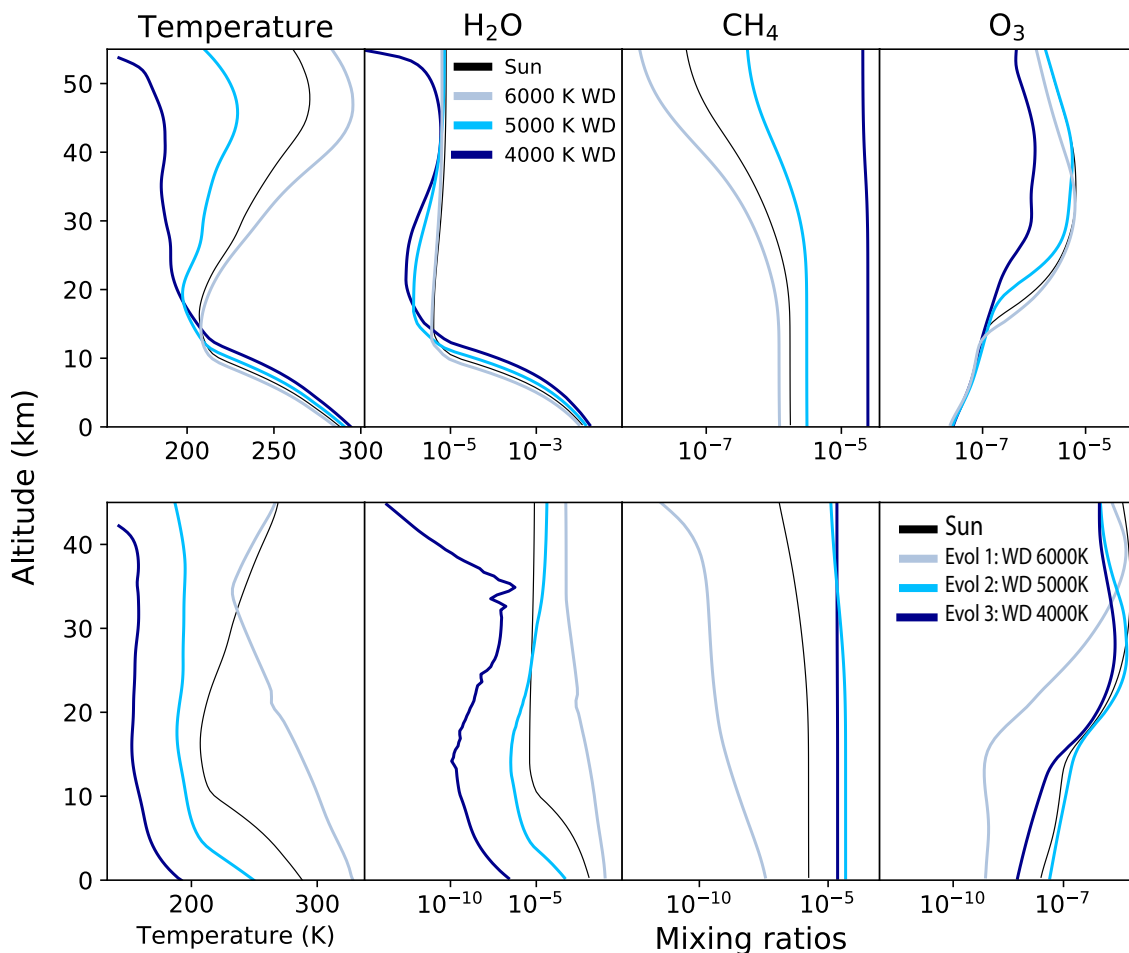


Figure 5.1: Temperature and mixing ratio profiles of Earth-like planet models orbiting WDs (top) at the Earth-equivalent distance and (bottom) on a specific orbit which allows for the maximum time in the WD HZ as the WD cools, shown for 3 evolutionary stages.

with less incident UV, and lowering the atmosphere’s ability to shield the surface from UV radiation. Note that shortward of about 200 nm, absorption by atmospheric CO₂ filters out biologically harmful UV flux (see e.g. discussion in Kozakis et al. 2018; O’Malley-James & Kaltenegger 2019).

The decrease of ozone leads to a decrease of its byproduct hydroxyl (OH), which is one of the main sinks for methane (CH₄). Methane additionally undergoes significant

Table 5.1:: Model summary for Earth-like planets orbiting WD hosts receiving i) Earth-equivalent irradiance and ii) on a specific orbit which allows for the maximum time in the WD HZ as the WD cools, shown for 3 evolutionary stages (Kozakis et al. 2018). We also compare the semimajor axes, a , of these planets to the Roche limit for a rigid satellite, r_{Roche} , which for a WD with a mass of $0.6 M_{\odot}$ and a radius of $0.0128 R_{\odot}$ corresponds to a value of $0.67 R_{\odot}$.

| Stellar host T_{eff} (K) | S_{eff} | a/r_{Roche} | Planet surface T_{eff} (K) | Ozone column depth (cm^{-2}) |
|--------------------------------------|------------------|---------------|--|--|
| Present day Earth | 1.00 | - | 288.2 | 5.4×10^{18} |
| 6000 | 1.00 | 4.5 | 285.6 | 5.7×10^{18} |
| 5000 | 1.00 | 3.1 | 290.8 | 3.9×10^{18} |
| 4000 | 1.00 | 2.0 | 294.3 | 1.8×10^{18} |
| 6000 | 1.34 | 3.9 | 328.4 | 1.7×10^{18} |
| 5000 | 0.64 | 3.9 | 249.6 | 4.4×10^{18} |
| 4000 | 0.26 | 3.9 | 191.9 | 9.6×10^{17} |

depletion during photolysis in high UV environments. Cooler WDs also emit a larger percentage of their light at longer wavelengths, resulting in more efficient planetary surface heating and higher planetary surface temperatures for cooler hosts. Thus with the evolution and cooling of the WD host, atmospheres of Earth-like planets show less ozone, more methane, higher surface temperatures and decreasing temperature inversion in the planetary model atmospheres for similar overall incident flux from cooler WD hosts. Details of the model parameters are shown in Table 5.1 and temperature and chemical profiles are shown in Figure 5.1 for both i) planets orbiting at the Earth-equivalent distance, and ii) a planet on the orbit that allows the maximum time in the HZ during WD cooling.

Figure 5.2 shows our transmission spectra calculated using these atmospheric models from Kozakis et al. (2018), with zoomed in biologically relevant features shown in Figure 5.3. A unique differences between transmission spectra of WDs versus main

sequence stars is the large difference in $(R_p/R_s)^2$, where R_p is the planet's effective radius, and R_s is the radius of the stellar host. This quantity determines the depth of the transit, with larger $(R_p/R_s)^2$ values creating a larger signal. If we were to consider an Earth-sized planet around a Sun-sized star ($R_s = 1 R_\odot$) versus a WD ($R_s = 0.00128 R_\odot$), the corresponding $(R_p/R_s)^2$ values for the planet without considering any atmospheric absorption would be 8.4×10^{-5} and 5.1×10^{-1} , respectively. With similar effective atmospheric heights for both cases, the contrast ratio is 4 orders of magnitudes larger for such planets orbiting WDs. In Figure 5.2 the Earth-Sun transmission spectra were multiplied by 1.65×10^4 to show on the same contrast ratio scale as the WD planet model spectra. The transmission spectra in Figure 5.2 are shown at a resolution of $\lambda/\Delta\lambda = 700$ for clarity.

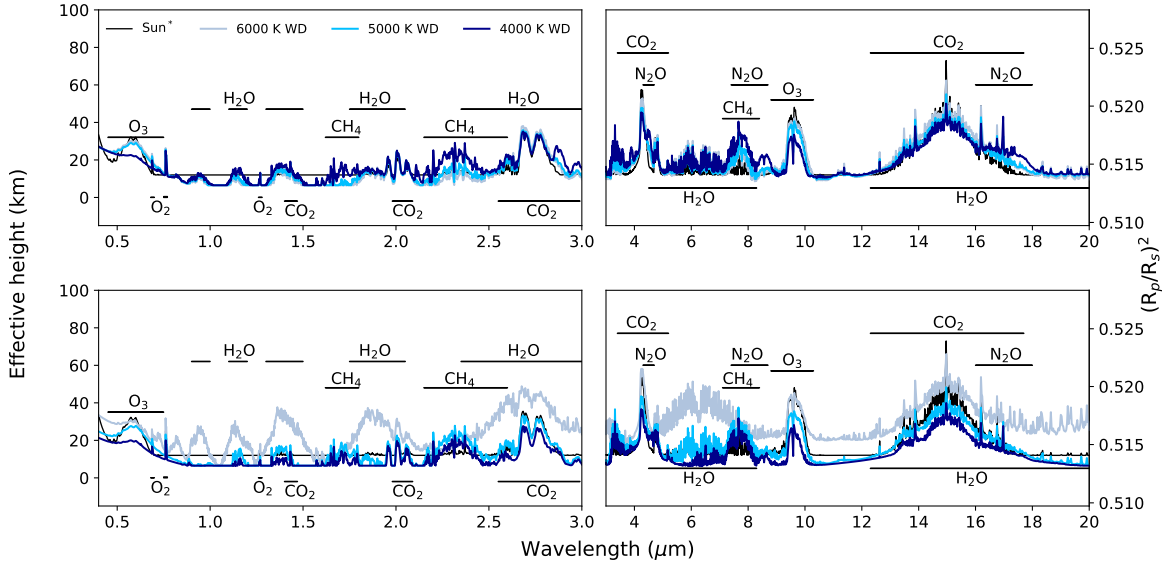


Figure 5.2: Transmission spectra for (top) planets orbiting at the Earth-equivalent distance and (bottom) a planet with a static semimajor axis 3.9 times the Roche limit throughout WD cooling for 3 evolutionary stages (4,000, 5,000, and 6,000 K WD) both in terms of effective height (left axis) and $(R_p/R_s)^2$ (right axis). Major spectral features are labeled. The Earth-Sun system is shown for comparison. Note that the transmission spectra of Earth is multiplied by 1.65×10^4 to show on the same contrast ratio scale for comparison.

H₂O: Although the higher surface temperatures for the cooler WD hosts result in increased water abundance in the upper atmosphere than for hotter WD hosts, the spectral features are dominated by the lower atmosphere, thus water features are stronger for planet models orbiting hotter WDs, because larger amounts of ozone protect the water from depletion via photolysis (see Figure 5.1). The strongest H₂O transmission spectra absorption features can be seen in Figure 5.2 at 0.9, 1.4, 1.9, 5 and 20 μm .

O₂: The strongest O₂ features in the transmission spectra models in the modeled wavelength range from 0.4 to 20 μm is at 0.76 μm (see Figure 5.3 for a detailed view). All model atmospheres assume a O₂ mixing ratios of 0.21, leading to similar strength of the oxygen absorption line. The differences are due to overlapping features.

O₃: The two strongest O₃ spectral features in our transmission spectra models are at 0.6 and 9.6 μm (seen in Figure 5.3). The spectral features increase for hotter WD hosts due to higher production rates of ozone.

CH₄: The strongest CH₄ absorption features in transmission are at 1.7 and 7.6 μm (seen in Figure 5.3). CH₄ absorption features are stronger in the atmosphere for the coolest WD case, where its concentration increases because of the lower UV environment causing less depletion via photolysis as well as less reactions with OH, a byproduct of ozone, which is also reduced in the atmosphere for cool WDs.

CO₂: The strongest CO₂ absorption features in transmission are at 2.0, 2.7, and 15 μm . CO₂ is set to a fixed mixing ratio of modern Earth concentration for all models and the absorption features shows comparable strength for all model planets.

N₂O: The strongest N₂O absorption features in transmission are at 4.4, 8, and 17 μm (see Figure 5.3 for details on the 17 μm feature). N₂O is depleted similarly to CH₄

around hotter WD hosts due to increased photolysis and reactions via OH.

The most prominent spectral features of potential biosignatures in the visible to NIR in transmission are O_3 at $0.6 \mu\text{m}$, CH_4 at $1.7 \mu\text{m}$ and O_2 at $0.76 \mu\text{m}$, and in the IR O_3 at $9.6 \mu\text{m}$, CH_4 at $7.6 \mu\text{m}$, and N_2O at $17 \mu\text{m}$. These spectral features are shown in detail in Figure 5.3 (top: visible to NIR 0.4 to $3 \mu\text{m}$, bottom IR 3 to $20 \mu\text{m}$) for planets orbiting at the Earth-equivalent distance.

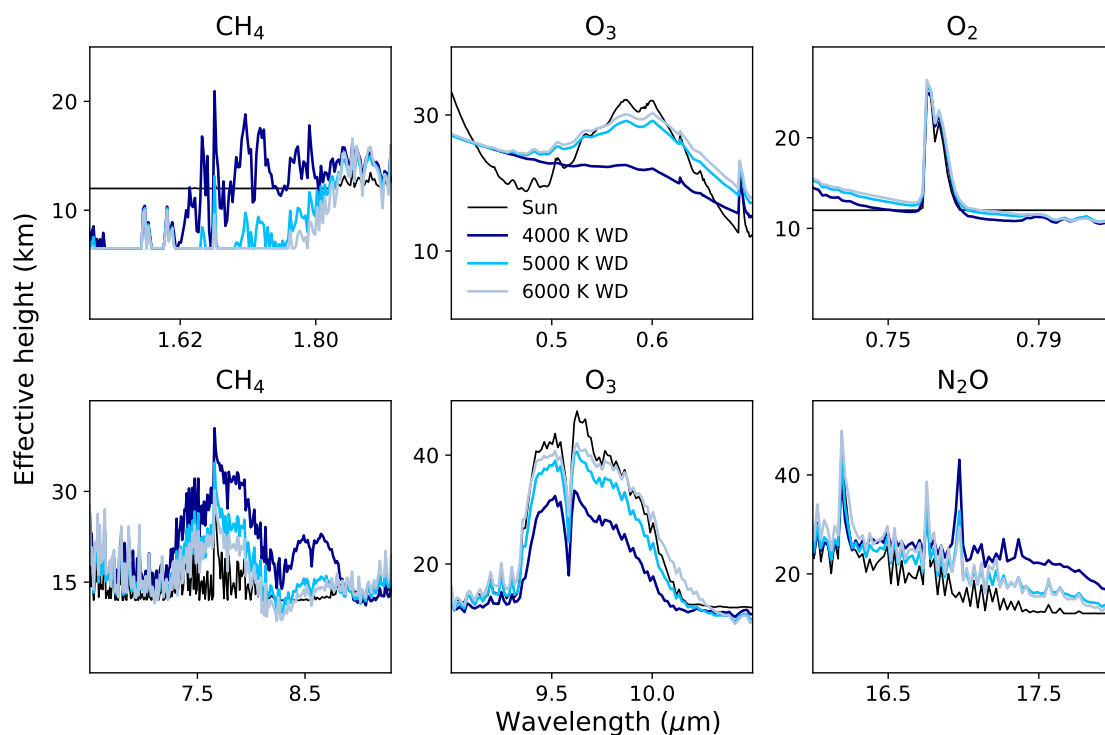


Figure 5.3: The most prominent spectral features for potential biosignatures of planets orbiting at the Earth-equivalent distance in the (top) visible to near-IR for O_3 at $0.6 \mu\text{m}$, CH_4 at $1.7 \mu\text{m}$ and O_2 at $0.76 \mu\text{m}$ and in the IR (bottom) for O_3 at $9.6 \mu\text{m}$, CH_4 at $7.6 \mu\text{m}$ and N_2O at $17 \mu\text{m}$. The black line shows the modern Earth-Sun system for comparison.

5.3.2 Transmission spectra of rocky planets in the WD HZ throughout white dwarf cooling

An average WD takes about ~ 8 Gyr to cool from 6,000 K to 4,000 K (Bergeron et al. 2001), providing a stable, continuous WD HZ during that time (discussed in detail in Kozakis et al. 2018). A planet orbiting at a semimajor axis 3.9 times the Roche limit from its WD host would spend ~ 6 Gyr in the conservative WD HZ, and ~ 8.5 Gyr in the empirical WD HZ (ibid) using empirical HZ limits based on early Mars and recent Venus irradiation (Kasting et al. 1993). Such a planet would initially (Evolution stage 1) receive 134% of modern Earth's flux from its 6,000 K WD host, which reduces to 64% for a WD which cooled to 5,000 K (Evolution stage 2), and 26% of modern Earth's flux when the WD cools to 4,000 K (Evolution stage 3). This change in irradiation is similar to a planet at an orbital distance between Venus and modern Earth, to a Mars orbit in our solar system.

During this WD cooling process the amount of incident UV flux upon the planet steadily decreases, changing the planet's atmospheric chemistry as well as its UV surface environment. Details of the model parameters from Kozakis et al. (2018) are shown in Table 5.1 and temperature and mixing ratio profiles are shown in the bottom row of Figure 5.1. We summarize the results here to link them to the spectral features shown in Figure 5.2, with specific biologically relevant features shown in Figure 5.4.

At the first stage in the modeled evolution of such a WD planet, for a 6,000 K WD host such a planet receives high UV flux, causing large ozone production as well as high rates of photolysis in the model atmospheres. O_3 , CH_4 , and N_2O are significantly depleted via photolysis. The high total incident flux causes high surface temperatures

and thus high amount of water vapor throughout the atmosphere.

At the second stage of the modeled evolution, for a 5,000 K WD, with a decreasing incident UV and overall flux the planet shows a substantial ozone layer because of reduced O_3 depletion via photolysis. The concentration of CH_4 and N_2O also increase compared to the first stage because of reduced depletion via photolysis.

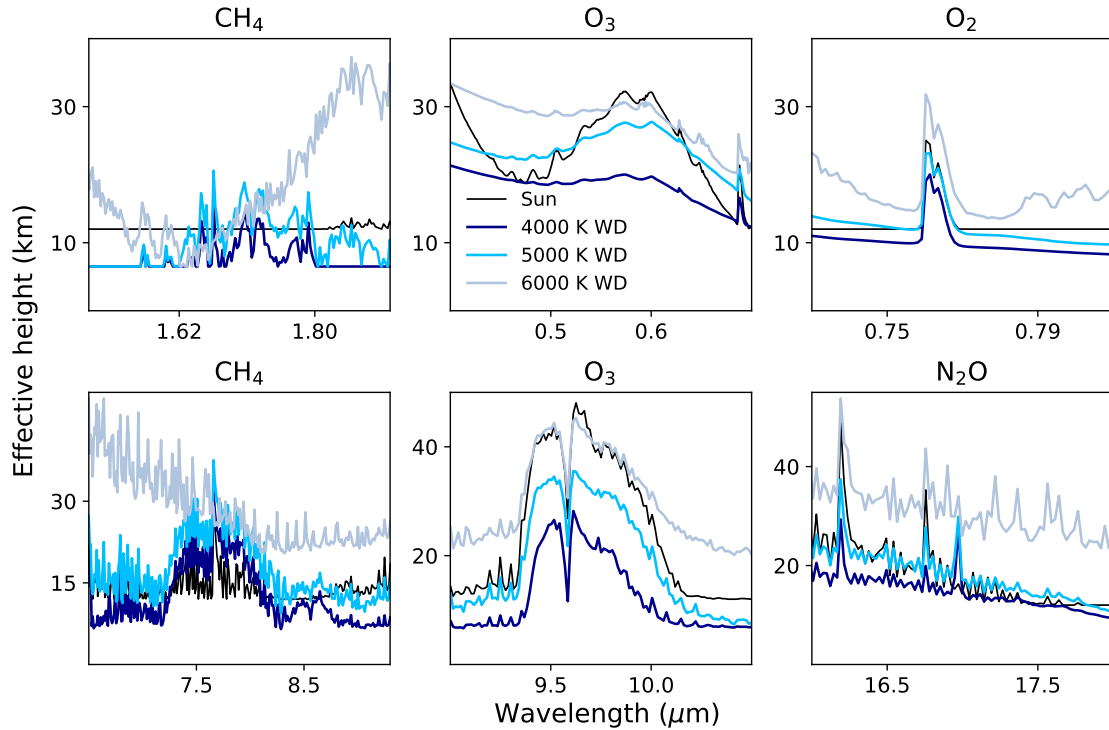


Figure 5.4: The most prominent spectral features for potential biosignatures shown in the (top) visible to near-infrared for O_3 at $0.6 \mu m$, CH_4 at $1.7 \mu m$ and O_2 at $0.76 \mu m$, and in the IR (bottom) for O_3 at $9.6 \mu m$, CH_4 at $7.6 \mu m$ and N_2O at $17 \mu m$ for a rocky planet at an orbital distance, which allows for maximum time in the WD HZ shown at 3 points throughout the WDs cooling process (at 6,000, 5,000, and 4,000 K WD host effective surface temperature). The modern Earth-Sun system spectra is shown for comparison.

At the third stage, for a 4,000 K WD host, the reduced incident flux causes cold surface temperatures and very low photolysis rates. Only a small amount of ozone is produced in our models and there is very little depletion via photolysis for all

chemical species. Due to the low surface temperature, water concentration is also lower. Note that we did not consider in our models that a similar geological cycle to Earth's carbonate-silicate cycle could increase the CO_2 concentration in the atmosphere of such colder planets, maintaining warm surface temperatures than shown in our models (see Kozakis et al. 2018).

Most notable in Figure 5.2 are the differences in H_2O absorption, caused by the decrease of H_2O for a cooling WD host. High ozone production rates in the first evolution stage for the 6000 K WD produce stronger ozone features in evolution stage 1. Methane shows stronger absorption features for the later evolution stages 2 and 3, the two cooler WD cases, where photolysis rates are low.

The most prominent spectral features of potential biosignatures in the visible to NIR in transmission are O_3 at $0.6 \mu\text{m}$, CH_4 at $1.7 \mu\text{m}$, and O_2 at $0.76 \mu\text{m}$, and in the IR O_3 at $9.6 \mu\text{m}$, CH_4 at $7.6 \mu\text{m}$ and N_2O at $17 \mu\text{m}$. These spectral features are shown in detail in Figure 5.4 (top: visible to NIR 0.4 to $3 \mu\text{m}$, bottom IR 3 to $20 \mu\text{m}$) for the planetary evolution models for a cooling WD host.

5.4 Discussion & Conclusion

Due to the similarity in size to Earth and relatively stable environments, WDs are very interesting places to search for and characterize Earth-sized HZ planets. The contrast ratio between Earth-sized planets and their small WD hosts are several orders of magnitudes higher than for an Earth-sized planet around a main sequence star, however no such planet has been found yet. Finding and characterizing such planets in

the HZ of WDs is challenging for several reasons. Due to the small size of WDs, such planets have a significantly lower transit probability than around main-sequence stars' HZs (Loeb & Maoz 2013). Although transits of HZ planets would occur very frequently (<10 hr orbital periods) their transit would only last a few minutes. It is also important to note that the close-in separation of the WD HZ would cause planets to experience extreme tidal forces. Veras et al. (2019) finds that often Earth-sized planets orbiting at less than 10 times their WD's Roche limit would tidally disrupted, implying low chances of survival for the planetary orbits described in this paper ($a/r_{roche} = 2 - 4.5$, Table 5.1). In addition, cool white dwarfs have a very low flux due to their small size, limiting our search for such planets to nearby targets.

However finding rocky planets in the HZ of WDs would allow first insights into the composition and environment of such second-generation planets and the intriguing question whether they could support life. Here we present high-resolution transmission spectra for Earth-like planets orbiting WDs at the Earth-equivalent distance as well as explore how a rocky planet in the HZ of a WD would evolve through the several billion year timescale when the WD host would provide a stable temperature environment.

While finding rocky planets in the HZ of a WD is extremely challenging, we shows that upcoming telescopes could characterize the atmospheres of such potentially Earth-like planets, if they exist. All high-resolution transmission spectra are available online² and can be used as a tool to prepare and interpret upcoming observations with JWST, the Extremely Large Telescopes, as well as mission concepts like Origins, HabEx, and LUVOIR.

²<http://carlsaganinstitute.org/data/>

Part IV

Conclusions

Chapter 6

Conclusions and future prospects

This thesis examines habitable zone evolution, atmospheric chemistry/climate, and spectra for planets around red giants and white dwarfs.

Chapter 2 shows that planets orbiting red giants above $2 M_{\odot}$ can experience longer times in the habitable zone than around less massive stars, due to the lack of a helium flash and a resulting longer horizontal branch. Since red giants experience a drop in temperature during expansion, most planets in these systems would experience less incident UV with time, potentially causing build-ups of species such as CH_4 that are susceptible to photolysis, which in turn can heat a planet. The reduced incident UV flux would additionally lower ozone production rates, leading to an increase in the amount of harmful UV reaching the planetary surface. Since the HZ separation for red giants would be at large orbital distances, Chapter 3 simulates reflected light and emission spectra rather than transmission spectra for such planets. Although this extra separation would allow easier direct measurements, the large luminosities of red giants will require higher contrast measurements.

CHAPTER 6. CONCLUSIONS AND FUTURE PROSPECTS

Chapter 4 demonstrates that after a white dwarf’s initially rapid cooling, at temperatures of ~ 6000 K the environment becomes stable enough that a planet could remain in the HZ for 6 Gyr, even using conservative limits. As the white dwarf cools its UV flux decreases, therefore ozone production decreases and there would be less depletion of CH_4 , N_2O , CH_3Cl , potentially improving the detectability of biosignatures. However, the HZ would be extremely close to the white dwarf (~ 0.01 AU), requiring a very circular orbit to prevent tidal disruption. Simulated transmission spectra in Chapter 5 demonstrate one of the most compelling reasons to search for life around white dwarfs: transit depths that often exceed 50%. Note that the transit of such planets would only last several minutes, making them challenging to detect with current searches.

After modeling the atmospheres of such planets, the next step to learning how to search for life around red giants and white dwarfs is to simulate their planetary spectra for upcoming telescopes. Such studies for JWST for white dwarf planet transmission can be done using Pandexo (Batalha et al. 2017), which contains JWST-specific noise models to simulate transmission spectra with error bars. While simulators for ground-based telescopes like ELT are not yet readily available, some proposed mission concept simulators exist for WFIRST and LUVOIR, which could be used to simulate observations of red giant emergent spectra (Robinson et al. 2016; Lustig-Yaeger et al. 2019b).

From an observational point of view, finding rocky planets in the HZ of red giants and white dwarfs to characterize will be an essential step. Although there are a number of known planets around red giants, that is still not the case for white dwarfs. However, TESS will soon begin to take 2 minute, and occasionally 20 second cadence data (Prins et al. 2019), which will be required for detecting planets in the HZ of white dwarfs, as they typically have transit durations of only several minutes for white dwarf with surface

CHAPTER 6. CONCLUSIONS AND FUTURE PROSPECTS

temperatures between 6000 and 4000 K.

Within the next decade we expect to see the launch of JWST, the first light of the ELTs, and possibly WFIRST. Past that we can hope to see space telescopes such as HabEx, Origins Telescope or LUOVIR. These telescopes will provide the next big step in our search for life.

This thesis demonstrates that hosts outside the main sequence can be characterized and could give us insights into life beyond what planets around main sequence hosts could answer. Actual data of terrestrial atmospheres will undoubtedly surprise us in ways we cannot possibly predict. To prepare for using the available time to observe effectively, it is critical to continue to explore potential parameter spaces in order to further our toolkit for the search for life in the universe, to finally answer the age old question “Are we alone?”

References

Agol, E. 2011, *ApJ*, 731, L31

Albarède, F. 2009, *Nature*, 461, 1227

Anglada-Escudé, G., Amado, P. J., Barnes, J., et al. 2016, *Nature*, 536, 437

Arney, G. N., Meadows, V. S., Domagal-Goldman, S. D., et al. 2017, *ApJ*, 836, 49

Baglin, A., Auvergne, M., Barge, P., et al. 2006, in *ESA Special Publication, Vol. 1306, The CoRoT Mission Pre-Launch Status - Stellar Seismology and Planet Finding*, ed. M. Fridlund, A. Baglin, J. Lochard, & L. Conroy, 33

Barbato, D., Bonomo, A. S., Sozzetti, A., & Morbidelli, R. 2018, arXiv e-prints, arXiv:1811.08249

Barnes, R., & Heller, R. 2013, *Astrobiology*, 13, 279

Barnes, R., Meadows, V. S., & Evans, N. 2015, *ApJ*, 814, 91

Baross, J. A., & Hoffman, S. E. 1985, *Origins of Life*, 15, 327

Batalha, N. E., Mandell, A., Pontoppidan, K., et al. 2017, *PASP*, 129, 064501

Battersby, C., Armus, L., Bergin, E., et al. 2018, *Nature Astronomy*, 2, 596

REFERENCES

- Baud, B., & Habing, H. J. 1983, *A&A*, 127, 73
- Bauer, E. B., & Bildsten, L. 2019, *ApJ*, 872, 96
- Beer, M. E., King, A. R., Livio, M., & Pringle, J. E. 2004, *MNRAS*, 354, 763
- Bell, K. J. 2019, arXiv e-prints, arXiv:1911.07889
- Benneke, B., Knutson, H. A., Lothringer, J., et al. 2019, *Nature Astronomy*, 3, 813
- Benvenuto, O. G., Althaus, L. G., & Torres, D. F. 1999, *MNRAS*, 305, 905
- Bergeron, P., Leggett, S. K., & Ruiz, M. T. 2001, *ApJS*, 133, 413
- Bergeron, P., Ruiz, M. T., & Leggett, S. K. 1997, *ApJS*, 108, 339
- Bertelli, G., Girardi, L., Marigo, P., & Nasi, E. 2008, *A&A*, 484, 815
- Bertelli, G., Nasi, E., Girardi, L., & Marigo, P. 2009, *A&A*, 508, 355
- B  tr  mieux, Y., & Kaltenegger, L. 2013, *ApJ*, 772, L31
- B  tr  mieux, Y., & Kaltenegger, L. 2014, *ApJ*, 791, 7
- Beuzit, J.-L., Feldt, M., Dohlen, K., et al. 2008, *Society of Photo-Optical Instrumentation Engineers (SPIE) Conference Series*, Vol. 7014, SPHERE: a 'Planet Finder' instrument for the VLT, 701418
- Birkby, J. L. 2018, *Spectroscopic Direct Detection of Exoplanets*, 16
- Bolcar, M. R., Feinberg, L., France, K., et al. 2016, *Society of Photo-Optical Instrumentation Engineers (SPIE) Conference Series*, Vol. 9904, Initial technology assessment for the Large-Aperture UV-Optical-Infrared (LUVOIR) mission concept study, 99040J

REFERENCES

- Bonneau, D., Josse, M., & Labyrie, A. 1975, *Astrophysics and Space Science Library*, Vol. 54, Lock-In Image Subtraction Detectability of Circumstellar Planets with the Large Space Telescope, ed. C. de Jager & H. Nieuwenhuijzen, 403
- Borucki, W. J., Koch, D., Basri, G., et al. 2010, *Science*, 327, 977
- Brogi, M., de Kok, R. J., Birkby, J. L., Schwarz, H., & Snellen, I. A. G. 2014, *A&A*, 565, A124
- Brown, T. M. 2001, *ApJ*, 553, 1006
- Bruno, G. 1584, *De Infinito universo et mundi*
- Canto, J., & Raga, A. C. 1991, *ApJ*, 372, 646
- Catling, D. C., Krissansen-Totton, J., Kiang, N. Y., et al. 2018, *Astrobiology*, 18, 709
- Chapman, S. A. 1930, *Mem. R. Met. Soc.*, 3, 103
- Charbonneau, D., Brown, T. M., Latham, D. W., & Mayor, M. 2000, *ApJ*, 529, L45
- Chauvin, G., Lagrange, A. M., Dumas, C., et al. 2004, *A&A*, 425, L29
- Chen, H., Wolf, E. T., Zhan, Z., & Horton, D. E. 2019, *ApJ*, 886, 16
- Cocconi, G., & Morrison, P. 1959, *Nature*, 184, 844
- Cockell, C. S. 1998, *Biological Journal of the Linnean Society*, 63, 449
- Cockell, C. S. 1999, *Planet. Space Sci.*, 47, 1487
- Cockell, C. S. 2014, *Philosophical Transactions of the Royal Society of London Series A*, 372, 20130082

REFERENCES

- Cortés, J., & Kipping, D. 2019, MNRAS, 488, 1695
- Cowan, N. B., Agol, E., Meadows, V. S., et al. 2009, ApJ, 700, 915
- Dame, K., Belardi, C., Kilic, M., et al. 2019, MNRAS, 490, 1066
- Danchi, W. C., & Lopez, B. 2013, ApJ, 769, 27
- Demarais, N. J., Yang, Z., Martinez, O., et al. 2012, ApJ, 746, 32
- Deming, D., Brown, T. M., Charbonneau, D., Harrington, J., & Richardson, L. J. 2005, ApJ, 622, 1149
- Deming, D., Richardson, L. J., & Harrington, J. 2007, MNRAS, 378, 148
- Demory, B.-O., Gillon, M., Seager, S., et al. 2012, ApJ, 751, L28
- Des Marais, D. J., Harwit, M. O., Jucks, K. W., et al. 2002, Astrobiology, 2, 153
- Des Marais, D. J., Nuth, Joseph A., I., Allamandola, L. J., et al. 2008, Astrobiology, 8, 715
- Diamond-Lowe, H., Stevenson, K. B., Bean, J. L., Line, M. R., & Fortney, J. J. 2014, ApJ, 796, 66
- Diffey, B. L. 1991, Rev Phys Med Biology, 36, 299
- Domagal-Goldman, S. D., Segura, A., Claire, M. W., Robinson, T. D., & Meadows, V. S. 2014, ApJ, 792, 90
- Doyle, L. R., Carter, J. A., Fabrycky, D. C., et al. 2011, Science, 333, 1602
- Drake, F. D. 1961, Physics Today, 14, 40

REFERENCES

- Drake, F. D. 1965, *Current Aspects of Exobiology*, 323
- Dressing, C. D., & Charbonneau, D. 2015, *ApJ*, 807, 45
- Dyson, F. J. 1960, *Science*, 131, 1667
- Farihi, J. 2016, *New A Rev.*, 71, 9
- Farihi, J., Gänsicke, B. T., & Koester, D. 2013, *Science*, 342, 218
- Feng, Y. K., Robinson, T. D., Fortney, J. J., et al. 2018, *AJ*, 155, 200
- Fontaine, G., Brassard, P., & Bergeron, P. 2001, *PASP*, 113, 409
- Ford, E. B., Seager, S., & Turner, E. L. 2001, *Nature*, 412, 885
- Forget, F., & Pierrehumbert, R. T. 1997, *Science*, 278, 1273
- Fossati, L., Bagnulo, S., Haswell, C. A., et al. 2012, *ApJ*, 757, L15
- Fossati, L., Bagnulo, S., Haswell, C. A., et al. 2015, in *IAU Symposium*, Vol. 305, *Polarimetry*, ed. K. N. Nagendra, S. Bagnulo, R. Centeno, & M. Jesús Martínez González, 325–332
- Fujii, Y., Kawahara, H., Suto, Y., et al. 2011, *ApJ*, 738, 184
- Fujii, Y., Angerhausen, D., Deitrick, R., et al. 2018, *Astrobiology*, 18, 739
- Fulton, B. J., Tonry, J. L., Flewelling, H., et al. 2014, *ApJ*, 796, 114
- Furnes, H., Banerjee, N. R., Muehlenbachs, K., Staudigel, H., & de Wit, M. 2004, *Science*, 304, 578
- Gaia Collaboration, Brown, A. G. A., Vallenari, A., et al. 2016, *A&A*, 595, A2

REFERENCES

- Gaidos, E. 2013, *ApJ*, 770, 90
- Gänsicke, B. T., Schreiber, M. R., Toloza, O., et al. 2019, *Nature*, 576, 61
- Garber, S. J. 1999, *Journal of the British Interplanetary Society*, 52, 3
- Gardner, J. P., Mather, J. C., Clampin, M., et al. 2006, *Space Sci. Rev.*, 123, 485
- Giammichele, N., Bergeron, P., & Dufour, P. 2012, *ApJS*, 199, 29
- Gilbert, E. A., Barclay, T., Schlieder, J. E., et al. 2020, arXiv e-prints, arXiv:2001.00952
- Gillon, M., Triaud, A. H. M. J., Demory, B.-O., et al. 2017, *Nature*, 542, 456
- Gilmozzi, R., & Spyromilio, J. 2007, *The Messenger*, 127, 11
- Gómez-Leal, I., Kaltenegger, L., Lucarini, V., & Lunkeit, F. 2018, *ApJ*, 869, 129
- Gordon, I. E., Rothman, L. S., Tan, Y., Kochanov, R. V., & Hill, C. 2017, in 72nd International Symposium on Molecular Spectroscopy, TJ08
- Green, J., Schechter, P., Baltay, C., et al. 2012, arXiv e-prints, arXiv:1208.4012
- Grenfell, J. L., Gebauer, S., v. Paris, P., Godolt, M., & Rauer, H. 2014, *Planet. Space Sci.*, 98, 66
- Grenfell, J. L., Stracke, B., von Paris, P., et al. 2007, *Planet. Space Sci.*, 55, 661
- Grunblatt, S., Huber, D., Lopez, E., Gaidos, E., & Livingston, J. 2017, Measuring Precise Radii of Giants Orbiting Giants to Distinguish Between Planet Evolution Models, Spitzer Proposal
- Haghighipour, N., & Kaltenegger, L. 2013, *ApJ*, 777, 166

REFERENCES

- Hamers, A. S., & Portegies Zwart, S. F. 2016, *MNRAS*, 462, L84
- Haqq-Misra, J. D., Domagal-Goldman, S. D., Kasting, P. J., & Kasting, J. F. 2008, *Astrobiology*, 8, 1127
- Harman, S., Schottelkotte, J., & Kasting, J. 2015, in *Pathways Towards Habitable Planets*, 46
- Hart, H. M., & Jakosky, B. M. 1987, in *Lunar and Planetary Science Conference*, Vol. 18, *Lunar and Planetary Science Conference*, 387
- Hart, M. H. 1975, *QJRAS*, 16, 128
- Hart, M. H. 1979, *Icarus*, 37, 351
- Hegde, S., Paulino-Lima, I. G., Kent, R., Kaltenegger, L., & Rothschild, L. 2015, *Proceedings of the National Academy of Science*, 112, 3886
- Helling, C. 2019, *Annual Review of Earth and Planetary Sciences*, 47, 583
- Hibbert, C. 2011 (DK Publishing, ISBN-10 0756671299)
- Houghton, J., Meira Filho, L., Bruce, J., et al. 2004, *Climate Change*
- Howell, S. B., Sobeck, C., Haas, M., et al. 2014, *PASP*, 126, 398
- Hsu, D. C., Ford, E. B., Ragozzine, D., & Ashby, K. 2019, *AJ*, 158, 109
- Huang, S.-S. 1959, *American Scientist*, 47, 397
- Hubble, E. P. 1926, *ApJ*, 64, 321
- Ingersoll, A. P. 1969, *Journal of Atmospheric Sciences*, 26, 1191

REFERENCES

- Jiang, J. H., & Zhu, S. 2018, *Research Notes of the American Astronomical Society*, 2, 185
- Jones, M. I., Jenkins, J. S., Bluhm, P., Rojo, P., & Melo, C. H. F. 2014, *A&A*, 566, A113
- Joshi, M. 2003, *Astrobiology*, 3, 415
- Jura, M., & Xu, S. 2010, *AJ*, 140, 1129
- Jura, M., & Young, E. D. 2014, *Annual Review of Earth and Planetary Sciences*, 42, 45
- Kaltenegger, L. 2010, *ApJ*, 712, L125
- Kaltenegger, L. 2017, *ARA&A*, 55, 433
- Kaltenegger, L., & Haghighipour, N. 2013, *ApJ*, 777, 165
- Kaltenegger, L., Lin, Z., & Madden, J. 2020, *ApJ*, 892, L17
- Kaltenegger, L., Pepper, J., Stassun, K., & Oelkers, R. 2019, *ApJ*, 874, L8
- Kaltenegger, L., Sasselov, D., & Rugheimer, S. 2013, *ApJ*, 775, L47
- Kaltenegger, L., & Traub, W. A. 2009, *ApJ*, 698, 519
- Kaltenegger, L., Traub, W. A., & Jucks, K. W. 2007, *ApJ*, 658, 598
- Kaltenegger, L., Selsis, F., Fridlund, M., et al. 2010, *Astrobiology*, 10, 89
- Kane, S. R., & Hinkel, N. R. 2013, *ApJ*, 762, 7
- Kane, S. R., Hill, M. L., Kasting, J. F., et al. 2016, *ApJ*, 830, 1

REFERENCES

- Kardashev, N. S. 1964, *Soviet Ast.*, 8, 217
- Kasting, J. F. 1988, *Icarus*, 74, 472
- Kasting, J. F., & Ackerman, T. P. 1986, *Science*, 234, 1383
- Kasting, J. F., & Catling, D. 2003, *ARA&A*, 41, 429
- Kasting, J. F., Holland, H. D., & Pinto, J. P. 1985, *J. Geophys. Res.* 90, 10497
- Kasting, J. F., Whitmire, D. P., & Reynolds, R. T. 1993, *Icarus*, 101, 108
- Kawahara, H., Matsuo, T., Takami, M., et al. 2012, *ApJ*, 758, 13
- Kawashima, Y., & Rugheimer, S. 2019, *AJ*, 157, 213
- Kepler, S. O., Koester, D., & Ourique, G. 2016a, *Science*, 352, 67
- Kepler, S. O., Pelisoli, I., Koester, D., et al. 2016b, *MNRAS*, 455, 3413
- Kerwin, B. A., & Remmele, R. L., J. 2007, *J. Pharm. Sci.*, 96, 1468
- Kilic, M., Kowalski, P. M., Reach, W. T., & von Hippel, T. 2009a, *ApJ*, 696, 2094
- Kilic, M., Kowalski, P. M., & von Hippel, T. 2009b, *AJ*, 138, 102
- Kitzmann, D., Patzer, A. B. C., von Paris, P., Godolt, M., & Rauer, H. 2011a, *A&A*, 531, A62
- Kitzmann, D., Patzer, A. B. C., von Paris, P., Godolt, M., & Rauer, H. 2011b, *A&A*, 534, A63
- Klein, B., Jura, M., Koester, D., & Zuckerman, B. 2011, *ApJ*, 741, 64

REFERENCES

- Knutson, H. A., Charbonneau, D., Allen, L. E., Burrows, A., & Megeath, S. T. 2008, *ApJ*, 673, 526
- Koester, D., Gänsicke, B. T., & Farihi, J. 2014, *A&A*, 566, A34
- Koester, D., & Wilken, D. 2006, *A&A*, 453, 1051
- Koll, D. D. B., Malik, M., Mansfield, M., et al. 2019, *ApJ*, 886, 140
- Konacki, M., Torres, G., Jha, S., & Sasselov, D. D. 2003, *Nature*, 421, 507
- Kopparapu, R. K., Ramirez, R. M., SchottelKotte, J., et al. 2014, *ApJ*, 787, L29
- Kopparapu, R. k., Wolf, E. T., Arney, G., et al. 2017, *ApJ*, 845, 5
- Kopparapu, R. k., Wolf, E. T., Haqq-Misra, J., et al. 2016, *ApJ*, 819, 84
- Kopparapu, R. K., Ramirez, R., Kasting, J. F., et al. 2013, *ApJ*, 770, 82
- Kowalski, P. M., & Saumon, D. 2006, *ApJ*, 651, L137
- Kozakis, T., & Kaltenegger, L. 2019a, *ApJ*, 875, 99
- Kozakis, T., & Kaltenegger, L. 2019b, arXiv e-prints, arXiv:2001.00050
- Kozakis, T., Kaltenegger, L., & Hoard, D. W. 2018, *ApJ*, 862, 69
- Kozakis, T., Lin, Z., & Kaltenegger, L. 2020, *ApJ*, 894, L6
- Kreidberg, L., Bean, J. L., Désert, J.-M., et al. 2014, *ApJ*, 793, L27
- Kreidberg, L., Koll, D. D. B., Morley, C., et al. 2019, *Nature*, 573, 87
- Krissansen-Totton, J., Bergsman, D. S., & Catling, D. C. 2016, *Astrobiology*, 16, 39

REFERENCES

- Krissansen-Totton, J., Garland, R., Irwin, P., & Catling, D. C. 2018, *AJ*, 156, 114
- Kulikov, Y. N., Lammer, H., Lichtenegger, H. I. M., et al. 2007, *Space Sci. Rev.*, 129, 207
- Kunitomo, M., Ikoma, M., Sato, B., Katsuta, Y., & Ida, S. 2011, *ApJ*, 737, 66
- Lammer, H., Bredehöft, J. H., Coustenis, A., et al. 2009, *A&A Rev.*, 17, 181
- Lecote, J., Forget, F., Charnay, B., et al. 2013, *A&A*, 554, A69
- Lecote, J., Wu, H., Menou, K., & Murray, N. 2015, *Science*, 347, 632
- Lederberg, J. 1965, *Nature*, 207, 9
- Leger, A., Pirre, M., & Marceau, F. J. 1993, *A&A*, 277, 309
- Lilly, J. C. 1961, New York: Doubleday
- Lin, H. W., Gonzalez Abad, G., & Loeb, A. 2014, *ApJ*, 792, L7
- Lin, Z., & Kaltenegger, L. 2020, *MNRAS*, 491, 2845
- Line, M. R., Stevenson, K. B., Bean, J., et al. 2016, *AJ*, 152, 203
- Lippincott, E. R., Eck, R. V., Dayhoff, M. O., & Sagan, C. 1967, *ApJ*, 147, 753
- Lissauer, J. J., Dawson, R. I., & Tremaine, S. 2014, *Nature*, 513, 336
- Loeb, A., & Maoz, D. 2013, *MNRAS*, 432, L11
- Lopez, B., Schneider, J., & Danchi, W. C. 2005, *ApJ*, 627, 974
- Lopez, E. D., & Fortney, J. J. 2016, *ApJ*, 818, 4

REFERENCES

- Lorenz, R. D., Lunine, J. I., & McKay, C. P. 1997, *Geophys. Res. Lett.*, 24, 2905
- Lovelock, J. E. 1965, *Nature*, 207, 568
- Lovis, C., Snellen, I., Mouillet, D., et al. 2017, *A&A*, 599, A16
- Luck, R. E., & Heiter, U. 2005, *AJ*, 129, 1063
- Lustig-Yaeger, J., Meadows, V. S., & Lincowski, A. P. 2019a, *AJ*, 158, 27
- Lustig-Yaeger, J., Robinson, T., & Arney, G. 2019b, *The Journal of Open Source Software*, 4, 1387
- Macdonald, E. J. R., & Cowan, N. B. 2019, *MNRAS*, 489, 196
- Macintosh, B. A., Graham, J. R., Palmer, D. W., et al. 2008, *Society of Photo-Optical Instrumentation Engineers (SPIE) Conference Series*, Vol. 7015, *The Gemini Planet Imager: from science to design to construction*, 701518
- Madden, J., & Kaltenegger, L. 2020, *MNRAS*, arXiv:2001.00085
- Maher, K. A., & Stevenson, D. J. 1988, *Nature*, 331, 612
- Malamud, U., & Perets, H. B. 2016, *ApJ*, 832, 160
- Malamud, U., & Perets, H. B. 2017a, *ApJ*, 842, 67
- Malamud, U., & Perets, H. B. 2017b, *ApJ*, 849, 8
- Manser, C. J., Gänsicke, B. T., Eggl, S., et al. 2019, *Science*, 364, 66
- Marois, C., Macintosh, B., Barman, T., et al. 2008, *Science*, 322, 1348
- Matsunaga, T., Heida, K., & Nikaido, O. 1991, *Photochem. Photobiol.*, 54, 403

REFERENCES

- Mayor, M., & Queloz, D. 1995, *Nature*, 378, 355
- McCree, K. J. 1971, *Agricultural Meteorology*, 9, 191
- McKay, C. P., & Stoker, C. R. 1989, *Reviews of Geophysics*, 27, 189
- Meadows, V. S. 2006, in *IAU Colloq. 200: Direct Imaging of Exoplanets: Science & Techniques*, ed. C. Aime & F. Vakili, 25–34
- Meadows, V. S. 2008, *Planetary Environmental Signatures for Habitability and Life*, ed. J. W. Mason, 259
- Meadows, V. S., Reinhard, C. T., Arney, G. N., et al. 2018, *Astrobiology*, 18, 630
- Mennesson, B., Gaudi, S., Seager, S., et al. 2016, *Society of Photo-Optical Instrumentation Engineers (SPIE) Conference Series*, Vol. 9904, *The Habitable Exoplanet (HabEx) Imaging Mission: preliminary science drivers and technical requirements*, 99040L
- Morbidelli, A., Chambers, J., Lunine, J. I., et al. 2000, *Meteoritics and Planetary Science*, 35, 1309
- Mustill, A. J., & Villaver, E. 2012, *ApJ*, 761, 121
- Nisbet, E. G., & Sleep, N. H. 2001, *Nature*, 409, 1083
- O'Malley-James, J. T., & Kaltenegger, L. 2017, *MNRAS*, 469, L26
- O'Malley-James, J. T., & Kaltenegger, L. 2018a, *MNRAS*, 481, 2487
- O'Malley-James, J. T., & Kaltenegger, L. 2018b, *Astrobiology*, 18, 1123
- O'Malley-James, J. T., & Kaltenegger, L. 2019, *MNRAS*, 485, 5598

REFERENCES

- Parsons, S. G., Gänsicke, B. T., Marsh, T. R., et al. 2017, *MNRAS*, 470, 4473
- Pavlov, A. A., & Kasting, J. F. 2002, *Astrobiology*, 2, 27
- Pavlov, A. A., Kasting, J. F., Brown, L. L., Rages, K. A., & Freedman, R. 2000, *J. Geophys. Res.*, 105, 11981
- Petigura, E. A., Howard, A. W., & Marcy, G. W. 2013, *Proceedings of the National Academy of Science*, 110, 19273
- Pickles, A. J. 1998, *PASP*, 110, 863
- Pierrehumbert, R., & Gaidos, E. 2011, *ApJ*, 734, L13
- Pollacco, D. L., Skillen, I., Collier Cameron, A., et al. 2006, *PASP*, 118, 1407
- Prins, S., Telting, J., & Østensen, R. 2019, *Open Astronomy*, 28, 61
- Quanz, S. P., Crossfield, I., Meyer, M. R., Schmalzl, E., & Held, J. 2015, *International Journal of Astrobiology*, 14, 279
- Quintana, E. V., Barclay, T., Raymond, S. N., et al. 2014, *Science*, 344, 277
- Ramirez, R. M. 2018, *Geosciences*, 8, 280
- Ramirez, R. M., & Kaltenegger, L. 2014, *ApJ*, 797, L25
- Ramirez, R. M., & Kaltenegger, L. 2016, *ApJ*, 823, 6
- Ramirez, R. M., & Kaltenegger, L. 2017, *ApJ*, 837, L4
- Ramirez, R. M., & Kaltenegger, L. 2018, *ApJ*, 858, 72
- Rasool, S. I., & de Bergh, C. 1970, *Nature*, 226, 1037

REFERENCES

- Rauer, H., Gebauer, S., Paris, P. V., et al. 2011, *A&A*, 529, A8
- Reimers, D. 1975, *Circumstellar envelopes and mass loss of red giant stars.*, 229–256
- Reinhard, C. T., Olson, S. L., Schwieterman, E. W., & Lyons, T. W. 2017, *Astrobiology*, 17, 287
- Rhew, R., & Mazéas, O. 2010, *Geophys. Res. Lett.*, 37, L18813
- Ricker, G. R., Winn, J. N., Vanderspek, R., et al. 2014, *Society of Photo-Optical Instrumentation Engineers (SPIE) Conference Series*, Vol. 9143, *Transiting Exoplanet Survey Satellite (TESS)*, 914320
- Ridden-Harper, A. R., Snellen, I. A. G., Keller, C. U., et al. 2016, *A&A*, 593, A129
- Robinson, T. D., Meadows, V. S., & Crisp, D. 2010, *ApJ*, 721, L67
- Robinson, T. D., Stapelfeldt, K. R., & Marley, M. S. 2016, *PASP*, 128, 025003
- Robinson, T. D., Meadows, V. S., Crisp, D., et al. 2011, *Astrobiology*, 11, 393
- Rowe, J. F., Bryson, S. T., Marcy, G. W., et al. 2014, *ApJ*, 784, 45
- Rugheimer, S., & Kaltenegger, L. 2018, *ApJ*, 854, 19
- Rugheimer, S., Kaltenegger, L., Segura, A., Linsky, J., & Mohanty, S. 2015a, *ApJ*, 809, 57
- Rugheimer, S., Kaltenegger, L., Zsom, A., Segura, A., & Sasselov, D. 2013, *Astrobiology*, 13, 251
- Rugheimer, S., Segura, A., Kaltenegger, L., & Sasselov, D. 2015b, *ApJ*, 806, 137

REFERENCES

- Sagan, C., & Newman, W. I. 1983, QJRAS, 24, 113
- Sagan, C., Thompson, W. R., Carlson, R., Gurnett, D., & Hord, C. 1993, Nature, 365, 715
- Saumon, D., Holberg, J. B., & Kowalski, P. M. 2014, ApJ, 790, 50
- Schreiber, M. R., Gänsicke, B. T., Toloza, O., Hernandez, M.-S., & Lagos, F. 2019, ApJ, 887, L4
- Schwieterman, E. W., Robinson, T. D., Meadows, V. S., Misra, A., & Domagal-Goldman, S. 2015, ApJ, 810, 57
- Schwieterman, E. W., Meadows, V. S., Domagal-Goldman, S. D., et al. 2016, ApJ, 819, L13
- Schwieterman, E. W., Kiang, N. Y., Parenteau, M. N., et al. 2018, Astrobiology, 18, 663
- Seager, S., Bains, W., & Petkowski, J. J. 2016, Astrobiology, 16, 465
- Seager, S., Whitney, B. A., & Sasselov, D. D. 2000, ApJ, 540, 504
- Segura, A., Kasting, J. F., Meadows, V., et al. 2005, Astrobiology, 5, 706
- Segura, A., Krelove, K., Kasting, J. F., et al. 2003, Astrobiology, 3, 689
- Segura, A., Meadows, V. S., Kasting, J. F., Crisp, D., & Cohen, M. 2007, A&A, 472, 665
- Shklovskii, I. S., & Sagan, C. 1966, Intelligent life in the universe
- Snellen, I., de Kok, R., Birkby, J. L., et al. 2015, A&A, 576, A59

REFERENCES

- Snellen, I. A. G., de Kok, R. J., le Poole, R., Brogi, M., & Birkby, J. 2013, *ApJ*, 764, 182
- Spergel, D., Gehrels, N., Baltay, C., et al. 2015, arXiv e-prints, arXiv:1503.03757
- Stern, A., & Spencer, J. 2003, *Earth Moon and Planets*, 92, 477
- Stern, S. A. 2003, *Astrobiology*, 3, 317
- Stock, S., Reffert, S., & Quirrenbach, A. 2018, *A&A*, 616, A33
- Swan, A., Farihi, J., Koester, D., et al. 2019, *MNRAS*, 490, 202
- Tamura, M. 2009, in *American Institute of Physics Conference Series*, Vol. 1158, *American Institute of Physics Conference Series*, ed. T. Usuda, M. Tamura, & M. Ishii, 11–16
- Tevini, M. 1993, *Lewis*, Boca Raton, 125
- Tian, F., France, K., Linsky, J. L., Mauas, P. J. D., & Vieytes, M. C. 2014, *Earth and Planetary Science Letters*, 385, 22
- Tinetti, G., Drossart, P., Eccleston, P., et al. 2016, *Society of Photo-Optical Instrumentation Engineers (SPIE) Conference Series*, Vol. 9904, *The science of ARIEL (Atmospheric Remote-sensing Infrared Exoplanet Large-survey)*, 99041X
- Tipler, F. J. 1980, *QJRAS*, 21, 267
- Tipler, F. J. 1993, *Society of Photo-Optical Instrumentation Engineers (SPIE) Conference Series*, Vol. 1867, *SETI—a waste of time!*, ed. S. A. Kingsley, 28–35

REFERENCES

- Toon, O. B., McKay, C. P., Ackerman, T. P., & Santhanam, K. 1989, *J. Geophys. Res.*, 94, 16287
- Traub, W. A., & Stier, M. T. 1976, *Appl. Opt.*, 15, 364
- Tremblay, L., Line, M. R., Stevenson, K., et al. 2020, *AJ*, 159, 117
- Tsiaras, A., Waldmann, I. P., Tinetti, G., Tennyson, J., & Yurchenko, S. N. 2019, *Nature Astronomy*, 3, 1086
- Tsiaras, A., Rocchetto, M., Waldmann, I. P., et al. 2016, *ApJ*, 820, 99
- Turbet, M., Forget, F., Head, J. W., & Wordsworth, R. 2017, *Icarus*, 288, 10
- Van Eylen, V., Agentoft, C., Lundkvist, M. S., et al. 2018, *MNRAS*, 479, 4786
- van Sluijs, L., & Van Eylen, V. 2018a, *MNRAS*, 474, 4603
- van Sluijs, L., & Van Eylen, V. 2018b, *MNRAS*, 474, 4603
- Vanderburg, A., Johnson, J. A., Rappaport, S., et al. 2015, *Nature*, 526, 546
- Vassiliadis, E. 1993, *Acta Astronomica*, 43, 315
- Veras, D. 2016, *Royal Society Open Science*, 3, 150571
- Veras, D., & Fuller, J. 2019, *MNRAS*, 489, 2941
- Veras, D., & Gänsicke, B. T. 2015, *MNRAS*, 447, 1049
- Veras, D., Efroimsky, M., Makarov, V. V., et al. 2019, *MNRAS*, 486, 3831
- Vidal-Madjar, A., Lecavelier des Etangs, A., Désert, J. M., et al. 2003, *Nature*, 422, 143

REFERENCES

- Vidal-Madjar, A., Désert, J. M., Lecavelier des Etangs, A., et al. 2004, *ApJ*, 604, L69
- Villaver, E. 2011, in *American Institute of Physics Conference Series*, Vol. 1331, American Institute of Physics Conference Series, ed. S. Schuh, H. Drechsel, & U. Heber, 21–32
- Villaver, E. 2012, in *IAU Symposium*, Vol. 283, *IAU Symposium*, 219–226
- Villaver, E. 2014, in *Habitable Worlds Across Time and Space*, P35
- Voet, D., Gratzer, W. B., Cox, R. A., & P., D. 1963, *Biopolymers*, 1, 193
- Walker, S. I., Bains, W., Cronin, L., et al. 2018, *Astrobiology*, 18, 779
- Wallach, A., Morris, B. M., Branton, D., et al. 2018, *Research Notes of the American Astronomical Society*, 2, 41
- Williams, D. M., & Gaidos, E. 2008, *Icarus*, 195, 927
- Wolf, W. M., Townsend, R. H. D., & Bildsten, L. 2018, *ApJ*, 855, 127
- Wolszczan, A., & Frail, D. A. 1992, *Nature*, 355, 145
- Wordsworth, R., & Pierrehumbert, R. 2014, *ApJ*, 785, L20
- Xu, S., Ertel, S., Wahhaj, Z., et al. 2015, *A&A*, 579, L8
- Yang, J., Boué, G., Fabrycky, D. C., & Abbot, D. S. 2014, *ApJ*, 787, L2
- Yang, J., Ding, F., Ramirez, R. M., et al. 2017, *Nature Geoscience*, 10, 556
- Zhang, M. 2019, in *AAS/Division for Extreme Solar Systems Abstracts*, Vol. 51, *AAS/Division for Extreme Solar Systems Abstracts*, 327.08

REFERENCES

Zsom, A., Kaltenegger, L., & Goldblatt, C. 2012, *Icarus*, 221, 603

Zugger, M. E., Kasting, J. F., Williams, D. M., Kane, T. J., & Philbrick, C. R. 2010, *ApJ*, 723, 1168